UCLouvain

École polytechnique de Louvain

Numerical study of the cooling stability of spent nuclear fuels in storage and deactivation pools

Analysis of the natural convection in the pool

Author: **Gauthier RUBBERS**
Supervisor: **Miltiadis PAPALEXANDRIS**
Readers: **Vincent LEGAT, Vincent DELEDICQUE**
Academic year 2022–2023
Master [120] in Mechanical Engineering

Acknowledgments

At first, I would like to thank Pr Miltiadis Papalexandris, the professor who initiated this master thesis. I have learned a lot about numerical fluid dynamic and buoyancy driven flows in general since the beginning of this master thesis, and the feedback he provided throughout the year clearly helped me a lot in the accomplishment of this work. I would also like to thank Mr Deledicque, the responsible for my master's thesis at Bel V, for his help and for the informations he gave me on the geometry of a nuclear assembly.

I would also like to thank Mr Thomas Keutgen and David Colignon, who are in charge of the CECI Clusters. They were present to answer the many technical question that I had this year on the installation of Code Saturne on Lemaitre3

Similarly, I am also very grateful towards my friend, Amaury Fierens, who helped me with the understanding of the software necessary to connect to the Clusters via SSH. He also answered my questions about the redaction of this manuscript.

Finally, I would like to thank my parents and my sisters for their support during this semester. I would also like to thank my roommates for their support during these last months.

Abstract

Since the Fukushima disaster in 2011, which caused the partial evaporation of the water contained in the spent fuel pools due to pump failure, the scientific community has set itself the goal of developing new safety systems to increase the safety of these pools. To this end, it is very important to develop numerical models in order to accurately model all the phenomena of convection, boiling and all the chemical reactions that can take place near the immersed assemblies. In this master thesis, we established a simplified model of such a pool in order to quantitatively and qualitatively analyze the water flow in the assemblies. The goal is to analyze the flow when the cooling system pumps are deactivated in order to simulate the worst case scenario. Several assembly arrangements were implemented and analyzed in order to know which one allows to limit the local temperature increase. It regularly happens that a local backflow of water in the channels causes a heating which could induce a local boiling of the water and the premature degradation of the assembly sheaths. In this study, a two-dimensional numerical model was developed using Code Saturne, a French software developed by EDF. As the assemblies can't be resolved in detail, a porous medium approximation was used. We found that in order to minimize the local temperature rise during the first 4 minutes of the outage, the most powerful nuclear waste should be placed in the middle of the rack. Furthermore, in extreme cases, hot spots are sometimes 25 degrees hotter than the surrounding water, which can cause local boiling to occur faster than expected.

Contents

Introduction

Nuclear fission has been used for decades in Belgium for the production of electricity. There are currently five nuclear reactors in service, producing thirty percent of the electricity used in the country (1). These powerplants are based on physical principles discovered in the thirties and the forties by several famous scientist such as Niels Bohr, Enrico Fermi and James Chadwick (2). The latter discovered the neutron in a famous experience realised in 1932, which would pave the way to nuclear fission and nuclear energy. The first application of nuclear fission came during the second world war with the bombing of Hiroshima and Nagasaki in 1945, and the first program promoting the peaceful use of the technology came in 1953 with the "atom for peace" program launched by the Eisenhower administration.

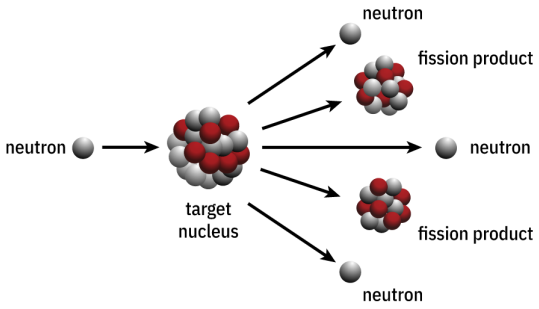

Figure 1: Nuclear fission reaction

The basic principle behind nuclear fission is the fact that some atoms such as plutonium or uranium tends to break into smaller atoms when they collide with a neutron, with the emission of two or more fast neutrons (3). This means that a chain reaction is possible and that it can be controlled via the absorption of some neutrons by various mechanisms such as control rods (these are rods generally made of graphite, which tends to absorb neutron) or boron water. These neutrons are extremely fast (a few percentage of the speed of life), which means that the time to double the power output would theoretically be below one millisecond if we only tried to control the reactor by acting on these "instantaneous" neutrons. This would be way too dangerous, so the power output is instead controlled by playing on the population size of the "delayed neutrons". These are not directly emitted during a fission event, but by the disintegration of the fission product which can happens much later on.

It is still important to note that the neutron population can grow very quickly out of control if one doesn't correctly follow all the safety procedures during an emergency situation. In the past, such catastrophic events have lead to the evacuation of wide swat of land like in the Chernobyl and the Fukushima meltdowns (4). the pressure inside the primary circuit is extremely high (150 bar) (5) to allow water to exist at a liquid state at high temperature (it increases the efficiency of the thermodynamic cycle used to produce electricity). The temperature of the water flowing in and out is around 290 C° and 330 C° respectively. The fuel is not pure U-235 as it would be way too reactive. Instead, it is slightly enriched from 0.72% to 3% approximately. Other types of reactor such as the smaller reactors used in SNLEs (sous-marin nucléaire lanceur d'engins) can use uranium with level of enrichment up to 20%, which is needed for achieving a high power density.

The fission reactions release a lot of heat that is generally evacuated by the water flowing through the core (some exotic reactors use other fluids such as lead-bismuth or sodium). The neutrons and the fission products contain most of the energy, and will dissipate it through the surrounding environment via multiple elastic collisions, the rest of the energy being released under the form of gamma photons. In the case of the Belgian reactor model, the water also slows the neutrons down as it increases the likelihood for a neutron to cause a fission in the surrounding material. The hot water is evacuated out of the core by pumps and is brought in several massive heat exchangers so that the heat is transferred to non radioactive water. The vapor is then sent to the turbines to produce electricity using the Rankine cycle. The thermodynamic efficiency of this cycle is around thirty percent, which means that there is a huge difference between the thermal and the electrical power of a nuclear reactor (a modern 1500 MW EPR [1] reactor has a thermal output of more than 4500 MW). The steam that comes out of the turbine is then condensed via the tertiary water circuit before being sent back to the heat exchanger. The water of this tertiary circuit is then sent to the huge cooling towers to be condensed with water coming from a nearby river (the Meuse or the Scheldt in our case).

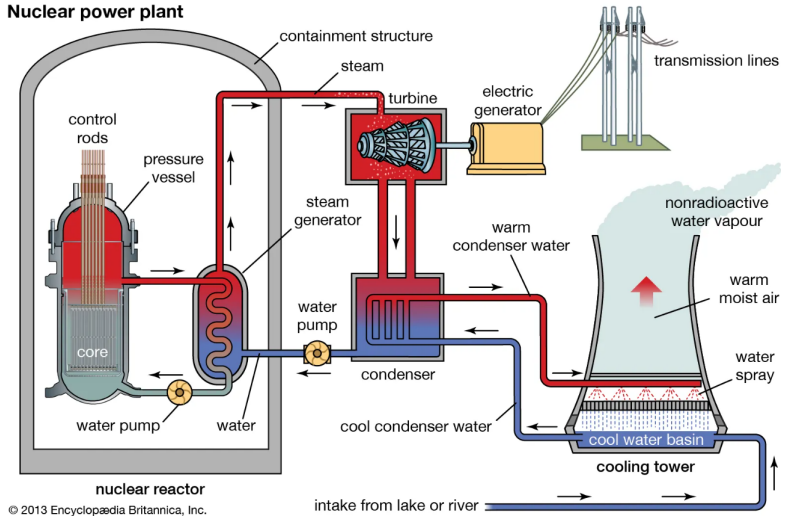

Figure 2: PWR schematic

The five reactors are located in two nuclear power plants, three in Doel on the banks of the Scheldt and two in Tihange near the city of Liege. Two other reactors are currently being dismantled by Engie Electrabel (1). They are PWR [2], which means that the water flowing inside the vessel is maintained in a liquid phase at high pressure.

One major criticism made by opponents to nuclear energy is that nuclear reactors produce very dangerous nuclear wastes that need to be stored safely for thousands of years. After many years of research, scientists came to the conclusion that the best way this nuclear waste could be managed on the long term was to bury it in very stable geological layers, even if it is not a popular solution for the local public opinion (6). However, one can't simply extract the spent uranium and the minor actinides from the core to put them directly in a cave far below our feet, for the simple reason that these wastes are extremely hot due to radioactive decay. It is thus necessary to store them temporarily in spent fuel pools in order to cool them down before the final burial phase.

The activity of a radioactive material follows an exponential law, with a half-life depending on the element. The combination of several radionuclides with many different half-lives means that the power output of the spent fuel will decrease following a rather complex pattern. As the spent fuel is extremely radioactive and dangerous, it has not undergone any industrial transformation since it was extracted from the core, which means that it is still in its original fuel assembly. These assemblies have a square section of 20 cm long and are gathered together in "racks" that are put in a deep water pool,

[1] Evolutionary Power Reactor
[2] Pressurized Water Reactor

with a typical water depth of 8 to 10 meters.

Such a depth is required to shield the workers from the deathly radiation emanating from the assemblies. The cooling of the fuel is assured by the natural convection happening in the pool. The water in contact with the fuel will heat up, which will decrease its density compared to the cold water above it, which in turn will drive the formation of convection cells through the pool. The hot water is then collected near the surface and is brought to a cooling system before being re-injected on the bottom of the pool. It is important to note that the flow in the pool can be very complicated depending on the position of the spent fuel cells and the power density distribution among them. In some case, a reflux can appear, which means that the flow can be directed toward the ground in some of the assemblies.

In every rack, the assemblies are separated by thin walls a few millimeters thick. An assembly consists of approximately 264 fuel rods assembled in parallel and is 4 meters long. Each rod is made of small fuel pellets stacked on top of each other. The sheath of a fuel rod is made out of pure zirconium, as it has a very low neutron absorption cross-section and it is corrosion resistant at high temperature. The water can flow between the rods, which will induce a pressure loss.

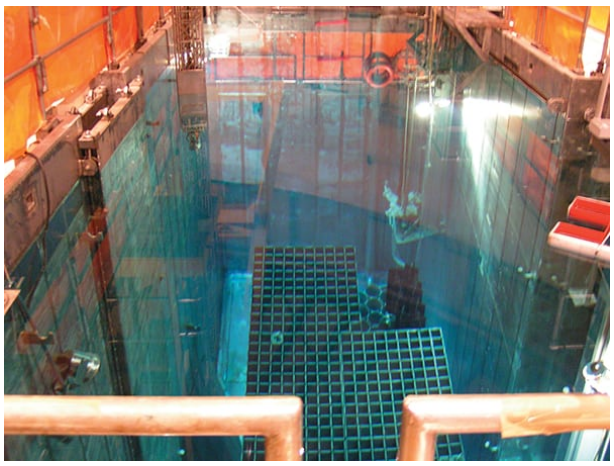

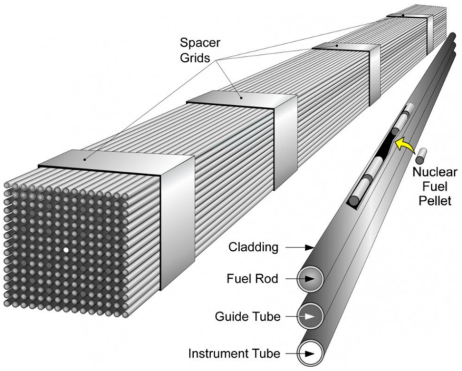

Figure 3: rack assembly in the pool (left), and spent fuel assembly (right)

These pools must be cooled continually to avoid the complete evaporation of the water over time. if it happened, the fuel would be primarily cooled down by natural air convection, but air is way less dense than water and the spent fuel would thus melt, causing a very serious nuclear accident. Depending on the case, the spent fuel must be stored between 3 to 6 years in a pool right next to the reactor, and 10 to 20 years under water after that.

The spent fuel assemblies are so radioactive that the operators need to use a dedicated robot to move them underwater during a refill operation. In general, a reactor is opened every year or every year and a half to replace one third of its fuel loading so in general the job of the operators is mainly to check that the cooling process takes place without any problem. The main reason why only a third of the fuel is replaced at a given time is to avoid reactivity variation before and after the break. Indeed, if all the fuel is changed in one go, the reactor will go from a state where nearly all its fuel is spent to a state where all the fuel is fresh and very reactive. This would mean that it would be harder to maintain a constant power output and so the fuel is replaced progressively.

Chapter 1

State of the art and software used

As explained in the introduction, a total loss of power in a nuclear powerplant can lead to a catastrophic evaporation of the water contained in the spent fuel pools. It effectively happened during the Fukushima-Daishi accident in 2011 where the water started to boil, which caused the diminution of the level of water. However, scientist didn't wait for this accident to happen to start building predictive models on the water evaporation in such pools. A review of the phenomena appearing before the total evaporation of the water was conducted in 2010 by Aliatka and Al (7), where they showed that the water would start to boil after 80 to 110h. However, they used data sets from a RBMK 1500 [1], which used fuel uranium with a relatively low enrichment level (only 2,6%, compared to 4% in a PWR (8)), so the time before the start of the boiling process will not be exactly the same with a pool full of assemblies coming from a Belgian reactor.

After the disaster, researchers in Shanghai started to look at different ways to improve the cooling system by using a passive installation. A proposition was made for a passive system in Ye and all (9), and a 3D CFD simulation was realized in order to check if the water would start to boil. As their computations where made in 3D, it allowed them to capture a lot of the phenomena happening in the pool, but it also implied a very high computational cost. They proved that with their proposed modifications to the spent fuel pool, the water would never boil, even in a situation where all power is lost.

Closer to us, in France, the DENOPI project was launched in order to do experiments and to validate existing models (10). The approach used is decomposed in three scales: the spent fuel scale, the assembly scale and the clad scale. In addition to the study of the natural convection happening in the pool, this project also looked at the oxydation of zirconium and the effect of hot steam on the reaction, which are expected phenomena when a hot assembly is no longer cooled by water. The heat exchange with the environment when the assemblies are exposed to air has also been investigated by Oertel and al (11), where their simulations considered both a part with a liquid at the bottom of the assembly, and a gas at the top. They treated the inside of the assemblies as a porous medium with a pressure loss term due to the viscous friction of the fluid against the rods. This porous medium approach is very commonly used when the resolution of the mesh is larger than the size of the physical element in the domain (here, the rods have roughly the same size as the smaller elements). The different properties such as the head loss coefficients and the heat flux intensity can be modelled using an RVE [2] approach, were we consider a fictitious homogeneous medium whose thermal and mechanical properties represent the "average" properties of the real porous medium.

The idea of treating a porous medium as it was a simpler uniform material is not new. An estimation of the volumetric flow of a fluid going through a porous material was first introduced

[1] RBMK: high-power pressure tube reactor
[2] RVE : Representative Volume Element

by Henry Darcy during the nineteenth century with his famous Darcy's Law, that links the volumetric flux q through a medium to the pressure drop, the length L of the considered region, the permeability k and the dynamic viscosity μ of the fluid :

$$q = -\frac{k\Delta p}{\mu L} \tag{1.1}$$

This Law gives a handy approximation of the flux q, and it was derived theoretically by many authors, like Neuman (12). This RVE methodology is very common in materials science, especially when trying to compute the mechanical properties of a composite. Serge Bories applied it to a porous medium filled with a fluid undergoing natural convection (13). In a similar manner, Bejan and Khair used it to develop an analytical solution to the flow induced by the natural convection along a vertical plate embedded in a porous medium (14).

In yet another study, a team of Taiwanese scientist developed a 3D model taking into account the evaporation rate at the surface of the pool; their results are presented in Hung and al (15). They used the porous medium approximation and an empirical approximation was used to compute the evaporation rate at the free surface from the Nusselt number. As their purpose was to simulate a worst case scenario, they set the height of water above the assemblies to 3 meters, which is the minimum value allowed by the legislation. Their results show that after a long enough time, the temperature is higher near the surface of the pool than in the assemblies if the cooling system is broken. This is explained by the fact that the heat transfer from the water to the atmosphere is less efficient than the heat transfer occurring in the pool (because air is far less dense than water).

The main goal of this master thesis is to make a qualitative and quantitative analysis of the convection and the heat accumulation happening inside a spent fuel pool when the pumps of the cooling system are broken by using a 2D computational fluid dynamic simulation (also called CFD). We will be using Code Saturne, a french open-source software developed by EDF for internal use. It was proved that this software was able to give correct results for turbulent flows (16). This master thesis is conducted under the supervision of Bel V, a subsidiary of the Federal Agency for Nuclear Control in Belgium. More precisely, this thesis will contain a study of the impact of some selected parameters on the convection pattern. These parameters include :

- the distribution of the fuel cells in the pool
- the residual thermal power distribution
- the distance between the side walls and the nearest rack

In an early phase, it was planned to look at the evaporation rate over a long period of time (a few hours), but the very large size of the domain combined with the very small size of the individual mesh cells means that we won't be able to conduct simulation longer than a few minutes, while the evaporation only starts to become significant after a few hours in the worst case (Wang et al showed that the fuel assemblies are uncovered after 2,7 days (17)). For the same reason of limited computational resources, the computations will be conducted in two dimensions as even the clusters of the CECI don't allow computation time longer than two days. Also due to that limitation, the porous medium approximation and a pressure loss source term will be used in order to emulate the presence of the rods inside the assemblies.

In the first part of this report, we will briefly describe the software and the discretized equations used by code Saturn to simulate the flow. We will then explain the physical hypotheses, the approximation implemented in Code Saturne and their numerical validations. In a second part, we will show the results of several simulations with different values for the studied parameters. We will then give a physical explanation on the impact of the parameters on the observed flows.

It is worth noting that the results won't exactly match a real situation and must thus be taken with some caution as the simulated flow is two dimensional. For instance, we would need to simulate a third spatial dimension and a finer mesh to accurately represent turbulence. Instead, we use a RANS approach with the $k - \epsilon$ model to capture the turbulent effects. The size of the mesh will be limited to 4 millimeters due to the time limitation. It is also assumed that the water temperature will always remains below 100 degree Celsius as Code Saturne is not equipped with a module able to simulate two-phase flows in its basic version.

Figure 1.1: Code Saturne logo

As said before, Code Saturne is a free software in open access that has been developed by the R&D department of Electricité de France since 1997. It is on GNU [3] since 2007. It is based on a finite volume approach and it can be used with a wide range of mesh format, from Gmesh to MED. Here we are mostly interested in the incompressible module of the software as we are obviously working with liquid water. We will be using the SHAPE and MESH modules of the SALOME software to generate the different meshes used in our simulations. All the parameters of a simulation can be set either manually in a setup.xml file, or via a GUI [4] present by default with the software. We couldn't generate the mesh on the CECI [5] clusters as it is not possible to use a GUI on them.
Code Saturne also allows its users to write the specifications of the simulations in small C scripts compiled when the code is run. It is especially useful when complex pressure loss needs to be implemented or when some specific post-treatment operations are needed to visualize more specific sets of Data.

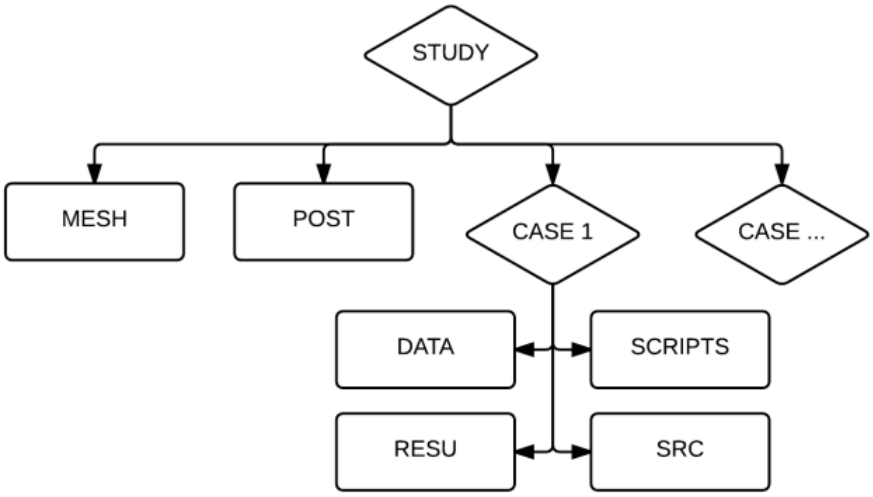

Figure 1.2: code saturne

[3]"GNU" stands for GNU's Not Unix. GNU is a complete free software system that is backwards compatible with Unix.
[4]GUI : Graphical User Interface
[5]CECI : Consortium des Équipements de Calcul Intensif

a Code Saturne simulation folder is structured in different studies which can each contains multiple cases. The only thing that the cases of a same study will share is the mesh file and the post processing data folder.

A new study can be created via the terminal using the following bash command :

```
code_saturne create -s STUDY -c CASE_NAME1 CASE_NAME2
```

A typical study contains :

1. a MESH directory, which contains a mesh file (.MED, .msh or CGNS for instance).
2. a POST directory, which contains an eventual script used for the post processing.
3. one or more CASE directory.

The DATA directory contains the setup.xml file, the run.cfg file, which is used to specify the number of thread used for the simulation, and the executable of the simulation.

All the user subroutines are put in the SRC folder, and the results are stored in the RESU file using the format: year-Month-Day-Hour-Minute .

Chapter 2

The mathematical background

2.1 Naviez-Stokes equations

In this section, we will introduce the equations used by Code Saturne to simulate the flow inside the spent fuel pool. We will derive them from the elementary laws of physics such as mass, momentum and energy conservation.

2.1.1 Mass conservation

In any finite material volume Ω inside the pool, the mass is constant as the boundary of the volume follows the trajectory of the particles. One can thus write

$$\frac{d}{dt}(\int_{\Omega} \rho \, d\Omega) = 0 \tag{2.1}$$

However, as stated before, this is only true for a material volume , a.k.a a finite volume that moves with the flow. But in our case, we will be using a fixed mesh so we need to go from a Lagrangian to a Eulerian formulation of the conservation of mass. To do that, it is important to introduce the Reynold Transport theorem (18):

$$\frac{d}{dt}(\int_{\Omega(t)} F \, d\Omega) = \int_{\Omega(t)} \frac{\partial F}{\partial t} \, d\Omega + \int_{\partial\Omega(t)} (v_b \cdot n) F \, d(\partial\Omega) \tag{2.2}$$

In this way, it is possible to get rid of the temporal derivative outside of the integral. We can now apply the theorem to conservation of mass :

$$\frac{d}{dt}(\int_{\Omega(t)} \rho \, d\Omega) = \int_{\Omega(t)} \frac{\partial \rho}{\partial t} \, d\Omega + \int_{\partial\Omega(t)} (v_b \cdot n) \rho \, d(\partial\Omega) = 0 \tag{2.3}$$

it is possible to use the Green theorem for the second integral in order to transform the integral of surface into an integral of volume.

$$\int_{\Omega(t)} \frac{d\rho}{dt} \, d\Omega + \int_{\partial\Omega(t)} (v_b \cdot n) \rho \, d(\partial\Omega) = \int_{\Omega(t)} \frac{\partial \rho}{\partial t} + \nabla \cdot (\rho u) \, d\Omega = 0 \tag{2.4}$$

The last integral must be true for any volume, so it can be written in differential form :

$$\frac{\partial \rho}{\partial t} + \nabla \cdot (\rho u) = 0 \tag{2.5}$$

2.1.2 Momentum conservation

Similarly to mass conservation, it is possible to use the Reynold transport theorem and the green theorem to find a differential expression for momentum conservation:

$$\frac{d}{dt}(\int_{\Omega(t)} \rho u \, d\Omega) = \int_{\Omega(t)} \frac{\partial \rho u}{\partial t} \, d\Omega + \int_{\partial\Omega(t)} u \otimes (\rho u) \, d(\partial\Omega) \tag{2.6}$$

by the Green theorem :

$$\frac{d}{dt}(\int_{\Omega(t)} \rho u \, d\Omega) = \int_{\Omega(t)} \frac{\partial \rho u}{\partial t} + \nabla \cdot (\rho u u) \, d\Omega \tag{2.7}$$

Newton's second law can be used to equal this relation to the sum of the forces applied on the finite volume. Here, we consider three forces :

1. the gravitational force (with a constant acceleration g that can be set to $9,81[\frac{m}{s^2}]$ for instance)
2. a source of momentum (head losses)
3. the internal constraints modelized by the stress tensor σ

The equation 2.7 is then combined with the three forces to give the following partial differential equation:

$$\frac{\partial \rho u}{\partial t} + \nabla \cdot (\rho u u) = \rho g + \nabla \cdot \sigma - \rho K u \tag{2.8}$$

Here, $\rho K u$ is the term that models the head losses, and K is a 3×3 tensor whose coefficients must be chosen by the user.

This equation still depends on σ, so we still must find a relation between the stress tensors and the fluid properties to close the model. To to that, the stress tensor is decomposed in two parts: its trace and its deviatoric part.

$$\tau = \sigma - \frac{1}{3} trace(\sigma) I \tag{2.9}$$

In the case of a Newtonian fluid, one can make the approximation that the local viscous stress rate is linearly proportional to the strain rate. In tensor term, it means that the deviatoric part of the stress tensor is linearly proportional to the deviatoric part of the strain tensor S (its definition is $2S = \nabla u + \nabla u^T$).

$$\tau = 2\mu S - \frac{2}{3}\mu \times trace(S) I \tag{2.10}$$

The trace of the stress tensor is then linked to a thermodynamic variable called pressure via the following relation:

$$p = -\frac{1}{3} trace(\sigma) \tag{2.11}$$

The equation 2.8 can be expressed with these new relations, which give the following expression for the momentum:

$$\frac{\partial \rho u}{\partial t} + \nabla \cdot (\rho u u) = \rho g - \nabla p + \nabla \cdot (\mu(\nabla u + \nabla u^T - \frac{2}{3} trace(\nabla u) I)) - \rho K u \tag{2.12}$$

The left term of this equation can be expressed differently using the mass conservation relation:

$$\frac{\partial \rho u}{\partial t} + \nabla \cdot (\rho u u) = \rho \frac{\partial u}{\partial t} + u \frac{\partial \rho}{\partial t} + u \nabla \cdot (\rho u) + \rho u \cdot \nabla u = \rho \frac{\partial u}{\partial t} + (\rho u) \cdot \nabla u \tag{2.13}$$

Finally, the following expression for the momentum is obtained :

$$\rho \frac{\partial u}{\partial t} + (\rho u) \cdot \nabla u = \rho g - \nabla p + \nabla \cdot (\mu(\nabla u + \nabla u^T - \frac{2}{3} trace(\nabla u) I)) - \rho K u \tag{2.14}$$

However, it is still necessary to find a differential expression for temperature, as the density will depend upon it via the Boussinesq approximation (that will be developed further in this report). In order to do that, one must write the conservation of energy and enthalpy.

2.1.3 Energy and enthalpy conservation

Similarly to the momentum and mass equation, the Reynold transport theorem can be used again with the Green theorem on a control volume to get the following relation for the total energy:

$$\frac{d}{dt}(\int_{\Omega(t)} \rho e_t \, d\Omega) = \int_{\Omega(t)} \frac{\partial \rho e_t}{\partial t} + \nabla \cdot (\rho u e_t) \, d\Omega \tag{2.15}$$

The variation of the internal energy inside such a control volume is due to different phenomenons listed below :

1. The heat flux at the boundary of the control volume modelized by the Fourier Law : $q = -\lambda \nabla T$
2. An imposed heat source term Q, in our case it will be used to model the heat released by the spent fuel
3. The energy released by viscous dissipation : $2\mu S^D : S^D$ [1] with S^D the deviatoric par of the strain tensor. This term is usually negligible compared to the diffusion and the source terms
4. The work of the pressure : $-\nabla \cdot (pu)$
5. The work of gravity : $\rho g \cdot u$

After gathering all the terms, the following expression is obtained for the total energy :

$$\frac{\partial \rho e_t}{\partial t} + \nabla \cdot (\rho u e_t) = -\nabla \cdot (pu) + \rho g \cdot u + 2\mu S^D : S^D + Q - \nabla \cdot (-\lambda \nabla T) \tag{2.16}$$

The equation for the internal energy e can be derived from 2.16 by using the relation $e_t = e + \frac{1}{2} u \cdot u$ and the Lagragian notation $\frac{d(.)}{dt} = \frac{\partial(.)}{\partial t} + u \cdot \nabla(.)$:

$$\rho \frac{de}{dt} = -p \nabla \cdot u + 2\mu S^D : S^D + Q + \nabla \cdot (\lambda \nabla T) \tag{2.17}$$

The next step consists in finding the differential relation for the enthalpy h via the basic thermodynamic relation $h = e + \frac{p}{\rho}$:

$$\frac{dh}{dt} = \frac{de}{dt} + \frac{1}{\rho}\frac{dp}{dt} - \frac{p}{\rho^2}\frac{d\rho}{dt} \tag{2.18}$$

After combining it with equation 2.17, we get :

$$\rho \frac{dh}{dt} = \frac{dp}{dt} + 2\mu S^D : S^D + Q + \nabla \cdot (\lambda \nabla T) \tag{2.19}$$

For a pure substance, Maxwell's relations give the following equality :

$$dh = C_p dT + \frac{1}{\rho}(1 - \beta\rho) dp \tag{2.20}$$

Where β is defined as $\beta = -\frac{1}{\rho}\frac{\partial \rho}{\partial T}$ at constant pressure. It is called the thermal expansion coefficient and depends on the temperature and the material considered. Here it will be neglected, so that the enthalpy only depends on the temperature.
Finally, relation 2.20 with β set to zero can be used to replace the enthalpy h by the temperature :

$$\rho C_p \frac{dT}{dt} = \frac{dp}{dt} + 2\mu S^D : S^D + Q - \nabla \cdot (-\lambda \nabla T) \tag{2.21}$$

the three equations are gathered to get the following system:

$$\begin{cases} \dfrac{\partial \rho}{\partial t} + \nabla \cdot (\rho u) = 0 \\ \rho \dfrac{\partial u}{\partial t} + (\rho u) \cdot \nabla u = \rho g - \nabla p + \nabla \cdot (\mu V^d) - \rho K u \\ \rho C_p \dfrac{dT}{dt} = \dfrac{dp}{dt} + 2\mu S^D : S^D + Q + \nabla \cdot (\lambda \nabla T) \end{cases} \tag{2.22}$$

[1] here, ":" represents the double dot product, indeed S:S corresponds to $S_{ij}S_{ij}$ in Einstein's notation.

2.2 The numerical simulation

We will now explain how we are going to simulate the flow inside the pool using Code Saturne. Concretely, in this section we will describe the different hypothesis made on the nature of the flow and how they were implemented in the software.

First, the RANS model will be introduced, which is a well known numerical approximation used to simulate a turbulent flow inside a very wide range of applications. It has the big advantage of not requiring much computing power compared to other strategies (like the DNS method [2]), while being quite accurate if the underlying turbulence model is correctly selected.

Secondly, the selected turbulence model (here, the $k - \epsilon$ model) will be discussed, why it was chosen in the first place, and what are the equation being solved in parallel to the Navier-Stokes equations. Note that the numerical discretization of the equations is not explained in details as it is not the subject of this master thesis.

The model used must take into account in one way or another the fact that the density of the water depends on the temperature. This can't be neglected at all since it is the main driving force of the flow. To do that, a very classical approximation was used in the configuration of the solver : The Boussinesq approximation.
In this frame of work, the momentum equation doesn't depend on the temperature, except for the gravitational term. The constant density in the convection term will induce a small error, but it is acceptable if the density variation is small enough (which is the case here, where we work with water with flows far below Mach one).

Then, The SIMPLEC algorithm is introduced to give an idea to the reader on how the software effectively solves the equations. We start by explaining a slightly simpler algorithm (The SIMPLE one) before giving the differences between this version and the SIMPLEC one. We also talk very briefly about the linear system solver since many of them are available to the users.

After explaining the different approximations and algorithms, next section describes how the values of the different physical constants were estimated and implemented. Basically, the viscosity, the thermal capacity, the heat conduction coefficient and the thermal dilatation coefficient are all functions of temperature, so an interpolation had to be made for the solver. We described how it was done with a simple python module and a few experimental data points.
Similarly, an estimation of the porosity coefficient was computed, and a methodology to compute the head loss coefficient in a fuel assembly is conducted in section 4.5. They required a little simulation in a simple pipe to make sure that the code is working properly.

The last subsection of this chapter explains how the pool was discretized, using different submeshes in order to impose different boundary conditions on the walls and the surface. The number of submeshes used is quite large because the boundary conditions on each face of the external walls and on the walls between each assembly needed to be imposed separately in the software.

[2] DNS: Direct Naviez Stokes

2.2.1 The RANS model

The problem with numerical analysis of turbulent flow is that one would need to have a very refined mesh in order to capture all the details and all the complexity of such a flow. In practice, a mesh with individual cells smaller than the Kolmogorov scale would be necessary. This is not possible in practice in most of the cases due to evident computation power limitation. In order to tackle such a problem, an approximation called the Reynold Average Navier-Stokes was developed. It basically consist in dividing all the unknown variables into an average and a fluctuating component and then solve numerically the former.
Here is the so called Reynold decomposition of a generic variable ϕ:

$$\phi = \overline{\phi} + \phi' \tag{2.23}$$

Where $\overline{\phi(x)} = \frac{1}{t_2 - t_1} \int_{t_1}^{t_2} \phi(x,t)\, dt$
This operation is linear, but one must pay attention when trying to apply it to a product, indeed :

$$\overline{\phi_1 \phi_2} = \bar{\phi_1}\bar{\phi_2} + \overline{\phi_1' \phi_2'} \tag{2.24}$$

others relevant quantities in the study of turbulent flows include the root mean square of a fluctuating quantity, the turbulent kinetic energy k and the dissipation rate ϵ:

$$\phi_{rms} = \sqrt{\overline{\phi_1' \phi_2'}} \tag{2.25}$$

$$k = \frac{1}{2}(\overline{u_1^{2\prime}} + \overline{u_2^{2\prime}} + \overline{u_3^{2\prime}}) \tag{2.26}$$

$$\epsilon = \nu \sum \sum \overline{\frac{\partial u_i'}{\partial x_j}} \tag{2.27}$$

2.26 and 2.27 represent respectively the turbulent kinetic energy density and the turbulent dissipation rate.

If the averaging operator is applied to the system of equations obtained at the end of the previous section, it is possible to get the following by neglecting the viscous dissipation in the energy equation (see (18) section 2.1.4) :

$$\begin{cases} \dfrac{\partial \rho}{\partial t} + \nabla \cdot (\rho \overline{u}) = 0 \\ \rho \dfrac{\partial \overline{u}}{\partial t} + (\rho \overline{u}) \cdot \nabla \overline{u} = -\nabla \overline{p*} + \nabla \cdot (2(\mu + \mu_t)\overline{S}^D) - \rho K \overline{u} - \nabla \cdot (\rho R^D + 2\mu_t \overline{S}^D) + (\rho - \rho_0) g \\ \rho C_p \dfrac{d\overline{T}}{dt} = \dfrac{d\overline{p}}{dt} + Q + \nabla \cdot ((\lambda + \lambda_t) \nabla T) \end{cases} \tag{2.28}$$

With $p* = p - \rho_0 g \cdot x + \frac{2}{3}\rho k$.

There is a new term R called the Reynold stress tensor that appears due to the relation 2.24, $R = \overline{u' \otimes u'}$. It is still necessary to impose a relation between R and the speed. It is done by assuming that the Reynold stress tensor is aligned with the strain rate tensor of the mean flow $\overline{S}$:

$$\rho R = \frac{2}{3}\rho k I - 2\mu_t \overline{S^D} \tag{2.29}$$

Note that μ_t and λ_t are coefficients called respectively the eddy viscosity and the eddy conductivity, they are in general not constant and can be very hard to model.

2.2.2 The turbulence model

(In order to fully close the system of equation given by the RANS model, multiple sets of equations are available, they are called turbulence model and the main information to remember about them is that none of them suits perfectly every possible situation. For instance, the model that will be used throughout this study is called the $k-\epsilon$ linear production model, a slightly modified version of the classic $k-\epsilon$ model (19). It is known to be suitable for free-shear layer flows with relatively small pressure gradients. Similarly, for internal and wall-bounded flows, this model gives reasonable results in cases where the mean pressure gradients are small. We selected this model because the pressure gradients in the spent fuel pool are relatively small. On the contrary, it doesn't work well with unconfined flow, flow in non circular duct and rotating flow.

The main assumption of the model is that the turbulent viscosity μ_t is isotropic (ratio between Reynold stress and mean rate of deformation is the same in all directions). It consists of a set of two linear partial equations relating k, the turbulent kinetik energy, and ϵ, the dissipation rate in the flow. It is partially based on physic, but the model contains some constant that had to be determined using experimental measures.

Here, the classical $k-\epsilon$ model is described. The first equation for k is the following :

$$\rho\frac{\partial k}{\partial t}+\nabla k\cdot(\rho u)-\nabla\cdot(\mu+\frac{\mu_t}{\sigma_k}\nabla k)=P+G-\rho\epsilon \tag{2.30}$$

and the second equation for ϵ is :

$$\rho\frac{\partial \epsilon}{\partial t}+\nabla \epsilon\cdot(\rho u)-\nabla\cdot(\mu+\frac{\mu_t}{\sigma_\epsilon}\nabla \epsilon)=C_{\epsilon_1}\frac{\epsilon}{k}(P+(1-C_{\epsilon_3})G)-\rho C_{\epsilon_2}\frac{\epsilon^2}{k} \tag{2.31}$$

In the equations, the new term P is the production term of the means shear, it is computed as follow :

$$P=2\mu_t S^D:S^D-\frac{2}{3}\rho k\times trace(\nabla u) \tag{2.32}$$

The term G is the production term related to gravity :

$$G=\frac{1}{\rho}\frac{\mu_t}{\sigma_t}\nabla\rho\cdot g \tag{2.33}$$

It is also possible to link the dynamic turbulent viscosity to k and ϵ:

$$\mu_t=\frac{k^2}{\epsilon}\rho C_\mu \tag{2.34}$$

In addition to that, there are 6 unknown constant that must be determined. The values chosen in Code saturne are in the next table :

C_μ	C_{ϵ_1}	C_{ϵ_2}	σ_k	σ_ϵ
0.09	1.44	1.92	1.0	1.3

The last constant C_{ϵ_3} is either null if G >0, or equal to 1 if G <0. The model is based on physic because the two equations can be understood as follows : The rate of change of k (or ϵ) plus the transport of k (or ϵ) by advection is equal to the transport of k (or ϵ) by diffusion plus a rate of production, plus a rate of destruction. It is thus a conservation equation mixed with numerical coefficient coming from multiple data fitting (many different flows were computed to assign a value to each coefficient).

One of the issues with this model is that it overestimates the energy in the production term P (20). This is explained by the fact that P is a quadratic function of the strain S, so in order to reduce

the overestimation, C_μ is no longer held constant and is modified so that P depends linearly on S, hence the name of the modified model.

$$\bar{C_\mu} = [a_{12}]^2_{log} \frac{\epsilon}{P} \tag{2.35}$$

With $a = \frac{R}{k}$, and R the reynold stress tensor. There are many other models available, such as the k-$\epsilon - \frac{v^2}{k}$ or the $k - \omega$ model, but they are not used in this master thesis.

2.2.3 The Boussinesq approximation

As stated before, the fluid in the spent fuel pool is liquid water, which is basically incompressible under reasonable pressure. It would be tempting to consider ρ as a constant, but it is not as simple as that. Indeed, while the density doesn't vary much with the pressure, it can vary with temperature, and this effect is non negligible as the dependence of density on temperature is actually the phenomenon driving up natural convection.

The Boussinesq approximation consists in assuming that the effect of a variable density is negligible on the flow, except for the term with the gravitational constant g (21). The inertia term will thus not depends on temperature, and it allows the model to be quite accurate while limiting the number of coupled terms in the momentum equation. Note that this model can't be used to simulate the propagation of sound waves in a fluid as in this case, the effect of the variable density on the inertia term is very important. We are not interested in that kind of analysis so we will stick with this approximation. The Navier-Stokes equation can be partially modified as follow (here in order to not make the equations too complex, we decided not to work with the RANS equations, but the principle is very similar):
the mass conservation equation becomes :

$$\nabla \cdot u = 0 \tag{2.36}$$

The momentum equation can first be rewritten under the following form :

$$\frac{\partial u}{\partial t} + u \cdot \nabla u = -\frac{1}{\rho} \nabla p + \nu \nabla^2 u + g \tag{2.37}$$

The density depends on temperature via this equality :

$$\rho = \rho_0 - \beta \rho_0 (T - T_0) \tag{2.38}$$

the equation 2.37 is then slightly modified to take into account the impact of T on the gravitational term :

$$\frac{\partial u}{\partial t} + u \cdot \nabla u = -\frac{1}{\rho_0} (\nabla p - \rho_0 g \cdot z) + \nu \nabla^2 u - g\beta(T - T_0) \tag{2.39}$$

The density in the energy equation is also considered to be constant, so the equation doesn't change :

$$\rho C_p \frac{dT}{dt} = \frac{dp}{dt} + Q + \nabla \cdot (\lambda \nabla T) \tag{2.40}$$

The coefficient β depends itself on the temperature and an interpolation needs to be done in order to give a formula to the solver of Code Saturne. It will be done in another section.
Another drawback of this approximation is that the density variation $\frac{\Delta \rho}{\rho}$ must be way smaller than one. It is thus not a good idea to try to use it when dealing with gasses experiencing a dramatic variation in temperature, like in a fireplace.

The Boussinesq approximation can be used in Code Saturne by activating the option in the GUI and by providing an expression of the density that depends on temperature.

2.2.4 Introduction to SIMPLE and SIMPLE-C

In this chapter, we will introduce the algorithm used by Code Saturne to numerically solve the Navier-Stokes equations. The purpose of this master thesis is not to develop in details the inner working of such software, but it is still relevant to know what's happening under the hood.

The flow in the pool is basically incompressible, which means that there isn't any state equation one could use to find the relation between the pressure and the density like with perfect gases. This difficulty was circumvented by using what's called a pressure based solver, like the SIMPLE and SIMPLEC algorithms (22).
We will first explain the SIMPLE algorithm, and then we will describe the SIMPLEC algorithm that is actually used by Code Saturne. The SIMPLE algorithm tries to find the values of the pressure field and the velocity field at each time step by solving the mass and momentum conservation equations. The algorithm is iterative and an initial guess of the pressure field needs to be provided in order to start the computation. Before diving into the details, we will first display the simplified version of the Navier Stokes equations used in this explanation:

$$\begin{cases} \nabla \cdot u = 0 \\ \dfrac{\partial \rho u}{\partial t} + \nabla \cdot \rho u u = -\nabla p + \nabla(\mu \nabla u) + S \end{cases} \tag{2.41}$$

The first difficulty arises from the fact that there is no explicit equation for the pressure field. This issue is solved by computing the velocity field from a guess of the pressure field via the momentum equation, followed by an iterative process that will make sure that the mass equation is also respected. the first step consists in dividing the domain of computation into very small cells and rewriting the differential equations by integrating each sides of both equalities of equation 2.41 on these small cells, this process is called discretization. The momentum equation is rewritten for each individual cell in discretized form as follows :

$$\begin{cases} a_e u_e^* = \sum a_{NB} u_{NB}^* + \Delta y (p_p^* - p_e^*) + b_e \\ a_n v_n^* = \sum a_{NB} v_{NB}^* + \Delta x (p_p^* - p_n^*) + b_n \end{cases} \tag{2.42}$$

The term "b" at the end of each equations represents a momentum source term, Δx and Δy are the length of the sides of an individual cell. The coefficients a_e, a_n, a_s and a_w are numerical coefficient computed during the discretization process and associated with the cells respectively on the east, the north, the south and the west of the current cell noted with the letter P. The summations symbols apply on all the neighboring cells (hence the notation NB), this term is the discretized version of the transport term $\nabla \cdot \rho u u$
At the beginning, an initial guess of the pressure field p^* is made in order to find an estimation of the velocity field by solving the two equations 2.42. This velocity field is not correct as it is probably not a solution to the mass conservation equation. This initial guess of the pressure field generally comes from either a precedent iteration of the algorithm, or a first guest of the velocity is made by applying a time scheme (Runge-Kutta, explicit Euler or Crank Nicholson to name a few of them) on the solution from the precedent time step.
In the next step, a correction to the velocity and pressure field will be computed based on the mass conservation. The correct fields are noted u, v and p, and the corrective terms are noted u', v', p' such that $u = u' + u^*$, $v = v' + v^*$ and $p = p' + p^*$.
The discretized mass conservation leads to :

$$(\rho u)_e \Delta y + (\rho u)_w \Delta y + (\rho v)_n \Delta x + (\rho v)_s \Delta x = 0 \tag{2.43}$$

There are four terms for the four boundaries (east, west, north and south). The value of the corrective term u' and v' can be deduced from the fact that the final field u and v must also be solution of the discretized momentum equation.

$$\begin{cases} a_e u_e = \sum a_{NB} u_{NB} + \Delta y (p_p - p_e) + b_e \\ a_n v_n = \sum a_{NB} v_{NB} + \Delta x (p_p - p_n) + b_n \end{cases} \tag{2.44}$$

subtracting momentum equation 2.44 from equation 2.42 yields :

$$\begin{cases} a_e u'_e = \sum a_{NB} u'_{NB} + \Delta y(p'_p - p'_e) \\ a_n v'_n = \sum a_{NB} v'_{NB} + \Delta x(p'_p - p'_n) \end{cases} \tag{2.45}$$

Then an approximation is made, the term $\sum a_{NB} u'_{NB}$ and $\sum a_{NB} v'_{NB}$ are neglected so that the equations simply become $u'_e = \frac{\Delta y}{a_e}(p'_p - p'_e)$ and $v'_n = \frac{\Delta x}{a_n}(p'_p - p'_n)$, we introduce the following notation to simplify the next equations : $\frac{\Delta y}{a_e} = d_e$. It is still necessary to find an expression for the corrective term of the pressure, which is done by using mass conservation.

Let's call F_i the mass flux coming from a generic neighboring cell noted "i" (so there are four mass flux: F_e, F_w, F_n and F_s), we have that $F_e = F'_e + F^*_e$ with $F'_e = \rho_e d_e \Delta y(p'_p - p'_e)$ (the correction term) and $F^*_e = \rho_e u^*_e \Delta y$. We know that the sum of the corrected max flux F_i is equal to zero, but not the sum of the uncorrected mass flux F^*_i.

$$F^*_e + F'_e - F^*_w - F'_w + F^*_n + F'_n - F^*_s - F'_s = 0 \tag{2.46}$$

$$F^*_e + \rho_e d_e \Delta y(p'_p - p'_e) - F^*_w - \rho_w d_w \Delta y(p'_w - p'_p) + F^*_n + \rho_n d_n \Delta x(p'_p - p'_n) - F^*_s - \rho_s d_s \Delta x(p'_s - p'_p) = 0 \tag{2.47}$$

It is possible to rewrite this equation by rearranging all the terms by nodes :

$$a_p p'_p = \sum a_{NB} p'_{NB} + b \tag{2.48}$$

It can be solved in order to find the values of p' for each cells. the b coefficient depends on the uncorrected mass fluxes at the boundaries of the cell:

- $a_e = \rho_e d_e \Delta y$
- $a_w = \rho_w d_w \Delta y$
- $a_n = \rho_n d_n \Delta x$
- $a_s = \rho_s d_s \Delta x$
- $a_p = \sum a_{NB}$
- $b = F^*_e - F^*_w + F^*_n - F^*_s$

After finding the value of p', all the value of v' can be computed. note that due to the approximation used when establishing the relation between v' and p', the velocity field v will not satisfy the momentum equation and it is generally necessary to iterate the whole process a few time to get the good values. Is is also important to note that due to the approximation, the value of p will be corrected using a relaxation factor α:

$$p = p* + \alpha p' \tag{2.49}$$

In summary, the algorithm can be resumed as follows;

1. An estimation of the pressure field is made by taking the result of the precedent iteration, or the speed is estimated via temporal integration
2. the equations 2.42 are solved to find a rough estimation of the velocity and pressure field, it does not satisfy the mass conservation equation.
3. a corrective term for the pressure field is estimated by solving the equation 2.48, it involves a sum of the uncorrected mass flows.

4. the corrective term for the velocity field is obtained, but due to an approximation, it does not satisfy momentum conservation.

5. other quantities of interest can be transported by the flow via a transport equation. An estimation of their displacement can be made at this point by using the computed velocity field.

6. iterate the whole process with the value obtained for the pressure field as a new starting point until convergence is reached.

The SIMPLE method requires to solve a system, which requires a suitable algorithm. Many of them are directly implemented in Code Saturne, with different rate of convergence:

- Gauss-Seidel (default for velocity, temperature, turbulent variables, passive scalars)
- the Jacobi method
- Conjugate gradient (default for pressure) with algebraic multigrid, jacobi, or polynomial preconditioning
- Algebraic multigrid
- Stabilized bi-conjugate gradient
- GMRES
- other solvers are also available in different libraries

2.2.5 The difference between SIMPLE and SIMPLEC

So far, we have introduced the SIMPLE algorithm, but it is not the one actually used by Code Saturne. The software uses a sligthly modified version of the algorithm called SIMPLEC. The only main difference between the two lies in the relation between the correcting term of pressure and the correcting term of the velocity. This relation was the following for SIMPLE :

$$\begin{cases} u'_e = \dfrac{\Delta y}{a_e}(p_p - p'_e) \\ v'_n = \dfrac{\Delta x}{a_n}(p_p - p'_n) \end{cases} \tag{2.50}$$

And the same relation in the SIMPLEC implementation is written as follows :

$$\begin{cases} u'_e = \dfrac{\Delta y}{a_e - \sum a_{nb}}(p_p - p'_e) \\ v'_n = \dfrac{\Delta x}{a_n - \sum a_{nb}}(p_p - p'_n) \end{cases} \tag{2.51}$$

There is also no need for a relaxation coefficient, and the algorithm is in general 1.2 to 1.3 times faster than the original one. Note that similarly to the SIMPLE algorithm, a bad initial guess of the pressure field can destroy the velocity field.

Chapter 3

Properties of liquid water and simulation parameters

3.1 Introduction

The following chapter will first introduce the different physical properties of liquid water, and how they were implemented in Code Saturne. Each of these properties is in general not a constant and will depends upon different state variables such as pressure or temperature. We will also provide a brief explanation of their physical meaning. After that, the approximations used to simulate heat sources and pressure losses will be explained as well as the mesh geometry.

We are interested to model the following properties :

1. β : the thermal expansion coefficient of water, is defined as follow for any substance : $\beta = \frac{1}{V}(\frac{\partial V}{\partial T})_p$. It measure whether a substance will see its volume increase when the temperature is increased at constant pressure. it has the following units : $[\frac{1}{K}]$

2. c_p : the heat capacity at constant pressure. is defined as follow for any substance : $c_p = (\frac{\partial H}{\partial T})_p$. It measures the amount of heat (in Joule) necessary to increase the temperature of a substance of 1 degree Kelvin at constant pressure. It has the following units : $[\frac{J}{Kg \cdot K}]$

3. λ : the thermal conductivity, is characterizes the ability of the material to conduct heat. The higher the value of λ, the lower the temperature gradient necessary to generate a given heat flux through a portion of the material. It is primarily used in the infamous Fourier's Law : $q = -\lambda \nabla T$. It has the following units : $[\frac{W}{m \cdot K}]$

4. μ : the dynamic viscosity, measures how "sticky" the flow is. For instance, honey has a very high viscosity while that of water is much lower. It is generally defined in term of shear stress in the following relation : $\tau = \mu \frac{\partial u}{\partial y}$ where τ is the shear stress between two "layers" of the flow. It has the following units : $[\frac{kg}{m \cdot s}]$

3.2 Properties of liquid water

3.2.1 The thermal expansion coefficient

Here we will look at the values of β between 0 C° and 100 C°, described in the book "Fundamentals of heat and mass Transfer" in table A.6 (23), in order to find a proper interpolation for a numerical implementation. We used 22 interpolation points and a fourth order polynomial fitted on the data using the polyfit function available in the numpy library.

We get the following graph.

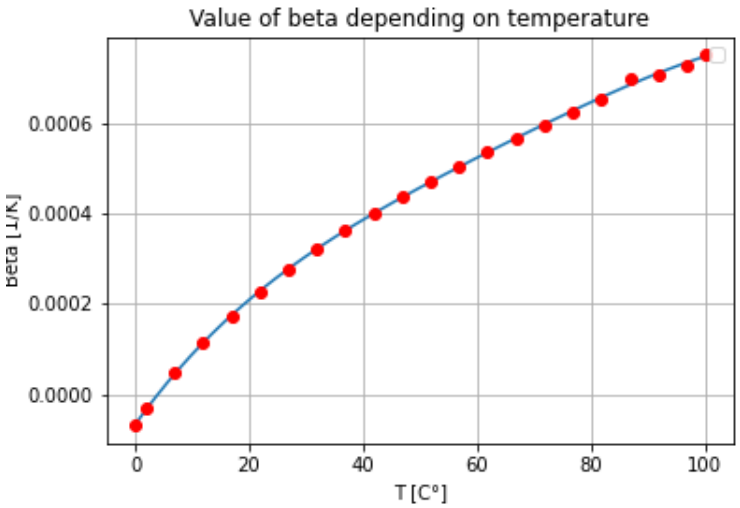

Figure 3.1: values of β depending on temperature

The numpy function returned the following 4th order polynomial :

$$\beta(T) = -8.59 \times 10^{-12}T^4 + 2.25 \times 10^{-9}T^3 - 2.34 \times 10^{-7}T^2 + 1.76 \times 10^{-5}T - 6.61 \times 10^{-5} \quad (3.1)$$

It is interesting to notice that the coefficient becomes negative for a small temperature range near 0 C°.

3.2.2 The heat capacity at constant pressure

The same method was applied to the heat capacity. The interpolation is shown below and one can notice the very low variation on a 100 C°range.

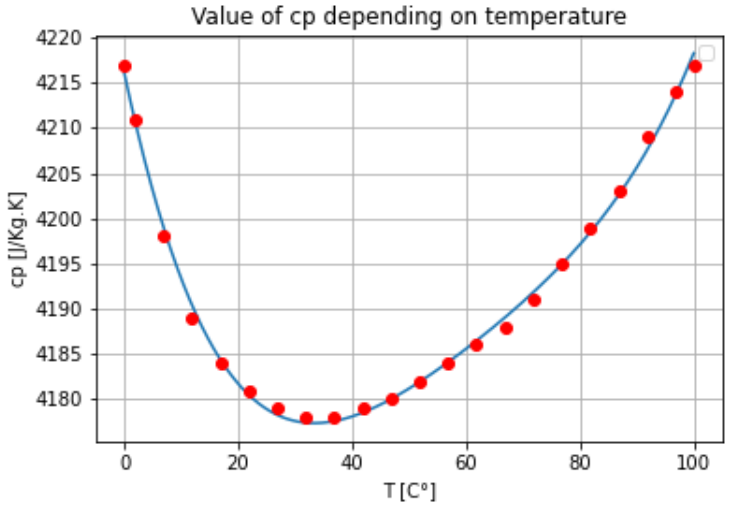

Figure 3.2: values of C_p depending on temperature

The heat capacity reaches a minimum of 4178 $[\frac{J}{Kg \cdot K}]$ and a maximum of nearly 4220. The polynomial computed by polyfit is the following :

$$C_p(T) = 3.27 \times 10^{-6}T^4 - 8.014 \times 10^{-4}T^3 + 7.72 \times 10^{-2}T^2 - 2.96T + 4.21 \times 10^3 \quad (3.2)$$

3.2.3 The thermal conductivity

The graph of the interpolation points and the interpolation polynomial are shown just below. It is assumed that the pool only contains pure water as a different chemical composition could change the values. :

$$\lambda(T) = 1.094 \times 10^{-10}T^4 - 2.91 \times 10^{-8}T^3 - 4.86 \times 10^{-6}T^2 + 1.77 \times 10^{-3}T + 5.69 \times 10^{-1} \quad (3.3)$$

Water has a relatively low thermal conductivity compared to other materials like metals, but has a high conductivity if it is compared to other fluids (excepted molten metals). Conductivity increases with temperature on the observed range.

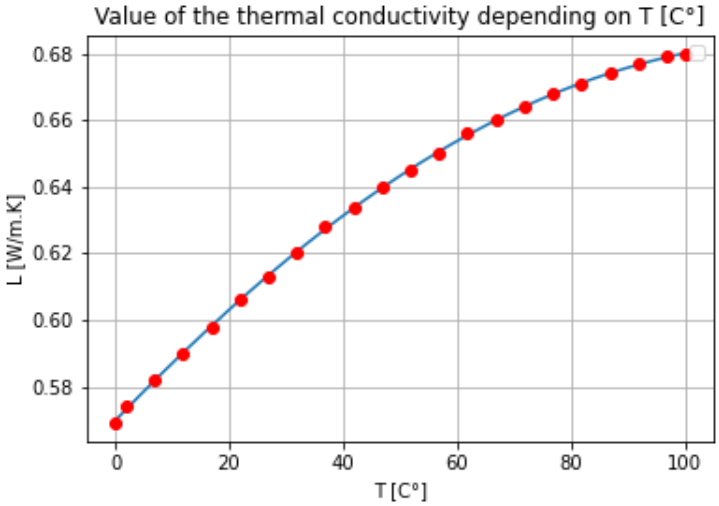

Figure 3.3: values of λ depending on temperature

3.2.4 The dynamic viscosity

As explained before, the dynamic viscosity μ is used in a constitutive law called Newton's law to relate the shear stress and the rate of deformation (the partial derivative of a speed component with respect to the direction perpendicular to that component). It is measured with various types of viscometers and rheometers. The momentum transfer in liquid is caused by attractive forces between molecules in the fluid. Viscosity tends to decrease with temperature in gases and increase in liquid.

Here are the interpolation polynomial and the graph of the data point for the dynamic viscosity of water. The red points are the interpolation points and the blue curve is the polynomial as for the other graphs.

$$\mu(T) = 2.86 \times 10^{-11}T^4 - 8.05 \times 10^{-9}T^3 + 8.93 \times 10^{-7}T^2 - 5.2 \times 10^{-5}T + 1.74 \times 10^{-3} \quad (3.4)$$

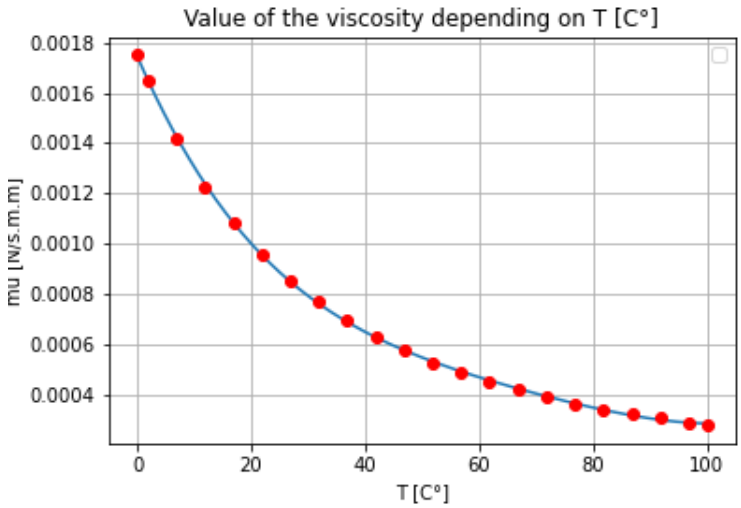

Figure 3.4: values of μ depending on temperature

3.3 The heat source

The source of energy that drives the convection in the pool is the heat coming from the radioactive decay of the unstable isotopes contained in the spent rods. Bel V gave a value of 70 kW of heat produced by each assembly coming straight from the core. The heat transfer between the assembly and the water has been modelled using three different techniques of increasing complexity. The two first models were later implemented in the simulations:

1. a simple uniform heat source distribution
2. a sinusoidal heat source distribution where the heat release rate is maximal at the center of the assembly an equal to zero at the top and the bottom
3. a heat release rate that depends locally on the temperature of the flow, the temperature of the rods, and a coefficient of heat transfer h that depends on the velocity.

The heat released by the rods is modelled as a heat source term in the energy equation. It as the unit of a power density $[\frac{W}{m^3}]$. It is constant for the uniform case, and it depends on the height Z in the sinusoidal case.
In order to compute the value of these three heat source terms at each point, it is necessary to know the dimensions of an assembly. Bel V was also able to provide the following estimates :

- a height of 4m
- a square cross section of 20cm

3.3.1 The uniform distribution

In this simple case, it is considered that all the heat released by the assembly goes directly in the surrounding water. The spatial distribution is assumed to be uniform and the heat release rate doesn't depend on the properties of the flow or its temperature. The value of the heat source term can be easily computed solely from the dimensions of an assembly.

$$Q = \frac{P}{V_w} = \frac{70000}{h \times L^2 \times \phi} = \frac{70000}{4 \times 0.2^2 \times \phi} = \frac{437500}{\phi} \frac{W}{m^3} \tag{3.5}$$

Where ϕ is the porosity coefficient, aka the ratio between the volume of water and the total volume in an assembly. V_w is the volume of water in an assembly.

3.3.2 The sinusoidal distribution

In reality, the heat release profile is not uniform along the vertical axis, but rather look like a sinus. This comes from the fact that the heat source is proportional to the concentration of radionuclide in the assembly. This concentration actually depends on the local power of each part of the assembly, which itself depends on the local neutron flux when it was producing energy in the core of the reactor. This flux can be computed analytically using the diffusion approximation in a nuclear reactor (24). For instance, in the case of an idealized finite cylinder reactor, the flux profile is given by :

$$\psi(r,z) = J_0(\frac{v_0 r}{R})cos(\frac{\pi z}{H}) \tag{3.6}$$

With R and H the corrected radius and height of the reactor, J_0 the Bessel function of the first kind and v_0 the first root of J_0. Here we neglect the flux variation in the radial direction as the width of an assembly is generally less than a tenth of the width of the whole core. This case require to integrate a sinusoidal function. Following the hypothesis made in the introduction of this section, the heat source term can be written under this form :

$$Q = A\sin(\frac{\pi z}{z_{max} - z_{min}})[\frac{W}{m^3}] \tag{3.7}$$

where $z_{max} - z_{min}$ is equal to 4. The double integration of this function on the domain should be equal to the total thermal output, which is equal to 70 kW by hypothesis.

$$P = \phi \int_{z_{min}}^{z_{max}} \int_{x_{min}}^{x_{max}} \int_{y_{min}}^{y_{max}} A\sin(\frac{\pi z}{z_{max} - z_{min}})\, dx\, dy\, dz \tag{3.8}$$

$$= \phi \int_0^4 \int_0^{0.2} \int_0^{0.2} A\sin(\frac{\pi z}{4})\, dx\, dy\, dz \tag{3.9}$$

$$= \phi \int_0^4 0.04A\sin(\frac{\pi z}{4})\, dz \tag{3.10}$$

$$= \phi 0.04A[-\frac{4}{\pi}cos(\frac{\pi z}{4})]_0^4 \tag{3.11}$$

$$= \phi 0.04A(\frac{4}{\pi} + \frac{4}{\pi}) \tag{3.12}$$

$$A = \frac{\pi P}{0.04 \times 8 \times \phi} = \frac{\pi P}{0.32\phi} \tag{3.13}$$

For an output of 70 kW, the constant A is equal to $\frac{687223}{\phi}$. It is possible to give a different heat distribution to each assembly. This can be done directly in the Code Saturne GUI, or via a user script.

3.3.3 The temperature dependent distribution

In the two precedent cases, it was assumed that the heat flux was independent of the temperature and the velocity of the flow. In reality, the heat flux going from the rods to the water can be modelled with a heat transfer coefficient h, using the following formula.

$$Q = S_{rods} \times h \times (T_{in} - T_{water})[\frac{W}{m^3}] \tag{3.14}$$

Where S_{rods} is the total surface of exchange between the water and the rods in a cubic meter of assembly, h is the heat transfer coefficient, T_{in} is the average temperature in the rods, and T_{water} is the temperature of water at a certain distance of the rods wall. The surface is computed as follows:

$$S_{rods} = N_{rods} \times 2\pi \times r = 8,04m^2 \tag{3.15}$$

The water temperature is different at each locations and is one of the unknown of the simulation. The flux Q at a given time t can be computed using the local value of T_{water}. The temperature of the rods T_{in} can be estimated using the conservation of energy principle. Here, it is assumed that

this temperature is uniform across the thickness of the rod. In reality, this is not true as the thermal conductivity of uranium oxyde UO_2 is quite low, but it allows for a simpler model:

$$\rho_{rods} c_p V_{rods} \frac{\partial T_{in}}{\partial t} = Q_{decay} - S_{rods} \times h \times (T_{in} - T_{water}) \tag{3.16}$$

Where $V_{rods} = 256 \times \pi \times r_{rods}^2$ is the volume occupied by the rods in a cubic meter of assembly, c_p and ρ_{rods} are the average heat capacity and the average density of a rod, and Q_{decay} is the volumetric heat flux due to the disintegration of the radionucleides : $Q_{decay} = \frac{P}{V} = \frac{70000}{h \times L^2} \frac{W}{m^3}$

The equation 3.16 must be integrated over time in each point of the assemblies so that the heat flux Q in equation 3.14 can be estimated at each time step. It is still necessary to find and expression for the global heat transfer coefficient h. It can be estimated using an empirical correlation on the Nusselt number, like the one given below (see heat and mass transfer 7th edition p 442 (23)):

$$Nu = 0.664 \times Re^{\frac{1}{2}} Pr^{\frac{1}{3}} \tag{3.17}$$

The coefficient h can be estimated using the following definition : $h = \frac{Nu \times k}{L}$, with k the thermal conductivity of water, and L the caracteristic length also used in the definition of the reynold number. Here it will be set to the length of a rod (4 meters). Pr is the Prandlt's number ($Pr = \frac{\nu}{\alpha}$) and Re is the Reynold's number ($Re = \frac{\rho u L}{\mu}$).

It is important to note that equation 3.17 only provides a rough estimation of the real value of the Nusselt number. It was obtained via the integration of an analytical solution of the temperature profile for a plate in a laminar flow, which is not the case here. Furthermore, this formula gives a heat flux equal to zero when the velocity is null. It does not reflect reality, as conduction would still occur between the hot wall and the surrounding water. So another correlation must be found for very low velocity flows.

This methodology was not implemented in Code Saturne as it would be necessary to integrate an additional scalar field over time (T_{in}), so only the two first heat flux models will be considered in the rest of this master thesis. The reason why it was developed here is to show to the reader a way to improve the accuracy of the heat transfer.

3.4 The porosity

Due to the presence of fuel rods in the assemblies, the actual density of water in the spent fuel is lower than in the rest of the pool (it is simply due to the fact that the space is actually limited). It is possible to directly implement a porosity coefficient in the graphical user interface of Code Saturne. The computation of this coefficient is mainly based on a geometrical hypothesis.

If an assembly is 4 meters long and has a square section of 20 × 20 centimeters, and that the assembly contains 256 rods which are 1 cm in diameter, the actual free volume (the volume occupied by water) is equal to 0.079 cubic meters for a total volume of 0.16 cubic meter. The ratio between these two volumes is the porosity coefficient and is equal to 0.493.

The general formula for the porosity in our case is :

$$\phi = \frac{V_{assembly} - V_{rods}}{V_{assembly}} \tag{3.18}$$

$$= \frac{H \times L^2 - n_{rod} H \pi r^2}{H \times L^2} \tag{3.19}$$

$$= 1 - \frac{n_{rod} H \pi r^2}{H \times L^2} \tag{3.20}$$

3.5 Validation of the uniform and sinusoidal heat flux

A small simulation was done using the sinusoidal and the uniform models to make sure that the implementation in Code Saturne works properly, and the following result was obtained :

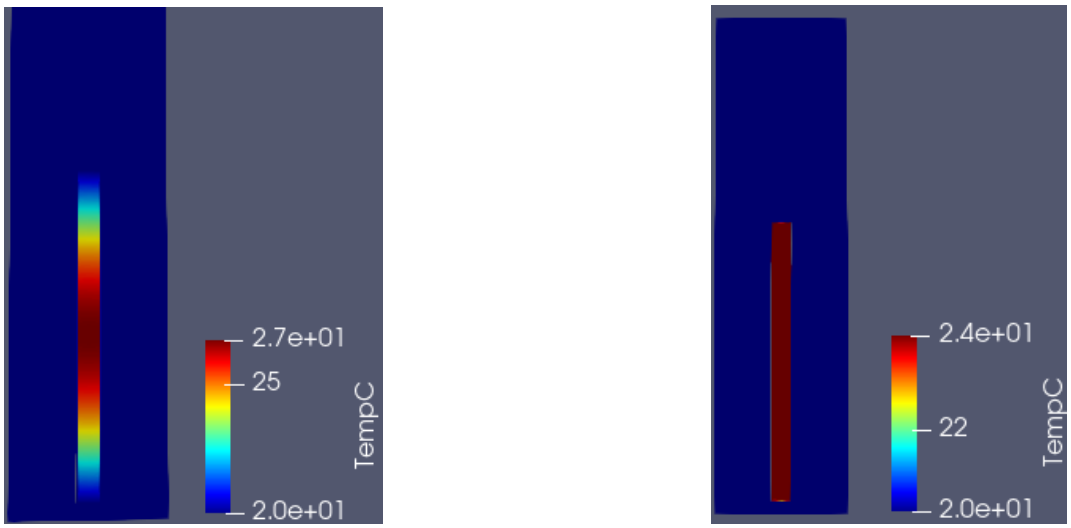

(a) (b)

Figure 3.5: temperature field in a simplified domain for the sinusoidal (a) and uniform (b) heat release profile in a simplified domain

In figure 3.5, a sinusoidal and a uniform heat source were implemented using the equations described before, the value of ϕ was set to 0,493 in the channel via the Code Saturne GUI (this value will be explained a bit later). The simulations used a time step of 0.2 seconds, for a duration of 20 seconds. The gravity field was set to $0[\frac{m}{s^2}]$ to avoid any convective effect, and the velocity field is equal to zero everywhere. Indeed, the main purpose here is to check that the value of the water temperature is coherent with the power released by a real assembly. It can be seen that the temperature field is higher in the middle of the left picture than on the top and the bottom of the assembly, it shows that the implementation of the sinusoidal heat release profile is correct. Indeed, the temperature field is directly proportional to the heat release rate in the absence of convection because of the following equation :

$$\Delta T = Q \times \Delta t \tag{3.21}$$

Now, let's see if the uniform heat source heats the water the same way a 70 kW spent fuel assembly would. The temperature inside a real assembly after 20 seconds is computed as follows :

$$\Delta T = \frac{t \times P}{V \times \phi \times \rho \times c_p} = \frac{20 \times 70000}{4 \times 0.2^2 \times 0.493 \times 1000 \times 4180} = 4.24C \tag{3.22}$$

When looking at the uniform profile on the right, the temperature of the water in the pool is 20 C° (this value was imposed via the GUI), and the temperature of the water in the vertical assembly is equal to 24 C°, which corresponds to the expected increase of 4 C°.

3.6 The volumetric head loss

3.6.1 The equations for the head losses

Due to the limitation in the cell size, it is not possible nor practical to simulate the individual channels of the assemblies. Instead of trying to resolve each individual rod, it was decided to implement an assembly as an area with a given porosity and a volumetric head loss, which is implemented in the momentum equation as the $-\rho KU$ term, where K is a 3×3 tensor with only diagonal terms.

An assembly is 4 meters high and has a square cross section with a length of 20 cm. It is composed of 264 fuel rods. The square root of 264 is equal to 16.24, so it was decided to consider an assembly with 256 rods so that they could be arranged in a 16×16 configuration.

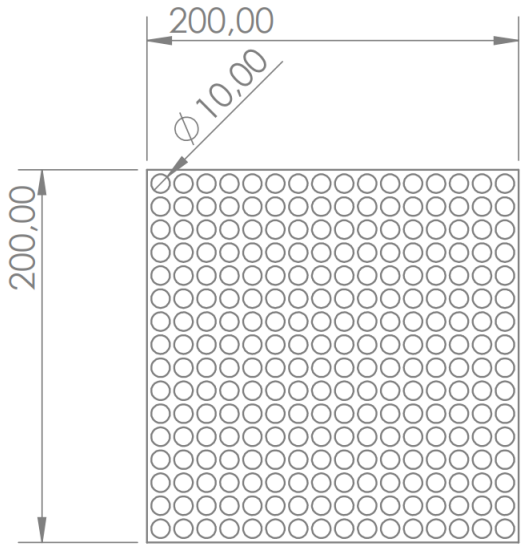

Figure 3.6: cross section of a fuel assembly

In the following computation, we will follow the procedure that was developed in the master thesis Balfroid et al (25).
As explained just above, K is a tensor that can be expressed as follows. :

$$K = \begin{bmatrix} K_{11} & 0 \\ 0 & K_{33} \end{bmatrix} \tag{3.23}$$

Where K_{11} is the horizontal pressure loss coefficient, and K_{33} is the vertical pressure loss coefficient, both must be positive because a positive speed must induce a negative pressure gradient. The ρKU term has the unit of a force per unit volume (the same as a pressure gradient), which will allow me to find an expression for it that depends on the speed components, the water fraction ϕ in the assembly, and the geometrical parameters d and h (respectively the diameter and the height of a fuel rod):

$$\rho K_{11} u = F = \frac{1}{\phi} n_b D_x [\frac{N}{m^3}] \tag{3.24}$$

with $n_b = \frac{4(1-\phi)}{\pi d^2 h}$, the number of rod with a length h in a cubic meter of assembly.
D_x is the drag coefficient, it can be computed using an expression for the adimentional frag coefficient $C_D = \frac{D_x}{\frac{1}{2}\rho u^2 S_c}$, where S_c is the cross section of a rod (so $S_c = hd$) and it gives the amplitude of the force that a rod of height h exerts on the flow.

To understand why there is a ϕ in the denominator of the right side of equation 3.24, it is necessary to introduce a simple example. If we take a channel with a square cross section of $1m \times 1m$ and a length of 10 meters, and that a $1m^3$ assembly is put in the middle of the channel with the rods perpendicular to the flow of water, then it is possible to compute the force that the flow apply on the rods if the speed of the flow is known, and by Newton's third law, the force that the rods apply on the water. As the porous region (the assembly) considered here has a volume of $1m^3$, this force is equal to $n_b D_x$. As the speed of the water doesn't change inside the porous region (the cross section and the density remains constant), it means that this force is balanced by the difference of pressure between the beginning and the end of the channel :

$$F = A_{crossP}(p_{start} - p_{end}) \tag{3.25}$$

Where A_{crossP} is the cross section. Here, the cross section A_{crossP} is not the cross section of the channel (which is equal to $1m^2$), but the cross section where the assembly is located and filled with water. The thing is that in the computations, we only care about the cross section of the channel A_{crossC}, so we have to use the following relation :

$$A_{crossP} = \phi A_{crossC} \tag{3.26}$$

If the cross section A_{crossC} is multiplied by ϕ, then it means that the pressure gradient must be divided by ϕ in order to keep the same force :

$$F = A_{crossC}\phi\frac{(p_{start} - p_{end})}{\phi} \tag{3.27}$$

This explains why there is a $\frac{1}{\phi}$ in front of equation 3.24

An expression for C_D can be found in the literature for a viscous flow past a cylinder (26) :

$$C_D = \frac{-8\pi}{Re_d \times (\frac{1}{2} - \gamma - log(\frac{Re_d}{8}))} \tag{3.28}$$

$$= \frac{-8\pi\mu}{\rho ud \times (\frac{1}{2} - \gamma - log(\frac{Re_d}{8}))} \tag{3.29}$$

If this equation is put inside the equation 3.24, I get the following :

$$\rho K_{11} u = \frac{1}{\phi} n_b D_x = \frac{1}{\phi}\frac{4(1-\phi)}{\pi d^2 h} \times \frac{\rho u^2 dh}{2} \times \frac{-8\pi\mu}{\rho ud \times (\frac{1}{2} - \gamma - log(\frac{Re_d}{8}))} \tag{3.30}$$

which gives the following value for K_{11}:

$$K_{11} = \frac{-16\mu(1-\phi)}{\rho\phi d^2(\frac{1}{2} - \gamma - log(\frac{\rho ud}{8\mu}))} \tag{3.31}$$

Very similarly, it is also possible to find an expression for K_{22} by using the adimentional coefficient of friction C_f. As with K_{11} , it is possible to write the following :

$$\rho K_{22} v = F = \frac{1}{\phi} n_b D_y [\frac{N}{m^3}] \tag{3.32}$$

With $D_y = \int \tau_w \, dA$

$$D_y = \int_0^h \int_0^{2\pi} \frac{1}{2} C_f(y) \rho v^2 r \, d\theta \, dy \tag{3.33}$$

$$D_y = \frac{1}{2}\rho v^2 \pi d \int_0^h C_f(y) \, dy \tag{3.34}$$

The coefficient C_f is estimated via a flat plane approximation found in (27), the tubes are not flat planes, but this approximation gives an order of magnitude of the head loss :

$$C_f = \frac{0.664}{\sqrt{Re_h}} = \frac{0.664}{\sqrt{\frac{|v|y}{\nu}}} \tag{3.35}$$

This equation is injected in expression 3.36 and integrated to give the next result:

$$D_y = \frac{0,664}{2}\rho v^2 \pi d \sqrt{\frac{\nu}{|v|}} \int_0^h \frac{1}{\sqrt{y}} \, dy \tag{3.36}$$

$$D_y = 0.664 \rho v^2 \pi d \sqrt{\frac{\nu h}{|v|}} \tag{3.37}$$

and then, the final expression for K_{22} is found :

$$\rho K_{22} v = \frac{4(1-\phi)}{\pi d^2 h \phi} \times (0.664 \rho v^2 \pi d \sqrt{\frac{\nu h}{|v|}}) \tag{3.38}$$

$$K_{22} = 2.656 \frac{(1-\phi)}{d\phi} \sqrt{\frac{\nu |v|}{h}} \tag{3.39}$$

3.6.2 The numerical implementation of the head losses

These two coefficients were implemented in the CD_user_head_losses.c file in the SRC folder. The fluid properties were first extracted from the data structure:

```
const cs_real_3_t *cvara_vel = (const cs_real_3_t *)(CS_F_(vel)->val);
const cs_real_t *cvara_mu = (const cs_real_t *)(CS_F_(mu)->val);
const cs_real_t *cvara_rho = (const cs_real_t *)(CS_F_(rho)->val);
const cs_real_t diam = 0.01;
const cs_real_t h = 4;
const cs_real_t ushift = 0.001;
const cs_real_t eulconst = 0.577;
const cs_real_t *cvara_poro = (const cs_real_t *)(CS_F_(poro)->val);
```

and the values of the CKU array are then updated after the computations :

```
for (cs_lnum_t i = 0; i < zone->n_elts; i++) {
    cs_lnum_t c_id = zone->elt_ids[i];
    cs_real_t v1 = cvara_vel[c_id][0];
    cs_real_t v2 = cvara_vel[c_id][1];
    cs_real_t v3 = cvara_vel[c_id][2];
    cs_real_t mu = cvara_mu[c_id];
    cs_real_t rho = cvara_rho[c_id];
    cs_real_t poro = cvara_poro[c_id];

    cs_real_t logarden1 = log((abs(v1)+ushift)*diam/(8*(mu/rho)));
    cs_real_t logarden2 = log((abs(v2)+ushift)*diam/(8*(mu/rho)));
    cku[i][0] = -(16*mu*(1-poro))/(rho*poro*(1/2 - eulconst-logarden1)*cs_math_sq(diam));
    cku[i][1] = -(16*mu*(1-poro))/(rho*poro*(1/2 - eulconst-logarden2)*cs_math_sq(diam));
    cku[i][2] = 2.656*(1-poro)/(diam*poro)*sqrt((abs(v3)*mu)/(rho*h));
}
```

In order to make sure that the equations where implemented correctly in Code Saturne, a simulation of a one dimensional flow in a channel was implemented. Note that the implementation of the head losses in the x direction differs a bit from the formula developed before as there is an additional term in the formula : u_{shift}. Its value was chosen so that the numerator is never equal to zero, which would lead to an error.

$$u_{shift} > -|u_1| + \frac{8\nu}{d} e^{\frac{1}{2}-\gamma} \tag{3.40}$$

With $u_1 = 0$, $d = 0.01$ and $\nu = 10^{-6}$, we get that the offset should be equal to $7,4 \times 10^{-4}[\frac{m}{s}]$, it was rounded up to 0,001.

The domain is a $1m \times 10m$ pipe with a head loss area comprised between $x = 2$ and $x = 8$ (the red area in the figure). The flow enters on the left and exit on the right. The mesh has a spatial resolution of 1 cm, and the code makes 300 iterations to ensure a good convergence. A slip condition was implemented on the two walls in order to make sure that there is not head losse other than the volumetric one.

Figure 3.7: domain for the head loss test

In order to check the correct implementation of the head losses, two measurement points where set in (1, 0.5) and in (9, 0.5) in the middle of the two areas without head loss to measure the pressure

difference between the entry and the exit of the pipe. Knowing that the pressure loss zone is 6m long, the theoretical pressure drop should be equal to the following expression :

$$\Delta p = \Delta x \rho u K = 6 \rho u K \tag{3.41}$$

with K the coefficient computed in the precedent section, u the speed and ρ the density of water.

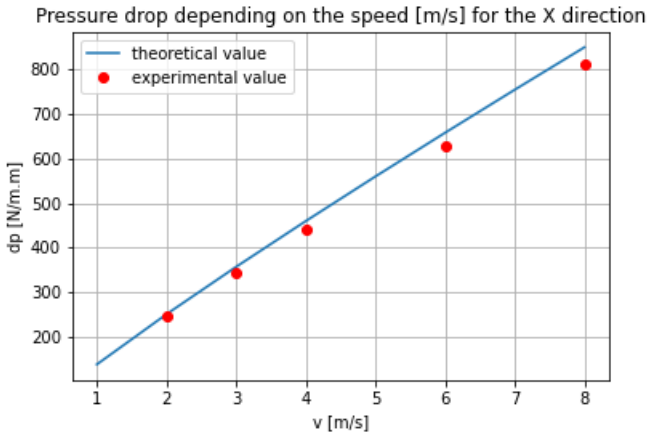

Figure 3.8: comparison between computed and theoretical value of Δp

On figure 3.8, the drop of pressure computed by Code Saturne for 5 values of the speed of the flow was compared with the theoretical formula in 3.41. The prediction are fairly accurate even if there is a small difference between the computed and the theoretical value for high speed flows. It shows that the implementation of the pressure drop in the x direction is correct.

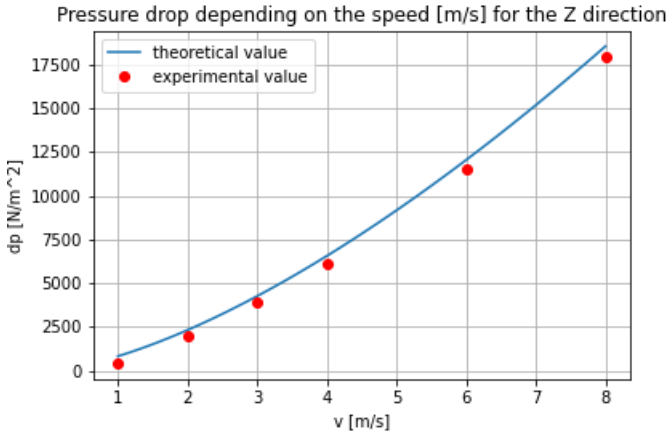

Figure 3.9: comparison between computed and theoretical value of Δp

Similarly, the vertical pressure drop is shown on figure 3.9. Here the accuracy is even better than before for high speed flows.

3.6.3 The mesh

The domain we are working on is a simple rectangle which represents a vertical section of the pool. A view of the rack from the top is displayed on picture 3.10, and the cut called "A" represent the 2D domain we will consider in this study. The mesh generation is a little bit trickier than simply taking a rectangle and then generating the meshing, and that's because we have to find a way to implement the walls between each assembly. To do that, we had to subdivide the domain in a lot of smaller rectangle that could be generated separately and then assembled in one big final mesh.

Depending on how many assemblies are being simulated, the number of rectangular sub-meshes will vary. In our case, the domain contains 8 assemblies and is sub-divided in 48 sub-meshes. It is represented in the figure 3.11, where the walls between the assemblies are represented by crossed out boxes. It is important to note that these walls are actually empty and don't contain any mesh so that a non slipping condition (speed vector equal to zero) can be applied on the four boundaries. Each sub-mesh has its own attributed number, starting from the bottom left, and ending at the upper right corner of the global mesh. The sub-meshes containing the assemblies are also numbered using the letter D (for instance, D1 is the first assembly, D2 the second, et cetera).
The formula to find the number of submesh is simply $n_{mesh} = 5n + 8$ with n the number of assemblies.

The dimensions of the boxes are key parameters of this study and are noted by their axes (dx or dy) followed by an index. Bel V provided some typical values, they are listed just below :

- dy1 : the distance between the floor of the pool and the bottom of the rack: 16 cm.
- dy2 : the height of an assembly : 4 meters.
- dy3 : Water height above the racks: 8 meters
- dx1 : the distance between the wall and the closest assembly : it is a parameter of this master thesis, either 16cm or 24cm.
- dx2 : The thickness of a wall separating two assemblies : here it has been set to 8 mm.
- dx3 : the width of an assembly : 20 cm.

The thickness of the domain doesn't matter much as the flow is 2 dimensional. The mesh will be one element thick anyway.

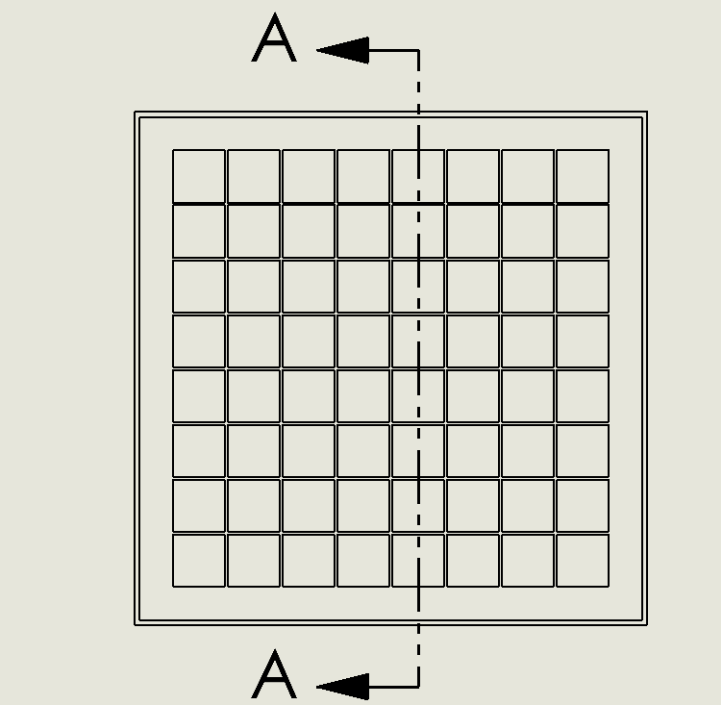

Figure 3.10: view from the top of the rack

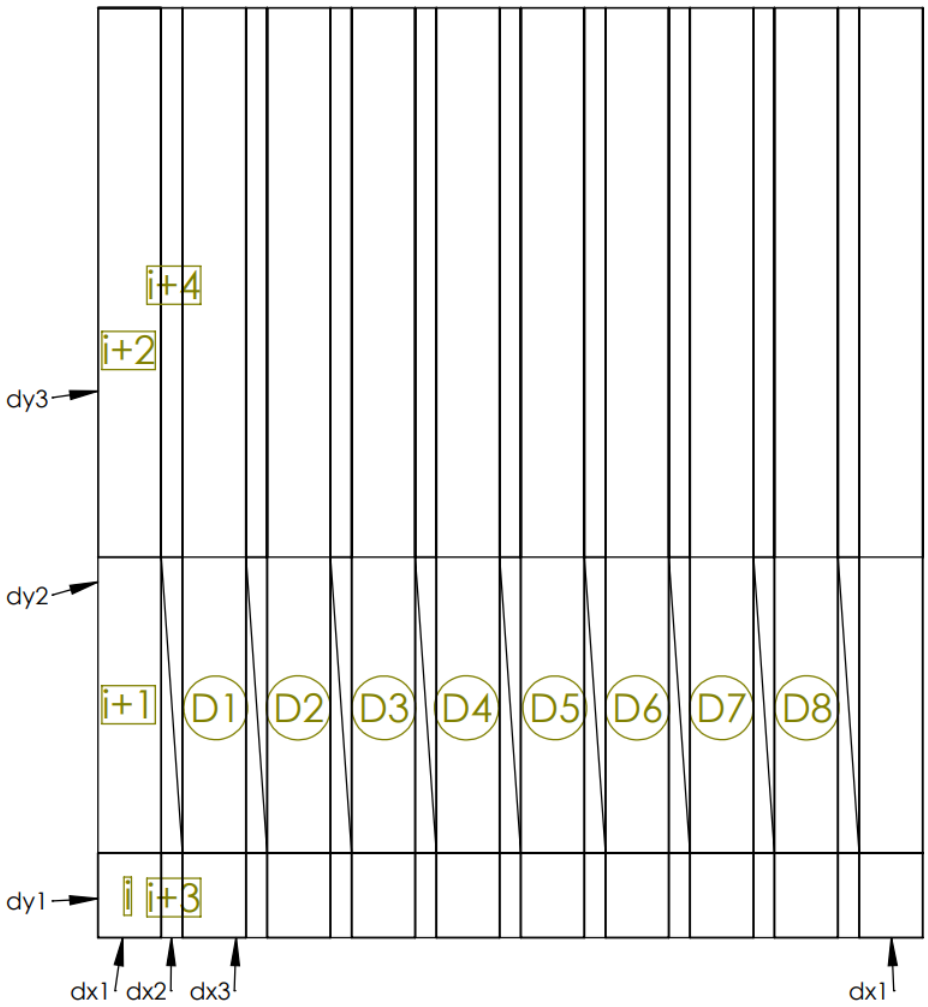

Figure 3.11: schematic of the mesh (not on scale)

To effectively create the mesh, we start by using the "Geometry" module in Salome where we can draw the 48 rectangles separately. We can then extrude them and gather the different faces into groups, which is very useful to later give a boundary condition to each of them. The rectangles are then individually meshed in the module "Mesh" (still in Salome) before being merged together in one big file that we can use in Code Saturne.

The construction of the mesh was made on a personal computer via a virtual machine, it can't be done on the clusters as Salome require a graphical user interface to build the different files. The refinement of the mesh (size of the individual elements) is limited by the available RAM and by the computation time. In order to keep the computation time below two days, the size of the elements was set to $4mm \times 4mm$.

Chapter 4

The results

4.1 Selected parameters and boundary conditions

Now that all the important parameters and approximations needed for the simulations have been defined and explained, it is time to set the configuration of the nuclear waste in the channels. The spatial resolution is 4mm as stated before, and it is mainly due to the fact that the calculation time can't be higher than two days. The impact of four parameters are studied here:

1. the distance between the walls and the rack; two values are considered here: 16cm and 24cm
2. the power of the assemblies (high power or low power)
3. the configuration of the assemblies in the rack
4. the heating profiles (uniform and sinusoidal)

In this study, two type of heating profiles are considered :

- uniform heating profile, new waste : P(x,z) = $\frac{437500}{\phi}[\frac{W}{m^3}]$
- sinusoidal heating profile, new waste : P(x,z) = $\frac{687233}{\phi} sin(\frac{\pi z}{z_{max}-z_{min}})[\frac{W}{m^3}]$

The two cases above are for an assembly that contains fresh spent nuclear fuel (power of 70kW), but in the simulations, some channels will also contain older nuclear wastes. For this reason, they will be configured with a heating profile whose thermal output is divided by two (so 35 kW), or by four (17,5 kW):

- uniform heating profile, 35kW : P(x,z) = $\frac{437500}{2\phi}[\frac{W}{m^3}]$
- sinusoidal heating profile, 35kW : P(x,z) = $\frac{687233}{2\phi} sin(\frac{\pi z}{z_{max}-z_{min}})[\frac{W}{m^3}]$

Before starting the simulations, it is still necessary to precise the boundary conditions selected for this study. The rack contains 8 nuclear assemblies. All the walls are set to a non slip condition, and the surface of the pool is free so we just imposed the normal component of the speed (normal to the surface) to be equal to zero. The initial temperature is set to 20 degree Celsius, the walls are adiabatic and the initial speed is set to 0 everywhere. It is also really important not to forget to impose a uniform gravitational field with an acceleration of -9.81 $[\frac{m}{s^2}]$. This can be done directly on the GUI of Code Saturne, and it is very quick to check if the functionality works as it should produce a strong vertical pressure gradient (the so called hydrostatic pressure).

Five configurations will be studied. In these configurations, each of the 8 assemblies will contain one of two power levels depending whether the rack has a high or a low power output.

- high power output rack : the assemblies contain either a 70kW or 35kW power source
- low power output rack : the assemblies contain either a 35kW or 17.5kW power source

The results are presented in three rounds of simulations, and in each round five nuclear waste configurations are studied.

In the first round of simulations, a low power output rack is considered (35kW and 17,5kW), the distance from the wall to the rack is 16cm and both sinusoidal and uniform heat profiles are studied.

In the second round of simulations, a high power output rack is considered (70kW and 35kW), the distance from the wall to the rack is 16cm, and only the sinusoidal heating profile is studied.

In the third round of simulations, a high power output rack is considered (70kW and 35kW), the distance from the wall to the rack is 24cm, and only the sinusoidal heating profile is studied.

The 5 configurations are describes here below.

- Config 1 : uniform distribution: all the 8 channels contain the same nuclear waste (high power output).
- Config 2 : centered distribution: the 4 innermost channels contain nuclear wastes with a low power output, while the four outermost channels contain nuclear wastes with a high power output.
- Config 3 : asymmetrical distribution: the 4 channels on the left contain nuclear wastes with a low power output, while the four channels on the right contain nuclear wastes with a high power output.
- Config 4 : mixed distribution: each channel has a different heating profile than its neighbors, so the first one on the left contains nuclear wastes with a high power output, the second one contains nuclear wastes with a low power output, the third a high power and so on.
- Config 5 : inverted centered distribution : the 4 innermost channels contain fresh nuclear wastes with a high power output, while the four outermost channels contain nuclear wastes with a low power output.

4.1.1 Time step and Courant number

The time step used can be estimated using the Courant number. When a simulation with a mesh is integrated using an explicit integration scheme (which is the case here, the velocity is integrated using a second order upwind scheme (SOLU), and the other transported quantities are integrated with a first order upwind scheme), it is important to pay attention to the fact that for the simulation to be accurate, the distance traveled by a water molecule during a time step can't be higher than the spatial resolution, otherwise the results will not be correct. Mathematically speaking, the Courant number in a 2D grid is defined as follows :

$$Co = \frac{dt \times u_{max}}{dx} + \frac{dt \times v_{max}}{dy} < 1 \tag{4.1}$$

Here, $dx = dy = 0.004m$. The max value of u and v (respectively the x and y components of the velocity vector) can only be estimated using assumptions on the flow. Here, it is reasonable to assume that the maximum value will be reached under the assemblies or in the assemblies themselves and that it will not exceed 1 $\frac{m}{s}$. This initial guess must be confirmed with the first results. If we inject these values in the equation, we get

$$dt < \frac{0.004}{2} = 0.002s \tag{4.2}$$

The time step must be below $dt = 0.002s$, here we will consider a value of 0.001s and 0.0005s in order to check the real maximum velocity, and then see if there is a difference between the simulations done with these two time step.

In the following descriptions, a "reflux" is the term used when the flow of water in one of the

channels with an assembly in it is directed toward the ground (the water goes down). The two channels that don't contain any assembly (on the extreme left and the extreme right) are referred to as "free channels". The channels containing an assembly are sometimes referred to by their number (D1, D2, D3, etc) as defined at the end of section 3.6.3

4.1.2 Sensors location

We were only able to capture two snapshots for each simulation as the clusters of the university take four hours to process one. So in order to gather more data about the speed of the flow and the temperature, 30 sensors were set in the channels. There is a sensor on the top, a sensor in the middle and a sensor at the bottom of each channel, and their x-z coordinates are displayed in Appendix A.

4.1.3 Methodology of the analysis

In the next section, the temperature and velocity fields will be analyzed from snapshots and pictures of the streamlines taken at different times for each simulation. The sensors described in the previous subsection will make it possible to establish graphs of the local evolution of temperature and speed at several specific points. For each of the simulations carried out in the first simulation round, we will first describe the flow using snapshots of the temperature and velocity field in order to make assumptions about the general behavior of this flow. Then, we will use the graphs to confirm these hypotheses and find the maximum speed and temperature among the analyzed points.

4.2 First simulation round: 35kW and 17.5kW assemblies

4.2.1 Configuration 1 : rack full of identical nuclear wastes at 35 kW outputs

50 seconds simulations

The reader can see the temperature field and the velocity magnitude field of a 50 seconds simulation with a time step $dt = 1ms$ for the sinusoidal heating profile case. Each channel has the same fresh nuclear waste in it, so the power output is the same everywhere at 35kW.

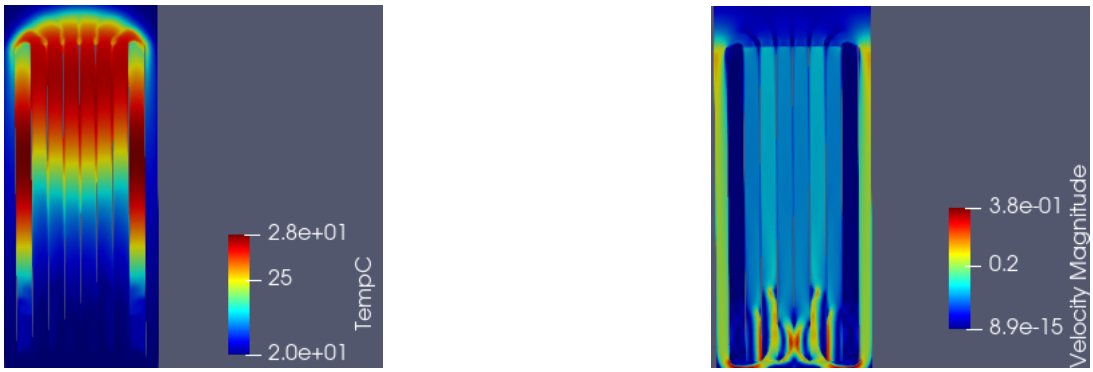

(a) (b)

Figure 4.1: Simulation for $dt = 1ms$ and $t = 50s$

Before comparing this result with a simulation with a smaller time step, it could be interesting to look at the apparent features of the flows. the first important thing to note is that the flows in the six inner assemblies seems to follow a very similar pattern:

1. the hot water climbs up due to the difference in density induce by the higher temperature (buoyancy driven flow).

2. This hot water is thus replaced by cold water, allowing the cooling of the assembly elements

3. The speed is quite uniform accross the x and z direction in the upper part of the channels, but it becomes more complex in the lower part, where the cold water is flowing in.

The second most notable feature is the nearly absence of flow in the two assemblies next to the free channels (D1 and D8). It seems like the flow coming out of the other channels is blocking the water from these two channels to exit. It is even more clear when we look at the velocity field, the vertical speed is nearly equal to zero in D1 and D8.

The norm of the speed reaches a maximum of 0.38 $\frac{m}{s}$ in the bottom of the pool, which gives a Courant number equal to 0,095 for $dt = 1ms$. The time step is thus small enough as the Courant number is far below one. We also decided to conduct the same simulation (sinusoidal heat profile and 8 assemblies in parallel) with a smaller time step of 0.5 ms to see how the simulation results would be impacted. The velocity profile has been displayed on figure 4.2 and it is almost identical to the one displayed on figure 4.1b so we can say that a time step of 1ms is good enough for an integration period of 50 seconds.

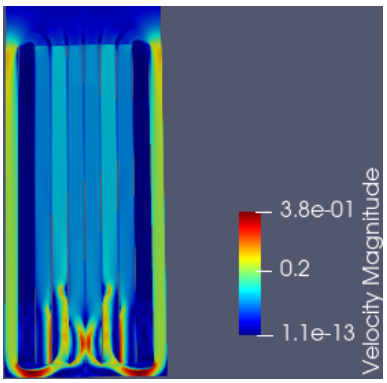

Figure 4.2: norm of the velocity field for $dt = 0.5ms$ and $t = 50s$

The speed profiles in the assemblies on figure 4.3 follow a rather interesting pattern. As explained before, the two free channels have a flow going downward (by conservation of mass, if the flow goes up in most channels and the water level of the pool stays the same, it is evident that the flow must go down somewhere) but the flow in the D1 and D8 channels actually first increases up to $t = 30$ seconds and then it decreases until reaching 0m/s at $t = 50$ seconds. the existence of this non-zero initial velocity field could have been deduced from the fact that the sinusoidal heat profiles in channels D1 and D8 are not perfectly centered, but are slightly shifted to the top. It seems like a similar trend is also happening in channels D2 and D7 since a maximum was reached in $t = 45$ seconds, but we will need longer simulations to confirm that.

As the flow of water going out of the channels increases over time, so must the flow going downward (by the mass conservation principle). At first, all the downward flow can evacuate via the two free channels, but as the speed increases, they are not sufficient anymore and therefore the flow going out of the two outermost assemblies stops completely.

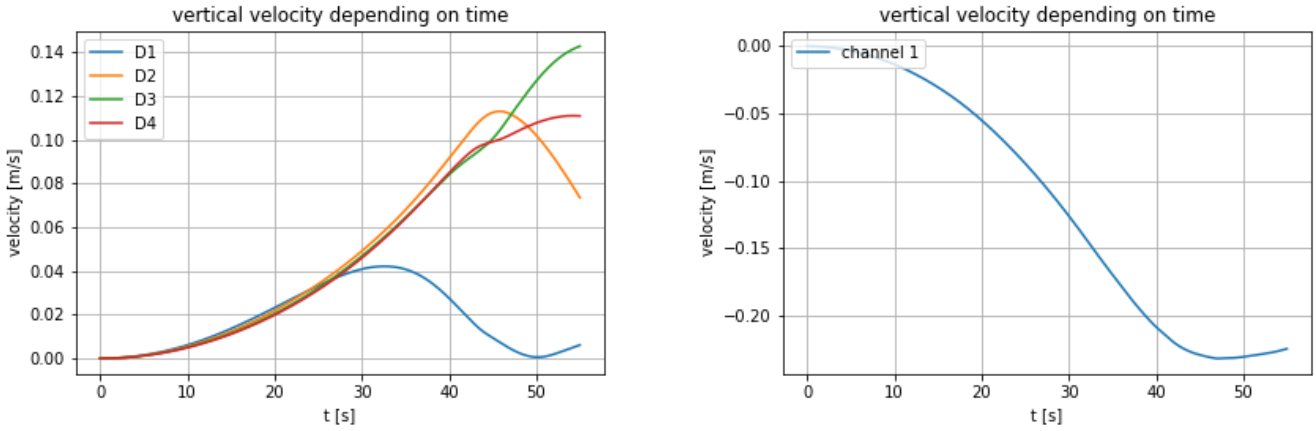

(a) (b)

Figure 4.3: vertical speed in the assemblies (a) and in the left free channel (b)

110 seconds simulation

In this section, two simulations with a time step of $dt = 0,5ms$ where conducted with a duration of 110s. The first simulation used the sinusoidal heating profile, and the second one used the uniform heating profile. Note that the reason why the small time step of 0,5ms was still used here is because the simulations were launched by waves of four or five at the same time. The next wave will use the 1ms time step instead as it was proven to be small enough in the precedent section.

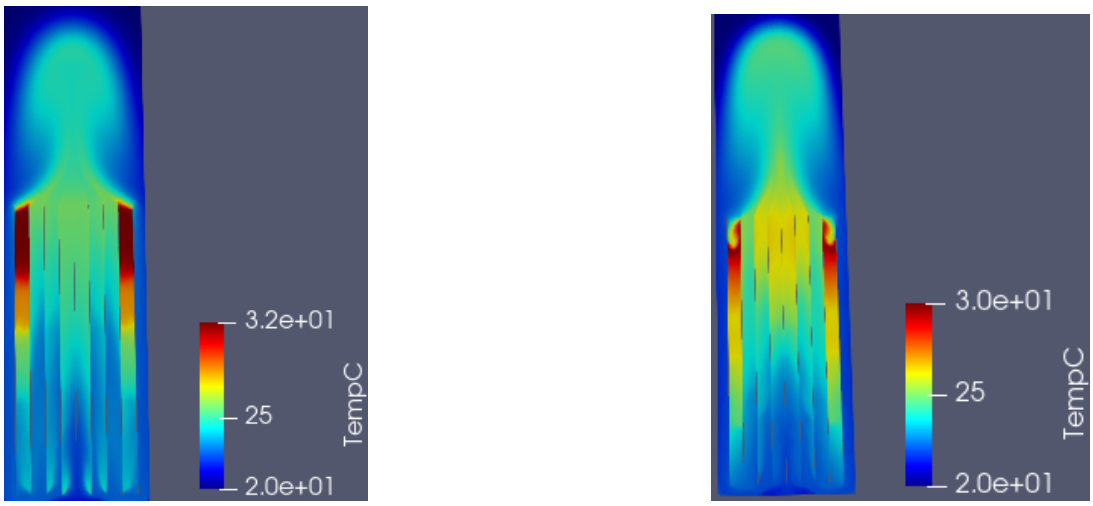

(a) (b)

Figure 4.4: temperature profiles for the uniform heating case (a) and the sinusoidal heating case(b)

In the two pictures on figure 4.4, the temperature field for the two heating cases are displayed. Both are very similar, but the maximum temperature is slightly higher in the uniform case, with a maximum value of 32 C° at the top, compared to 30 C°. There is a large plume in both case, which indicates the presence of two convective cells. The water from the center assemblies climbs in the pool, and push colder water down in the two free assemblies at the extremities of the pool. The hot water in D1 and D8 in both heating profiles is trapped inside by this reflux of colder water in a similar fashion to what was observed in the 50 seconds simulation.

The two color map of the velocity norm at $t = 110s$ are shown in picture 4.5. The pattern is almost identical to what was observed in simulations for $t = 50s$ (figure 4.2), with downward flows in the two spaces between the assemblies D1 and D8 and the two walls. The flow is nearly equal to 0 $[\frac{m}{s}]$ in D1 and D8, and is nearly uniform in the upper parts of the internal channels (D2, D3, D4,

D5, D6 and D7). The maximum velocity is reached just below the D1 and D8 channels, with local streams of water reaching up to 0.37 $[\frac{m}{s}]$ locally. The speed in the central assemblies is a bit higher in the sinusoidal case, with the D3 and D6 channels undergoing the strongest mass flow.

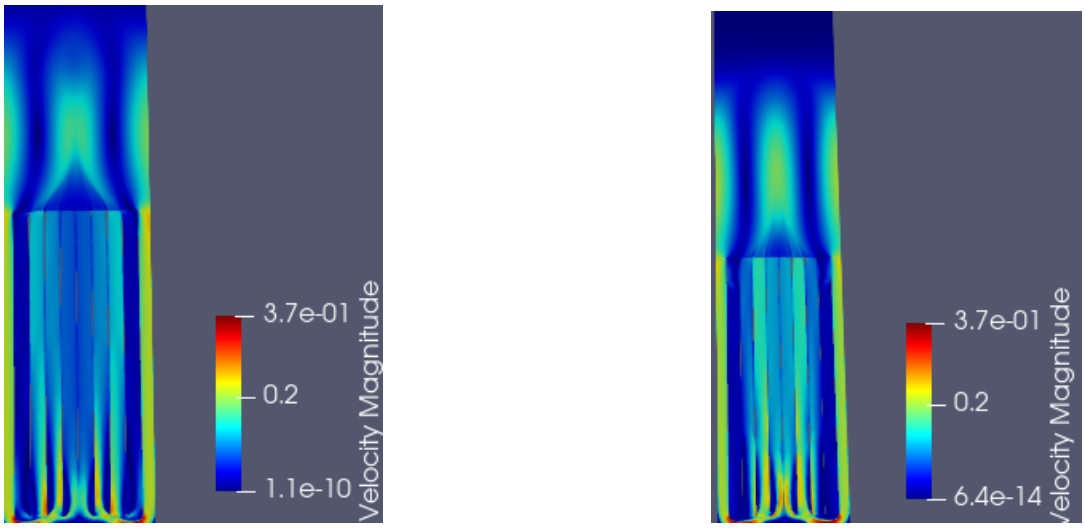

(a) (b)

Figure 4.5: velocity magnitude of the flow for the uniform heating (a) and the sinusoidal heating (b) at $t = 110s$

It is important to look at the streamlines of the flow in order to describe the convection cells with more details and to see their impact on the flow in the assemblies. As can be seen at the bottom of figure 4.6, the hot water exits the 6 most internal assemblies and enter a system of two symmetrical convection cells. The speed reaches a maximum roughly at the same Z coordinates than the centers of the convection cells. This maximum is mainly due to the Z component of the speed as the streamlines where the max speed is reached are nearly vertical. Note that in all the representations of the streamlines used in this master thesis, the color scale represent the norm of the speed.

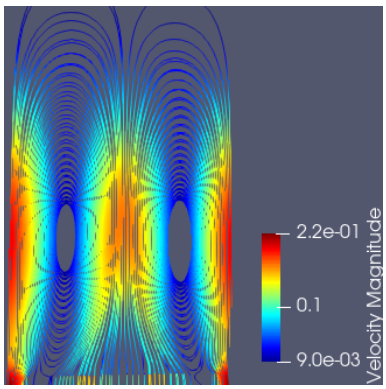

Figure 4.6: streamlines of the flow above the rack

The X component of the speed stays quite low even in the four areas where the streamlines are almost horizontal (below and above each cell centers on figure 4.6). This can be explained by the mass conservation principle. Let's look at the cell on the left: the flow that goes down near the left wall of the pool next to the center of the convective cell (where the velocity norm reaches its maximum value) can only pass through a small section with a width of 50 cm (distance between the wall and the center of the left convective cell), roughly one fourth of the total width of the pool, this section will be called section A.

Once the water has reached the lower part of the cell, it can either go further down in the left free channel, or it can turn on the right and re-enter the convection cell (let's call this area section

C). So the sum of the mass flow that goes in the left free channel and the mass flow that stays in the convection cell (region C) is equal to the mass flow that goes through section A. It means that the flow going through section C is much slower since its mass flow is lower than the mass flow in section A, and the section it has to cross is much wider (1,2m instead of 60 cm). This explains why there are two low velocity band in figure 4.5, note that this locally horizontal flow in section C will temporarily block the hot water in the assemblies D1 and D8 from exiting, which explains why the temperature is more important in these channels as the heat cannot be evacuated by natural convection.

The flow in the upper part of the pool (near the surface) doesn't exhibit any interesting feature at this stage, the two convective cells extend upward and the speed of the flow stays very low with a value of less than $0.01[\frac{m}{s}]$ as can be seen on picture 4.7. The symmetry of the flow is broken in both the uniform and the sinusoidal case.

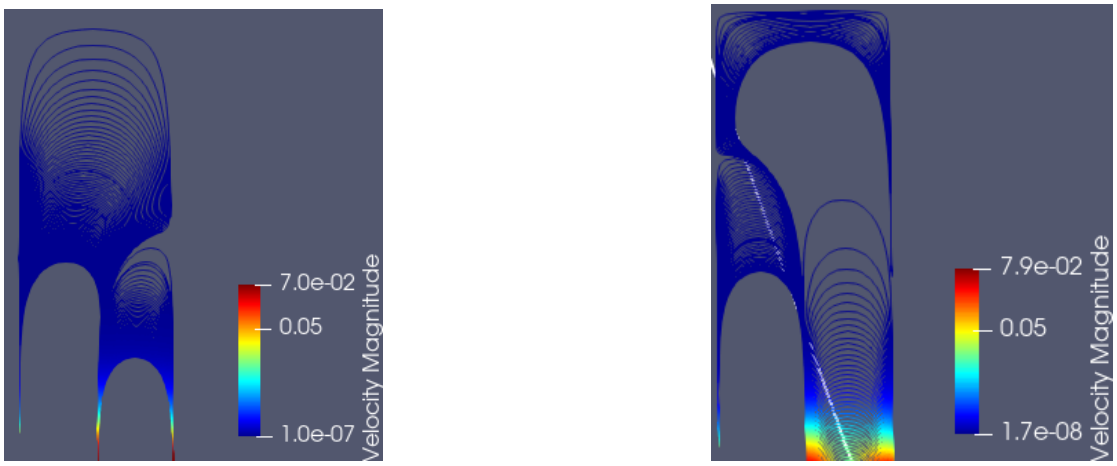

(a) (b)

Figure 4.7: streamlines of the upper part of the flow for the uniform (a) and the sinusoidal heating profile (b) at $t = 110s$

The curves of the vertical speed at the top of the different assemblies are displayed on figure 4.8a, and the vertical speed in the two free channels on figure 4.8b. As the configuration of the rack is symmetrical, only the curve of the 4 assemblies on the left are shown. As could be seen on the picture 4.5, the vertical speed in the D1 channel is nearly equal to zero for both $t = 50s$ and $t = 100s$, but it actually reaches a maximum in t = 85s with a speed of more than 10 $[\frac{cm}{s}]$, a first maximum is also reached in $t = 32s$. The onset of a local reflux can also be seen in $t = 100s$ in D1.

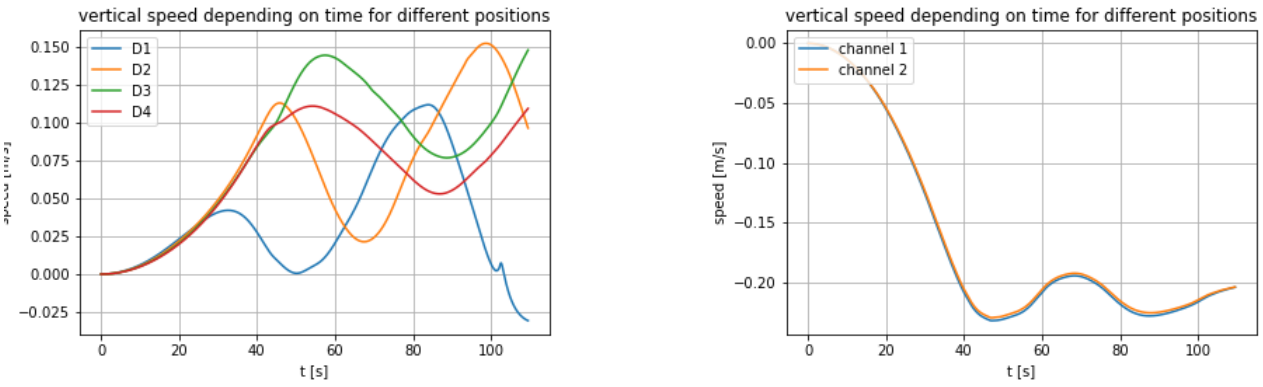

(a) (b)

Figure 4.8: graph of the vertical speed of the flow in four assemblies (on the left) and in the two spaces between the wall of the pool and the rack

At the beginning of the simulation, as the water starts to go up in the assemblies, all vertical speed profiles are almost identical (the speed curves are the same between $t = 0$ and $t = 30s$), but as the speed increases in all channels, the water coming out of the D2, D3 and D4 assemblies will create the convection cells, which will effectively prevent the water in D1 from escaping (as it was explained in the "50s simulation" section), which explain the local minima of the blue curve in $t = 50s$. After a while, the speed in D2, D3 and D4 will start to drop, which will allow the water in D1 to gain speed vertically as can be seen on the graph between $t = 50s$ and $t = 90s$. The reason why this drop in speed in the three assemblies occurs is because the hot water accumulated there has been evacuated and replaced by colder water from the top of the pool, which means that the buoyancy force pushing the water upward has decreased. Eventually, the water will heats up again and a new increase in speed will be observed in the three innermost assemblies (the beginning of a new cycle can be seen on the D2 curve at $t = 70s$).

The temperature at the top of the four assemblies and the left free channel for both heating profiles are shown on figure 4.9. The biggest difference lies in the shape of the curves for the 4 assemblies during the first 60 seconds. In the sinusoidal case, the temporal derivative of the temperature is first roughly constant during the 20 first seconds. At this point, the water hasn't move much and the increase in temperature is only due to the local heating by the nuclear waste.

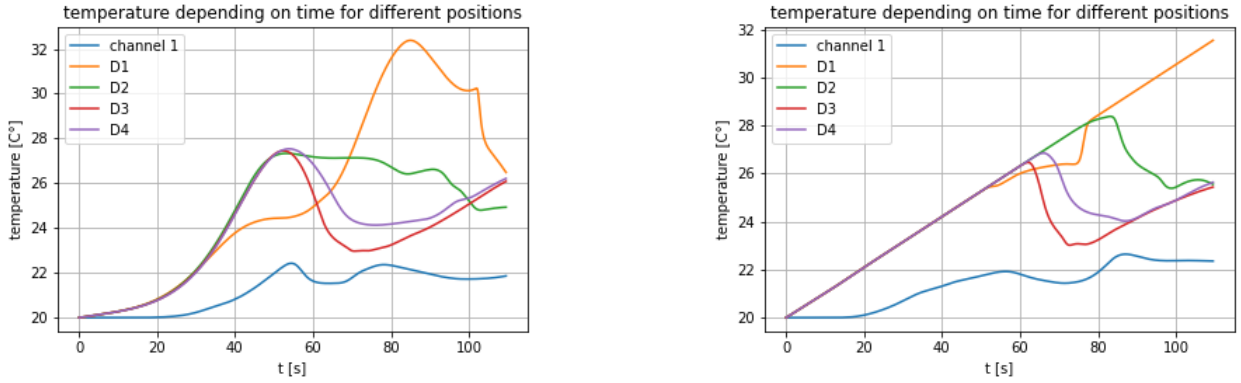

(a) (b)

Figure 4.9: graph of the temperature at the top of the four assemblies and a free channel for the sinusoidal heating (a) and the uniform heating (b)

After 20 seconds, the temperature starts to increase faster as hotter water coming from a region with a higher flux start to go up due to the higher buoyancy. After 50 seconds, the temperature suddenly drops at the sensors on top of D3 and D4 as the colder region originally located at the bottom of the channels passes in front of the sensor. Note that the maximum temperature is reached later in D1, more precisely in $t = 85s$. This "delayed" maximum is due to the low velocity in this channel for the reasons explained a bit earlier.

The temperature curves in the uniform case are much simpler. Even when the convection becomes significant, the temperature field is not impacted and stays linear as there is initially no temperature gradient in the channels. The sudden drop occurs when colder water that was not in the channel at the beginning passes in front of the sensor.

The first important lesson learned in this section is that the free channels and the space between the bottom of the pool and the bottom of the rack are not wide enough. Because of this, the assemblies initially empty into the pool one after the other and the flows exhibit an oscillating behavior.

4.2.2 Configuration 2 : rack with older nuclear wastes in the center

The second rack configuration studied here consists of 8 nuclear wastes like before, but this time, the power output of the four innermost assemblies has been divided by two: the power outputs are 35kW on the outermost assemblies and 17,5kW in the innermost ones. In the first configuration, it was discovered that the flow in the inner assemblies tended to block the flow in the outer assemblies. Here we are going to see if the same phenomenon takes place.

The time step chosen was $dt = 0.5ms$ (it was launched in parallel to the first simulations, so the time step was not adapted to the larger value of $dt = 1ms$) and the boundary conditions are the same as before. The simulation lasts 110 seconds and both sinusoidal and uniform heat release profiles were tested in order to compare them.

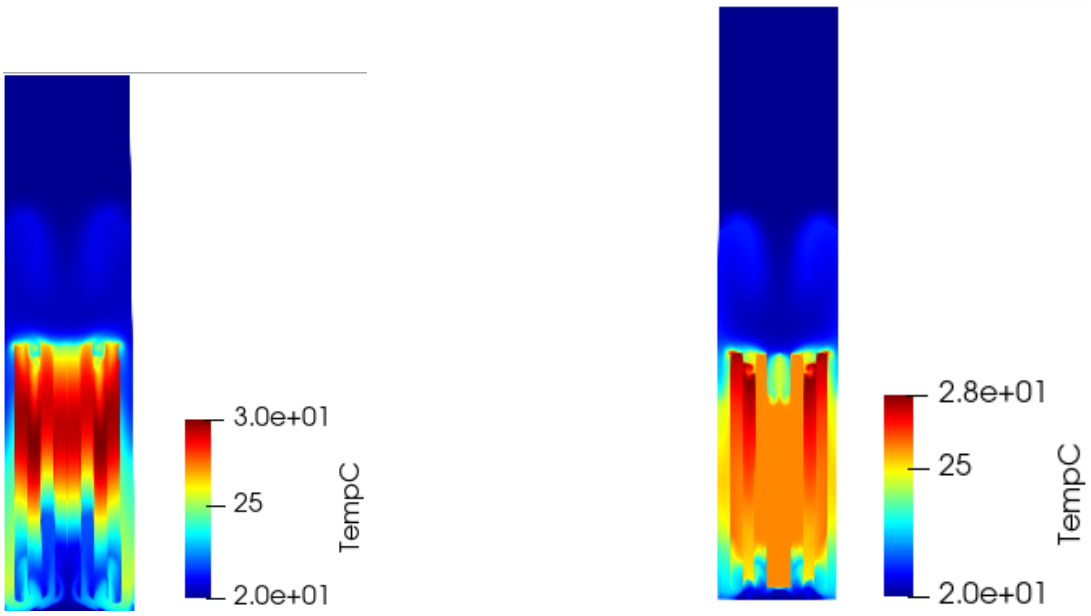

(a) (b)

Figure 4.10: temperature of the flow with a sinusoidal (a) and a uniform power distribution (b) at $t = 110s$

At first sight, one might be tempted to conclude when looking at 4.10 that the water in the assemblies almost didn't move. Indeed, as can be seen on figure 4.10a, The hot regions located at the top all have a sinusoidal shape similar to the one observed in D1 and D8 in figure 4.1a. Similarly, a uniform temperature region is also clearly visible in the four innermost assemblies on 4.10b. Convective cells can be observed above the rack in both case, but they are much fainter than in the first configuration studied in section 4.2.1. In fact, the outermost assemblies actually experimented a significant flow and the remnant of the hot regions that were evacuated from these assemblies can be observed in the two free channels.

In the case of the uniform heating profile (figure 4.10b), the four innermost assemblies seemed to have mainly conserved a uniform temperature field, indicating that the velocity field was rather low and uniform during the simulation, while the four outermost underwent some mixing, which caused the observed temperature gradient (the temperature is clearly higher at the top of the D1 and D2 channels than at the bottom). This can be explained by the fact that the buoyancy in the middle was lower due to a lower heating profile, which induced a lower natural convection. This hypothesis can be confirmed by looking at the streamlines in $t = 80s$ (see figure 4.11a), where we see that all the streamlines in the innermost assemblies are parallel and have the same very low velocity.

As said earlier, some hot water can be observed going downward in the two free channels. The

maximum temperature of this hot reflux reaches a value up to 25°C in the case of the uniform heating profile. It means that contrary to the first configuration, the hot water is directly brought in the two empty channels without entering the convection cells on top, which explains why those ones are almost invisible on the color map of the temperature field displayed in figure 4.10. This effect is also clearly visible in the two free channels of the sinusoidal heat profile case. A quick look at the two streamline profiles on figure 4.11 will confirm that the flow going out of the channels nearly doesn't enter the two convection cells. What is interesting there is that contrary to the first case, the convection cells on the right rotate counterclockwise, which tends to push some water inside the two innermost channels in the uniform distribution case, causing the two vortices at the top of D4 and D5 visible on figure 4.11b. In a similar way to what was observed in section 4.2.1, the convection cells are blocking the water in some channels, but here only the innermost assemblies are concerned as the directions of rotation of the cells are reversed compared to section 4.2.1.

The maximum speed is reached at the top of the two empty channels near the walls and at the bottom of the D1 and D8 channels. A few vortices are also present down there, they are induced by the high velocity stream of water going up in the two channels.

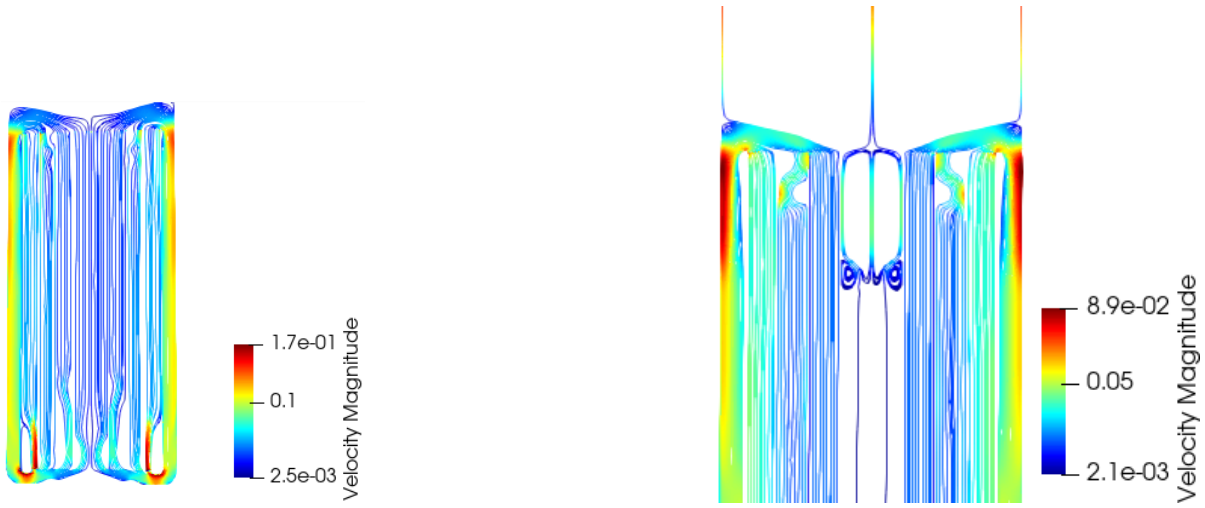

(a) (b)

Figure 4.11: streamline of the flow in the channels with a sinusoidal heating profile (a) and a uniform heating profile (b) at $t = 110s$

Similarly to what was observed in section 4.2.1, the vertical speed in the channels varies greatly over time as can be seen on picture 4.12a. As it was discussed before, the speed in the D4 channel is nearly equal to zero during all the simulation, at least in the uniform heating profile case. Consequently, the temperature profile increases linearly as the water stays in place. In the D1 and D2 channels, there is first a fast increase of the vertical speed, which will limit the temperature increase in the first place as hot water is quickly replaced by cold water, then the current will slow down significantly to almost reach $0[\frac{m}{s}]$ in $t = 90s$. As an effect, the temperature will rise again as the water is immobilized. The hot water seems to reach the middle of the two free channels in $t = 40s$.

The flow regime here seems to work by pulse : The mass flow going through the two free channels first increases until reaching a speed of $0.15[\frac{m}{s}]$, before decreasing at the same pace than the flow in D1 and D2. An onset of a second pulse can be seen after $t = 90s$, but it must be confirmed with a longer simulation. Here there is a perfect illustration of mass flow conservation : all the water that goes out of the D1 and D2 channels immediately flows back down in the left empty channel. The cross section of the empty channel is half the total cross section of D1 and D2, but the porosity in these channels are roughly equal to 0.5, which means that the speed in D1 and D2 is nearly the same as the speed in the empty channel.

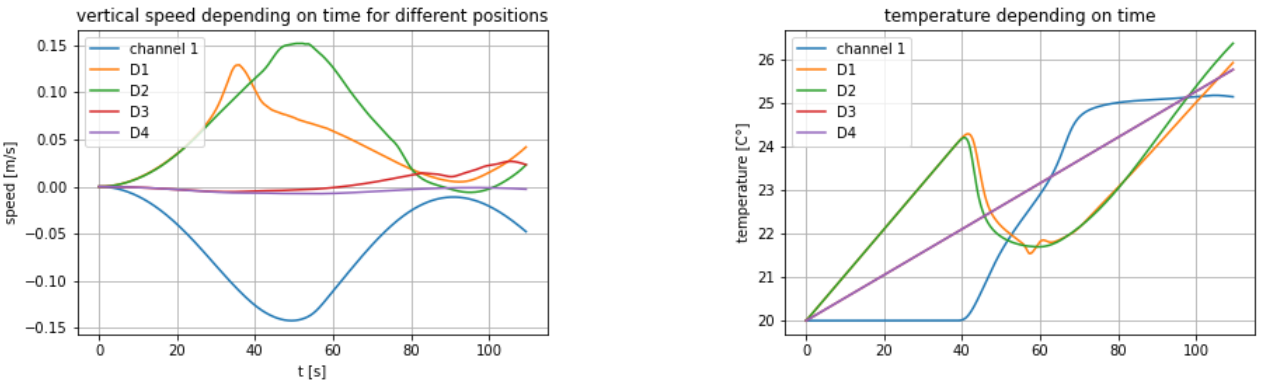

(a) (b)

Figure 4.12: graphs of the vertical speed and the temperature in the middle of the channels over time for the uniform heating profile, only half of the channels are shown as the flow is almost symmetrical

To understand the reason why the vertical velocity in D2 drops in $t = 90s$, it is necessary to understand why the vertical velocity increased in the assembly in the first place. At the beginning, the free channels are full of cold dense water while the density of the water in the assemblies decreases. As a result, natural convection will occur and a big "loop" will appear as the hot water starts to go up and the cold water starts to go down. However, as hot water starts to enter directly in the free channel, this density difference between the channels disappears and the driving force of the "loop" fade away, causing the flow to stop. Then, as the water temperature continues to rise in the channels, the density difference starts to increase again and the cycle continues until the water in the free channels becomes too hot once again. The velocity and the temperature profiles at $t = 80s$ are displayed on figure 4.13, the flux of hot water in the empty channels can clearly be seen on picture 4.13a. It is interesting to note that the flow is actually faster near the wall at the level of the two large convection cells than in the free channels in $t = 80s$, but most of the hot water bypass the cells to go directly to the bottom of the pool.

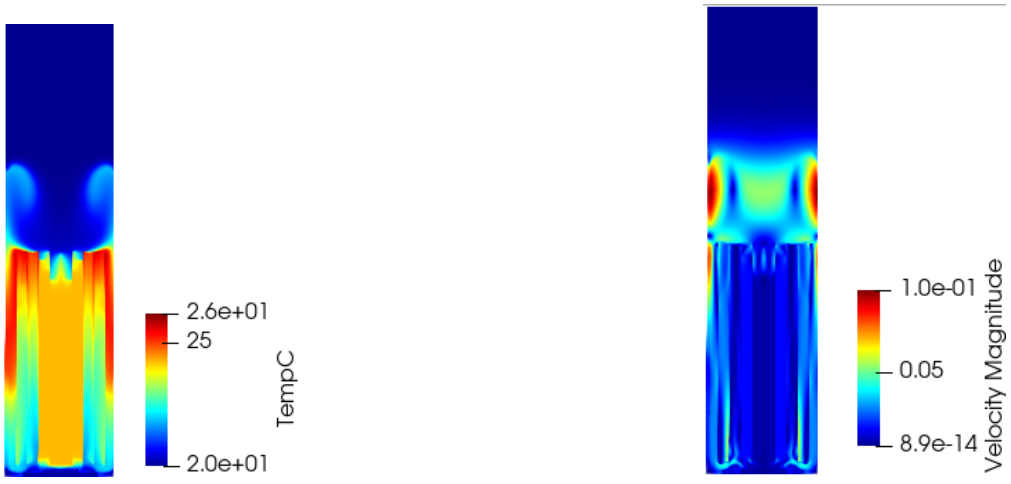

(a) (b)

Figure 4.13: temperature and velocity profile of the uniform heating profile simulation at $t = 80s$

This configuration of the nuclear wastes doesn't seem to be optimal, at least based on the 2 first minutes of simulations, because half of the assemblies couldn't evacuate their accumulated heat, compared to two assemblies in section 4.2.1. This is due to the fact that the water in the outermost assemblies have a greater buoyancy than the water in the four innermost channels. the hot water in D1, D2, D3 and D4 will thus climb faster in a first time, which will induce two convective cells with a downward flow in the middle of the pool. This flow will then block the water in the innermost

assemblies. Furthermore, hot water flows back directly into the free channels without mixing with the cooler region above the rack, which means it can then flow back into the assemblies and cause high-temperature hot spots.

4.2.3 Configuration 3 : rack with an asymmetrical distribution

In the two first cases, it was seen that at some point in the simulation, some channels containing old or fresh nuclear waste couldn't evacuate their heat properly due to the flow generated by other assemblies. In order to try to address this issue, four nuclear waste assemblies with a power of 35 kW were put on the right side side of the pool, with four nuclear waste assemblies with a power of 17.5kW kW filling the four channels on the left side. The simulation used a time step $dt = 0.5ms$ and the two heating profiles defined at the beginning were used (both sinusoidal and uniform).

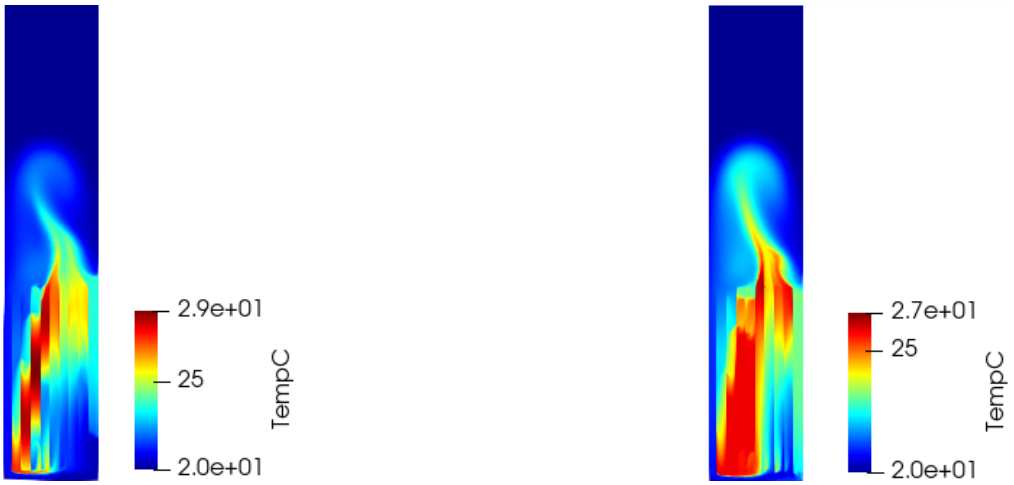

Figure 4.14: temperature field of the uniform heating profile (b) and the sinusoidal heating profile (a) at $t = 110s$

The temperature field for both heating profiles are shown on picture 4.14. It seems that the hot water contained in the right assemblies was evacuated by convection and mixed with the colder water present above, the hot plume is clearly visible in both simulations. The convection cells present above the channels follow a more complicated pattern than the one observed in configuration 1 and 2, it is due to the asymmetrical heating profile of the pool and the fact that the convection current is stronger on the right than on the left.

The four assemblies with less powerful nuclear waste couldn't completely evacuate the accumulated heat released by the decay of the radioactive isotopes. The flow of water in the two channels on the left is directed toward the ground, which explains why they contain cold water at the top and very hot water at the bottom. It is even more clear on picture 4.14a, as the sinusoidal temperature profiles are still visible but are shifted downwards (in D1 and D2). The maximum temperatures in the uniform and the sinusoidal cases reach respectively a value of 26 and 29 C°.

The streamlines are shown on figure 4.15. Two large convection cells are visible, the smallest one located on the left is connected to the streamlines entering the channels with the older nuclear waste, and the larger one is not directly connected to the assemblies. The water that exits the D6, D7 and D8 channels enters the small cells, climbs up to 3 meters (at least in this time step) and then goes down in the left free channel, with a maximum velocity of up to $0.22[\frac{m}{s}]$. The water that exit the D5 channel also enters the convection cell, but will then enter in D1 and D2, which will induce a local reflux there.

(a) (b)

Figure 4.15: streamlines just above the channels of the uniform heating profile (b) and the sinusoidal heating profile (a) at $t = 110s$

In this configuration of the assemblies, the temperature and velocity profile are no longer symmetric, the 8 vertical velocities measured at the middle of the assemblies are shown on picture 4.16. The vertical velocities in the four channels on the left are almost equal to zero for the 60 first seconds of the simulations, which suggest that the water was blocked during this period of time, before it starts to increase in the negative value. This effect is very strong on the D1 channel and at the end of the simulation, almost all the hot water contained in it was evacuated from the bottom. The free channel on the left of D1 also sees its velocity increase in the negative value, but it reaches a plateau after roughly 80 seconds. It is very likely that its value will start to decrease after that as the flow in this channel is induced by the hot water contained in the four channel on the right. This hypothesis must be confirmed by a longer simulation though.

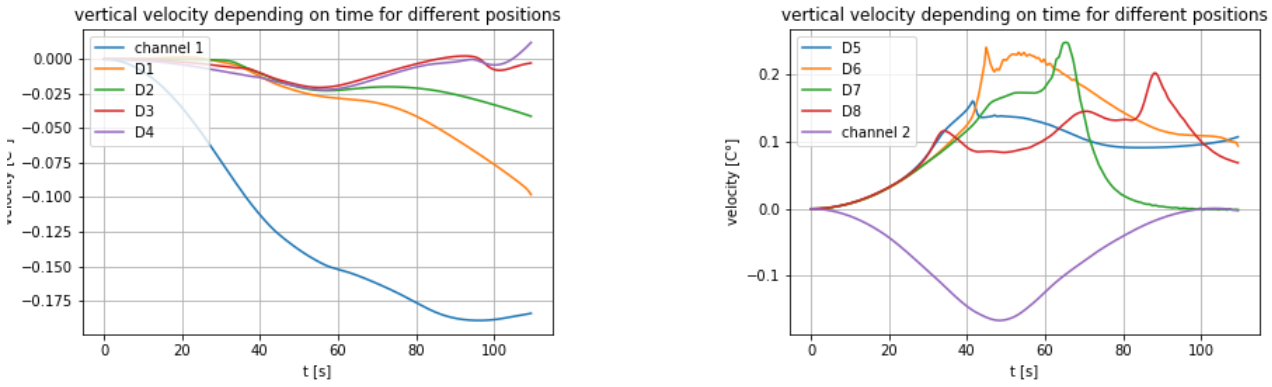

(a) (b)

Figure 4.16: Graphs of the vertical velocity for the uniform heat profile case at $t = 110s$

In the right part of the rack, the four flows are directed upward as the water circulating in these assemblies has a higher buoyancy. After an initial increase, the velocity in D7 drops to zero as the hot water is being replaced by colder water. The velocity in the other channels also decrease, but they didn't reached zero at the time of the end of the simulation. What is also interesting is that here, the free channel on the right has a very smooth Gaussian shaped velocity profile which reaches a maximum value in $t = 50s$. The relatively high temperature region observed in this free channel in picture 4.14b and 4.14a is a remnant of the flow that entered by the top in the middle of the simulation. Before $t = 90s$, the flow going out of the 4 assemblies on the right split itself into two parts, one was headed toward the left free channel and D1, and the other entered directly the right free channel. We know that because the temperature at the top the right free channel (visible on figure 4.17b) starts to increase after only 20 seconds of simulation. After a while, the accumulation of hot water caused a local decrease of the water density, which induced a drop in the velocity. The flow that used to go

on the right free channel headed toward the left, which explains why the left free channel still has a strong current after $t = 110s$.

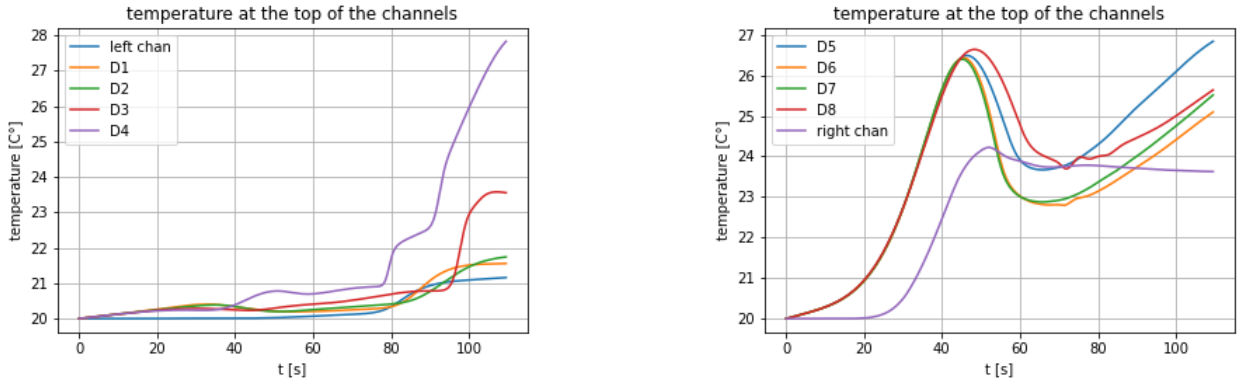

(a) (b)

Figure 4.17: Graphs of the temperature at the top of the assemblies for the sinusoidal heat profile case at $t = 110s$

4.2.4 Configuration 4 : rack with an alternate distribution of assembly

The fourth case that will be studied in this section consists of a rack with four assemblies releasing a power of 35kW in the D2, D4, D6 and D8 channels, while the four other channels contain less powerful 17.7kW assemblies. The time step here is $dt = 1ms$, and the simulations was run on both sinusoidal and uniform heating profile for a period of 220s in total. This longer integration time is necessary to study the flow with more details. It will allow us to see if the velocity or the temperature field exhibit some kind of periodic behavior on the long run.

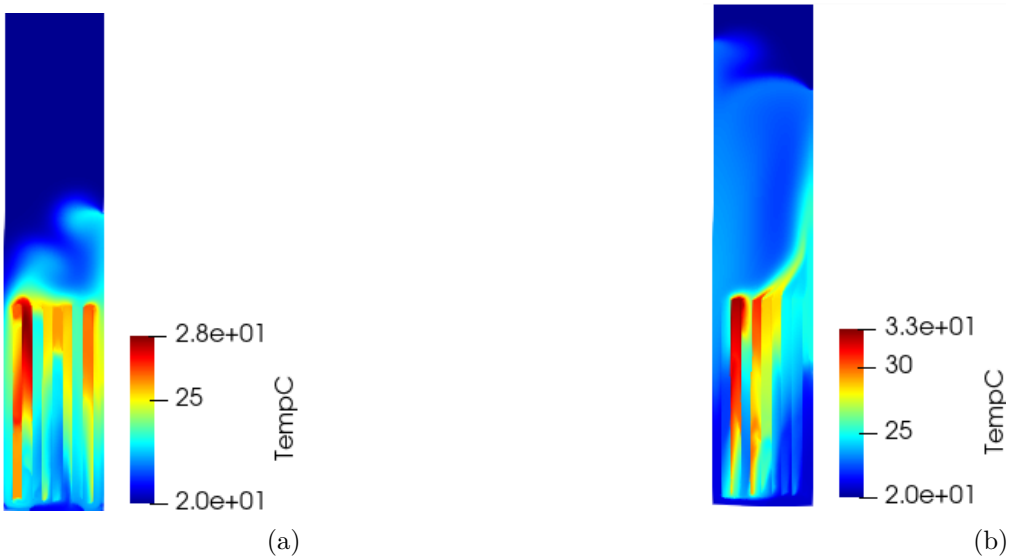

(a) (b)

Figure 4.18: temperature profile of the uniform heat release profile at $t = 110s$ (a) and $t = 220s$ (b)

The pictures on figure 4.18 show the temperature profiles at two different moments of the simulation. The hot water produced in the channels moved upward and mixed with the surrounding cooler water in all but one assembly, the D2 channel, where the temperature reach a maximum of 28 C° in $t = 110s$, and 33 C° in $t = 220s$. The temperature in the two free channels first climbs to 23-24C° in $t = 110s$, before cooling down to 21C° in $t = 220s$. This is due to the fact that the hot water exiting the channels in the middle is first evacuated directly in the free channels in $t = 110s$, then the pattern of the flow changes and the hot water starts to move upward directly. The hot water exiting D2 is directly re-entering either the left free channel in $t = 110s$, or D3 in $t = 220s$, which indicates the presence of a

reflux. The water in the bottom part of the D1 channel didn't move a lot as the uniform temperature field is still clearly visible, it indicates that the velocity field there was quite low at least during the first 110s of the simulation .

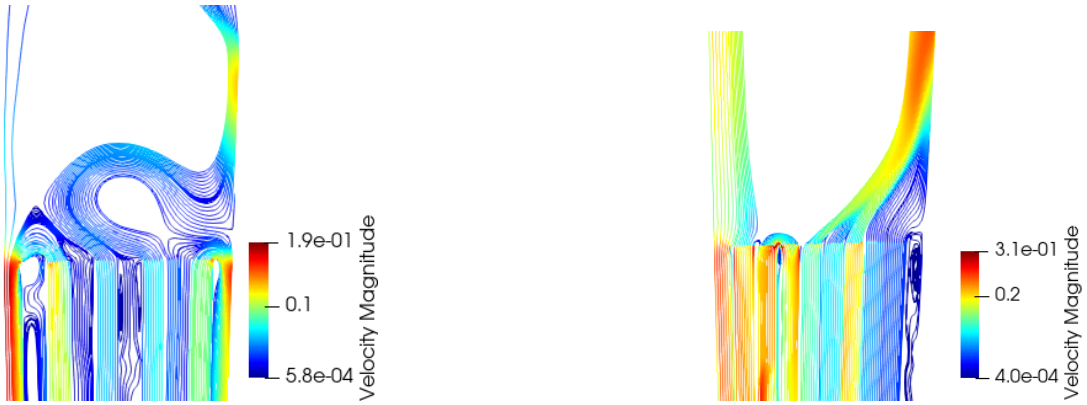

(a) (b)

Figure 4.19: streamlines of the uniform heat release profile at $t = 110s$ (a) and $t = 220s$ (b)

The streamlines of the flows are shown on picture 4.19. In both snapshots, there is a big convection cell as large as the pool above the assemblies that rotates counterclockwise. There is also a smaller cell just below in $t = 110s$. The higher upward flow on the right of the pool in picture 4.19b will induce a higher downstream flow on the other side of the pool by mass conservation, which will induce a reflux in the D1 channel as can be seen on the left of picture 4.19b. It also means that the water exiting the D2 channel is now forced to be evacuated in the D3 channel instead of going into the left free channel, which will also induce a reflux there.

The streamlines of the two large cells are shown on figure 4.20

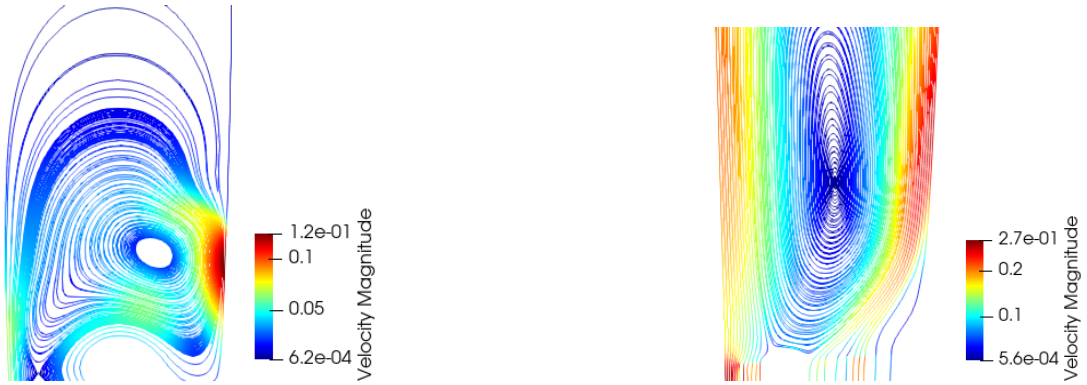

Figure 4.20: streamlines of the two large cells of the uniform heat release profile at $t = 110s$ (on the left) and $t = 220s$ (on the right)

The graphs of the vertical velocity at the top of the channels are shown on picture 4.21 for the uniform case. As in the previous sections, the curves of the vertical velocities in the assemblies with the most powerful waste are equal in the channels with a 35 kW nuclear waste between $t = 0s$ and $t = 30s$, before they start to diverge due to the impact they have on each other. The flow in the left free channel (which is always directed downward) first increases due to the incoming flow from channel D2, then it reaches a plateau at $v = -0,15[\frac{m}{s^2}]$ in $t = 50s$, before increasing again due to the flow coming from D4, D5 and D6.

The flows in D1 and D3 are relatively weak until $t = 180s$ because the thermal output of the assemblies they contain is lower than the others, then a massive reflux begins in both due to the flow exiting D2 for the D3 channel, and the flow exiting D4, D5 and D6 for the D1 channel. Note that the flow in D2 undergoes a small reflux between $t = 160s$ and $t = 190s$. It happens when the

outgoing flow switches from entering D1 to entering D3. The reflux in D2 happens because the temperature is not high enough at this moment in time to counterbalance the downward flow coming from the channels on the right of the domain (in other words, the density is not low enough in D2 at this time).

The velocity profiles in the channel located in the right part of the rack have the same behavior than the one on the left during the 40 first seconds, with the flows in D6 and D8 (the channels containing the most powerful wastes) increasing steadily at least in the 50 first seconds. The flow in D5 is almost equal to zero during most of the simulations, which explains why it is the channel with a 17.5kW power ouput that has the highest temperature at the top of it as the hot water wasn't carried away. In the last part of the simulation, the three channels on the right (D6, D7 and D8) seem to empty themselves of their hot water one after the other (the peaks on the graph has a slight offset), which feeds the vertical flow that enters the left empty channel after a loop around the large convective cell. It is not hard to predict that once the hot water in the D4 channels has been replaced by colder one, this flow will greatly diminish at least until the water starts to heat up again.

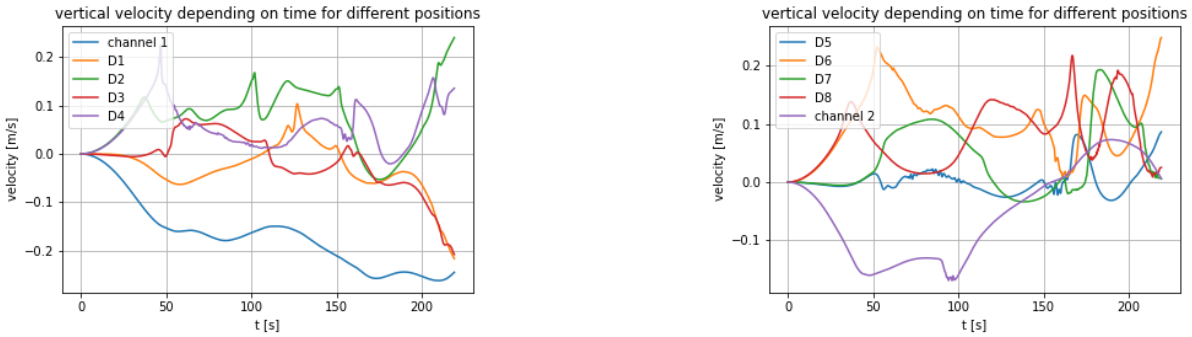

(a) (b)

Figure 4.21: graph of the vertical velocity in the middle of the channels

The temperatures at the top of each channels are shown on picture 4.22. It was decided to show the temperature profile on the top of the rack instead of in the middle, because that's where the maximum value of 32 C° is reached. It is interesting to see the correlation between the curves on the graph 4.21a and 4.22a. The stop of the flow that can be seen on the vertical speed curves at $t = 180s$ on 4.21a is matched with a drop of temperature at nearly the same time on figure 4.22a, followed by a sharp increase in the temperature when the velocity increases again. What is happening here is that the still water sees an increase of its temperature due to the heat source, which induce an increase of the water buoyancy so that the flow starts to accelerate upward after a while. At this time, the hot water accumulated in the middle of the channels passes in front of the sensor, which causes the sharp increase of T° in the four channels on the left.

The sensors on the right part of the rack (graph on figure 4.22b) shows that the temperature profiles in these channels vary less and are closer to each other. The five curves first increase during the 100s first seconds, then they stabilize at around 26 C°. The temperatures are not constant, but they don't vary as much as on the left. In addition to that, neither the D6 nor the D8 channels see a reflux of their flow as strong as the one seen in D2 (in $t = 180s$), which means that the heat couldn't accumulate as much, which lead to a lower peak temperature, with a maximum actually reached in D5 (which is a 17,5kW assembly) with a value of 28,5C°. To answer the question asked at the beginning of this section, it seems like there is no periodic pattern happening between 0s and 220s.

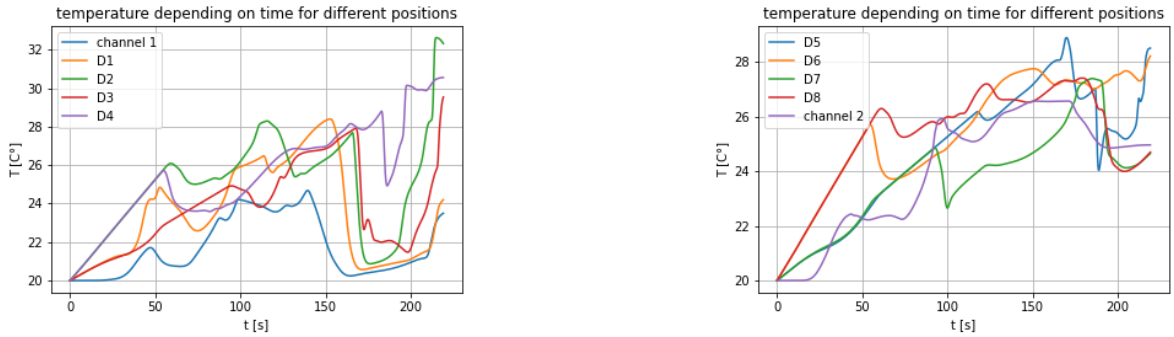

(a) (b)

Figure 4.22: graph of the temperature profiles on the top of the channels

In the following paragraphs, the temperature and the velocity profiles for the sinusoidal heating case will be studied and compared with the uniform one described previously. Here on picture 4.23, the temperature profile at $t = 110s$ and $t = 220s$ can be seen.

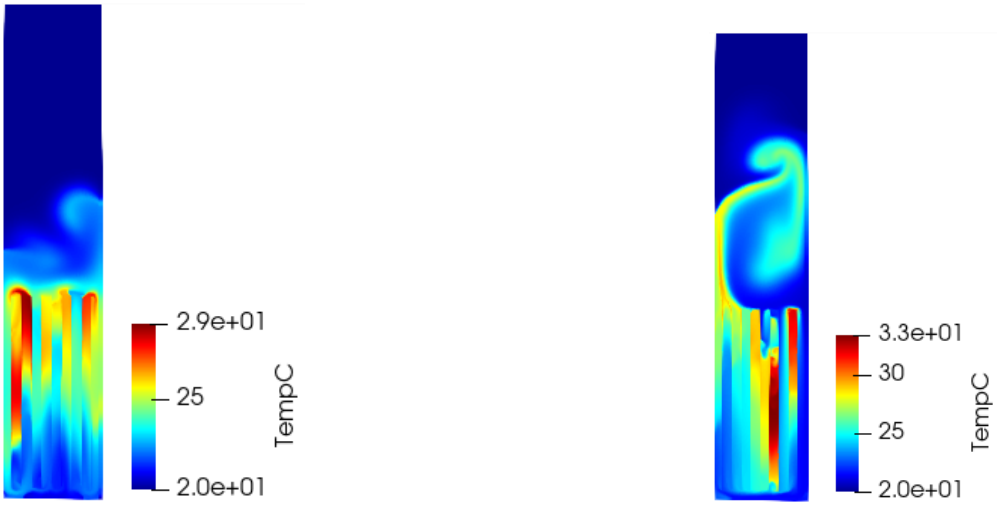

(a) (b)

Figure 4.23: temperature profile of the sinusoidal heat release profile at $t = 110s$ (a) and $t = 220s$ (b)

The temperature profile of both the uniform and the sinusoidal cases at $t = 110s$ share the same general features. Indeed, in both cases the D2 assembly has the highest temperature, with a maximum reached at the top at 29 C° (28 C° in the uniform one), the vertical velocity component is also very low in the D1 channel in both case, with a plume going out of D2 to enter the left free channel directly. Even the temperature profile in the region above the rack are similar in shape with a plume on the upper right. However, the similarity between the two stop shortly afterwards as the two temperature profile are completely different in $t = 220s$. There is also a large plume like in the uniform case, but this time it is located on the left of the rack, above the D1, D2, D3 and D4 channels. The maximum temperature is reached in the middle of the D6 assembly (one of the channels with a power of 35kW) because of a local reflux. This must be confirmed by the analysis of the streamlines.

The streamlines at $t = 110s$ on figure 4.24 are very similar to the uniform case, with the presence of a small convective cell that prevents most of the water from entering the larger one located above. The picture on the right however seems to depict a very different story than in the first simulation. Indeed, in this case the large convective cell rotate clockwise, and it is not as stretched upward as previously. The fact that the velocity field reaches a local on top of it (nearly $0.44\frac{m}{s}$) suggests the presence of an even larger convection cell that stretches to the surface of the pool.

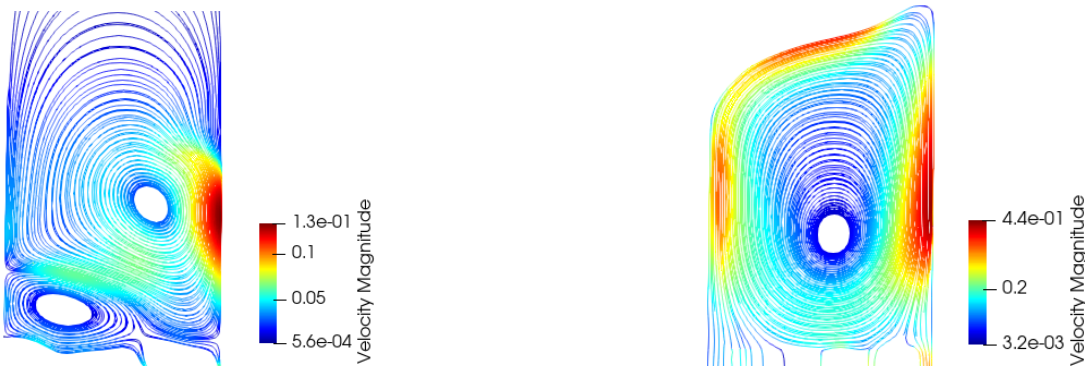

Figure 4.24: streamlines of the two large cells of the sinusoidal heat release profile at $t = 110s$ (on the left) and $t = 220s$ (on the right)

The apparition of the plume on the left side of the pool is related to the increase of the vertical velocity in the left free channel, and the 4 assemblies next to it. It can clearly be seen on the graph of figure 4.25a that the vertical velocities in D1 and the free channels undergo a reversal of direction at around $t = 190s$, which is the moment where the current becomes really strong. Similarly, the effect of this big convection cell is visible on the curve of the right free channel (channel 2) and D7, where a very strong reflux is observed with speed up to $-0.3\frac{m}{s}$. The divergence between the sinusoidal and the uniform case seems to happens around $t = 120s$; at this moment, the velocity of the flow in the free channel on the left (channel 1) starts to increase towards more positive values whereas it increases in the negative values in the uniform case. Similarly, the right free channel and D7 take the role of the left free channel and D1 on the right part of the rack, with very negative value for the vertical speed and a strong reflux.

When looking at the early phase of the simulations, it is interesting to spot the fact that the flows in both D2 and D3 channels oscillate in phase opposition. The D2 channels starts by emptying itself as it contains the hottest water, then once it is done, the water in the D3 channels can exit. In this early phase, the water coming from both goes directly in the left free channel like in the early phase of the uniform heating profile simulation.

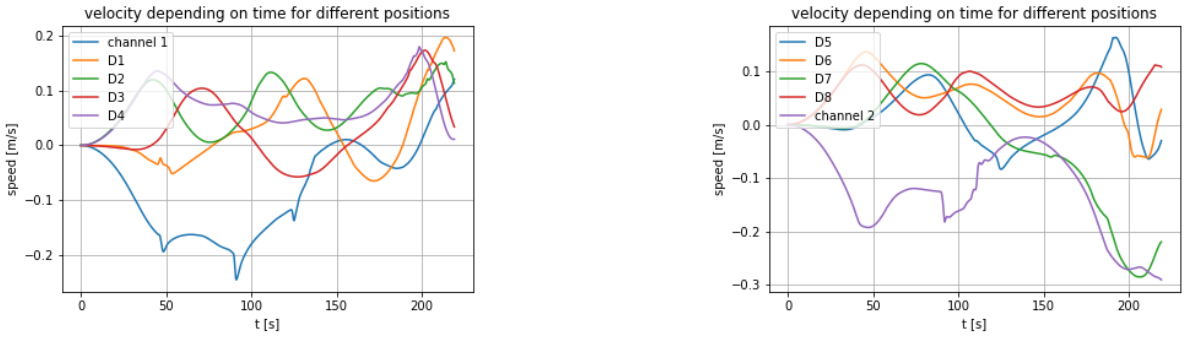

(a) (b)

Figure 4.25: graph of the vertical velocity profiles at the top of the channels

Similarly to what was observed in the uniform case, the side of the rack undergoing a reflux in the last stage of the simulation experiments the highest temperature (here 32 C° in the D8 assembly on graph 4.26b). The temperature curves in the left part of the rack are close to each other like the one observed on the right of the uniform case in 4.22b.

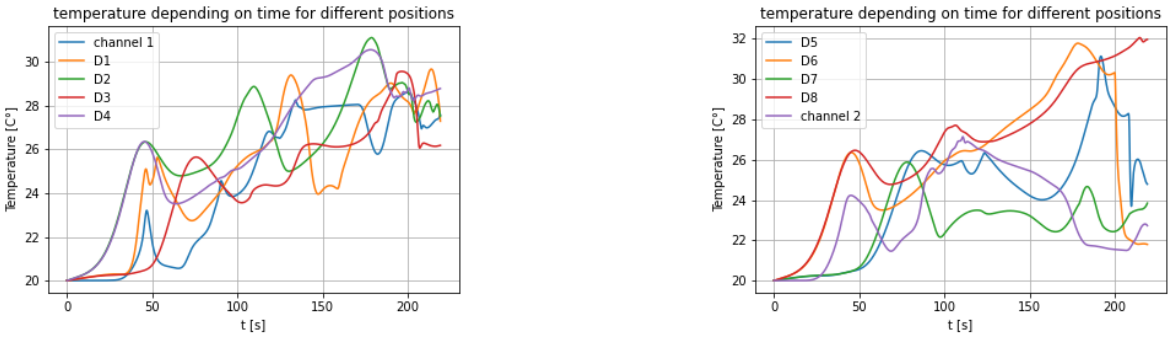

(a) (b)

Figure 4.26: graph of the temperature profiles on the top of the channels for the sinusoidal heat release profile

In both cases (sinusoidal and uniform), a few general lessons can be retained :

- In both cases, there is first a transient phase where the water exit the assemblies to enter directly in the free channels, followed by the formation of a plume on one of the sides, which will drive a large unique convection cell
- The hottest spot generally happens on the side of the rack opposite to where the plume appears, and it can be anywhere in one of the two most powerful assemblies, as the flow there undergoes an alternate of climbing phase and reflux phase.

4.2.5 Configuration 5 : inverted centered distribution

It was seen in section 4.2.2 that in a centered distribution with the low power assemblies in the middle, most of the hot water would stay blocked in the inner channels due to the presence of two large convection cells. Here, a similar case will be investigated, but this time with the low power assemblies on the outside. So the assemblies D1, D2, D7 and D8 will receive nuclear waste with a power output of 17.5kW, and the others will receive 35kW nuclear wastes.

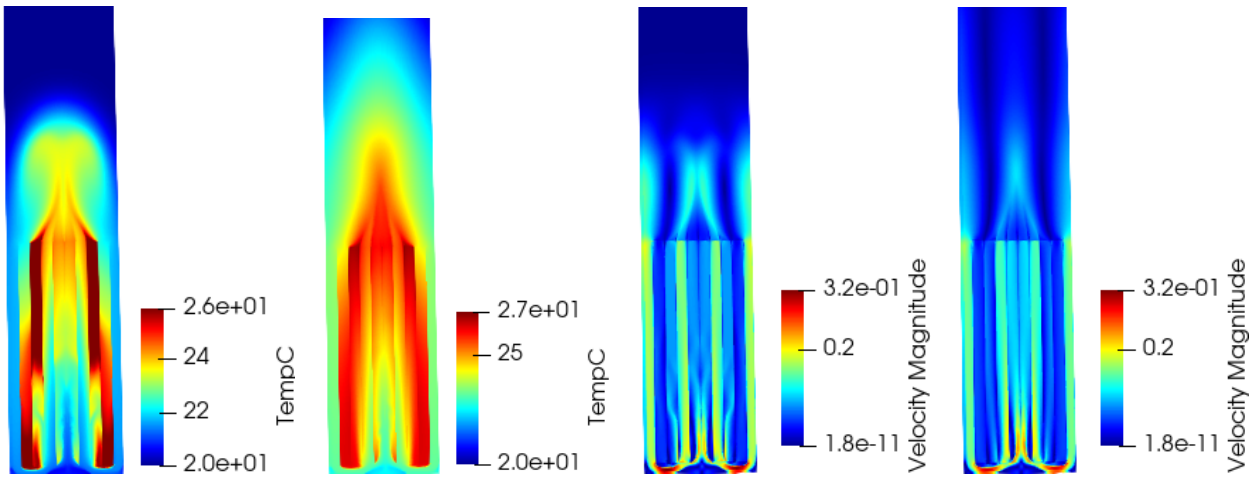

(a) (b) (c) (d)

Figure 4.27: temperature and velocity profiles of the uniform heat release case at $t = 110s$ (a, c) and $t = 220s$(b, d)

The temperature and velocity profile are coherent with what could be expected using intuition. Indeed, As the assemblies in the middle contains more powerful assemblies, one would expect the water there to heat faster and climb at a higher rate than at the periphery, which then would produce a massive central plume. And it is exactly what is observed in practice. Because of that

central climbing mass flow, the water in the 2 outermost assemblies (D1 and D8) is either blocked in the channel, or undergoes a reflux in a similar manner to what was observed in section 4.2.1. Basically, it means that the hot-spots are located at the bottom of D1 and D8, and at the top of D2 and D7.

Because of the local reflux, the hot water in D1 and D8 exit by the bottom, and enters the bottom of the D2 and D7 channels. This water can't be evacuated via the free channels on the other side as the current there goes in the opposite direction (it actually brings down the cold water that has been pushed back by the hot plume). The area with the highest velocity is actually located just below these two outermost channels, with a maximum water speed of 0,32 $[\frac{m}{s}]$. Contrary to configuration four where it was seen that the velocity field changes its shape dramatically after a while, here the pattern doesn't evolve much over time, the plume stretches a bit upward, but there is no inversion of the direction of the flow in any channel. Even the maximum temperature stays nearly the same with a slight increase from 26C° to 27C°.

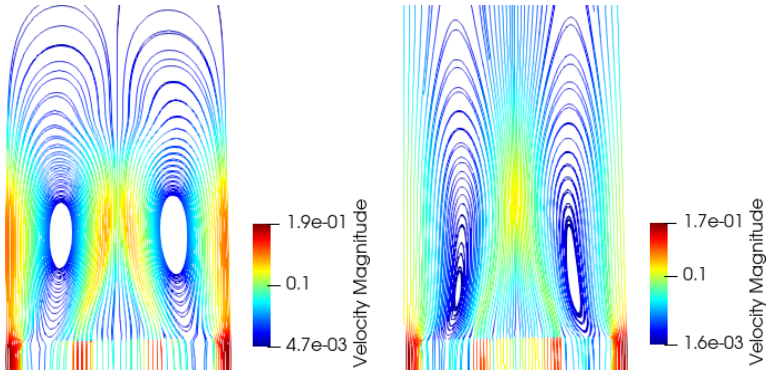

(a) (b)

Figure 4.28: streamlines at $t = 110s$ (a) and $t = 220s$ (b) just above the rack

The streamlines above the rack shown on figure 4.28 don't change shape either. There is just a lower peak velocity at the entry of the two free channels, where the water flows downwards, and it is probably due to the fact that as the hot water has been evacuated from the central channels, the speed at the exit of those diminishes, which in turn induce this lower velocity.

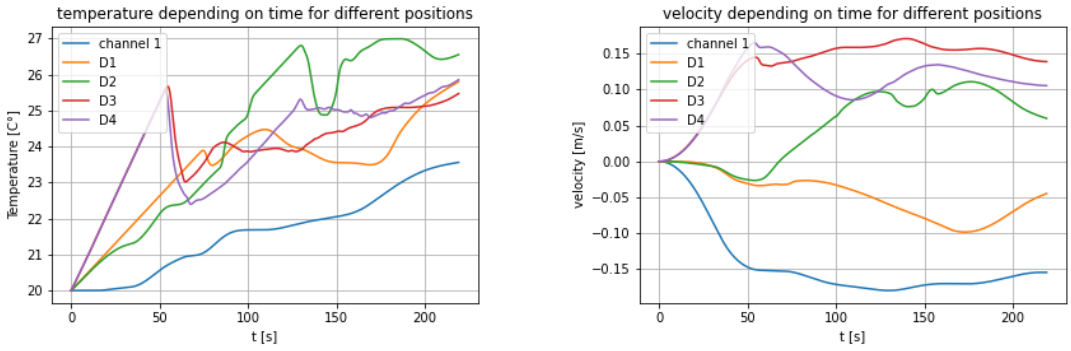

(a) (b)

Figure 4.29: graph of the temperature (a) and the velocity (b) in the channels for the uniform heating case

As the domain is symmetric, the graphs for the temperature and the vertical velocity on figure 4.29 only show the curves for the channels on the left. All the values where sampled on top of the channels, except for the temperature in D1, where the values are taken in the middle so that the temperature near the lower hot-spot is visible on the graph. The velocity curves don't present a lot of surprise and are rather constant in time after an initial acceleration. It shows once again that once the two convection cells on top are established, the pattern of the flow doesn't change much. The temperature

increase is also quite smoother than in the four other configurations. A big drop of temperature on top of D3 and D4 can be observed in $t = 50s$ on figure 4.29a as the column of hot water is completely evacuated. The drop is very sharp because the heating profile is uniform, so this "cliff" corresponds to the moment where the hot water is replaced by cold one. It is easy to argue that this "cliff" would be less steep in the sinusoidal case, because the water far from the middle of the assembly are heated less and less as the observer goes down.

The results of the sinusoidal heating simulations are quickly presented here. They are very similar to the uniform case, with some difference notably in the maximum temperature value reached in the channels. On figure 4.30, the temperature profile and the streamlines at the bottom of the rack are shown for $t = 110s$. The central plume is clearly present, and the sinus in the channels are still visible in D1 and D8. Note that there is also a reflux in these two outermost channels as the temperature profile is closer to the ground that they where in $t = 0s$, like in the uniform case. The maximum speed is reached at the bottom, with a value of $0.32[\frac{m}{s}]$.

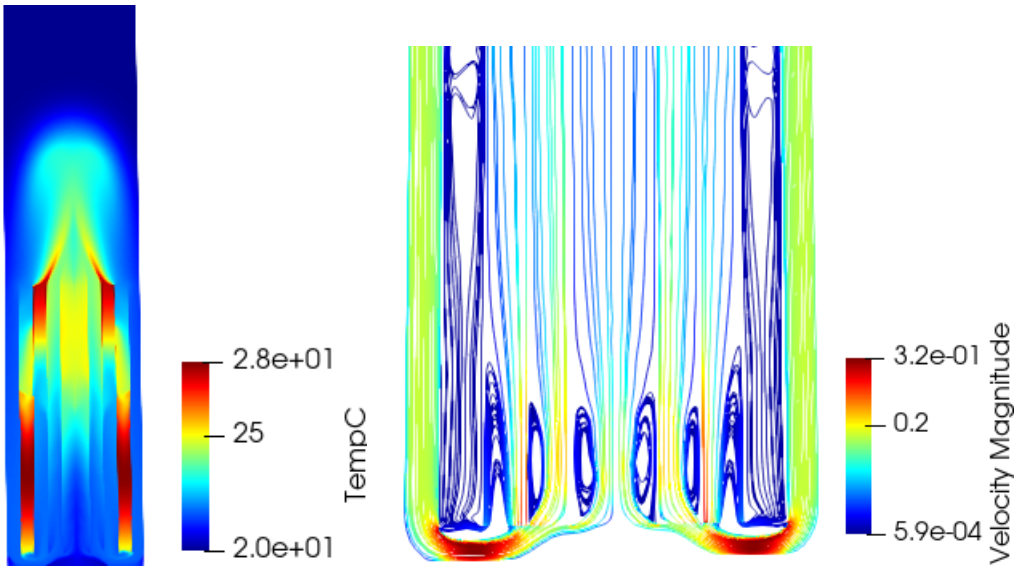

(a) (b)

Figure 4.30: temperature profile (a) and streamlines at the bottom (b) at $t = 110s$ for the sinusoidal heating case

The maximum temperature however, seems to be higher than before, with a value equal to 30 C° near the middle of D1 in $t = 130s$ (see 4.31a), and it could still be higher as the sensor is probably not exactly located on the hottest spot (the sensor is 16 cm above the bottom exit, and the hottest spot could be a bit higher). The reflux in D1 is also far less important, the vertical speed in this zone is negative but with a value very close to zero, and then it goes up in the positive value in a burst. This indicate that the hot water accumulated in there was evacuated upward (which was not the case in the uniform power distribution as the velocity profile in D1 is always negative), which explains the sudden drop in temperature at the bottom of D1 after the max is reached.

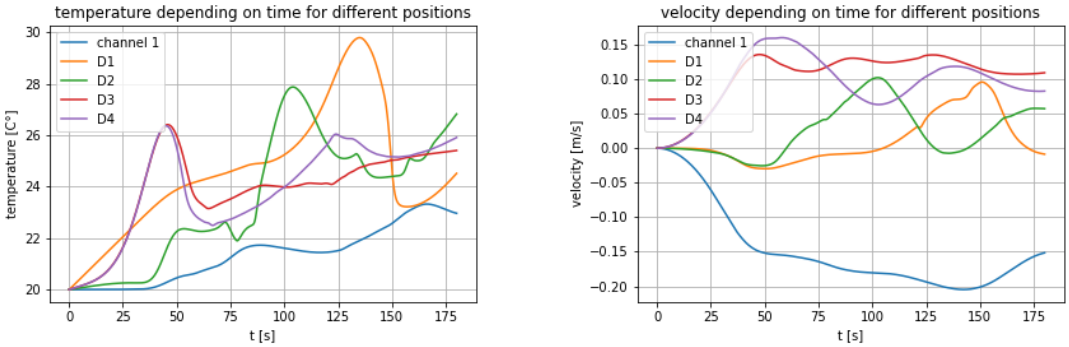

(a) (b)

Figure 4.31: graph of the temperature at the top (except for D1) (a) and the velocity (b) in the channels for the sinusoidal heating case

4.3 Second simulation round : 70kW and 35kW simulations

In this second round, the same five configurations will be studied again, but with a power of 70 kW and 35 kW over a period of 220s. As the heating sources are more powerful, a higher buoyancy is expected in the channels, which would lead to a faster flow. The width of the two free channels is unchanged at 16 cm. Unlike the previous section, only the sinusoidal heating profile case was implemented here.

4.3.1 Configuration 1 : rack full of identical nuclear wastes (70kW)

Here, only the sinusoidal heating profile is considered. Two snapshots were taken at $t = 110s$ and $t = 220s$. The temperature and velocity profiles are shown on figure 4.32.

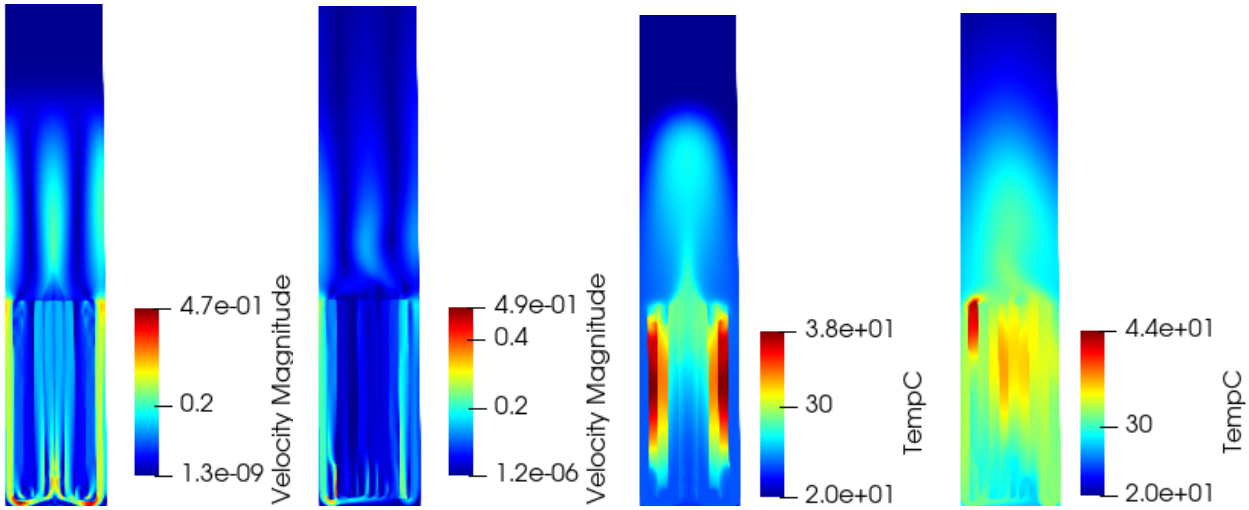

(a) (b) (c) (d)

Figure 4.32: temperature and velocity profiles of the sinusoidal heat release case at $t = 110s$ (a,c) and $t = 220s$ (b,d)

The simulation results are very similar at $t = 110s$ to the results in subsection 4.2.1. There is a symmetric plume that rise above the channels, and the two most extremes channels also contains the hot spots, but with higher maximum (the maximum temperature reaches 38 C°). This time however, the water in the D2 and D7 channels also seems to be blocked by the flows of the inner channels, even if this effect is less strong than for the two outermost channels. The local maximum there is equal to 32C°. The temperature and velocity profiles at $t = 220s$ are no longer symmetric, the plume is still visible on picture 4.32b (the two low velocity bands above the rack are still there, even if they are a bit

distorded). At the end of the simulation, there is only one hot spot localized at the top of D1, at a temperature of 44 C° (see figure 4.32d).

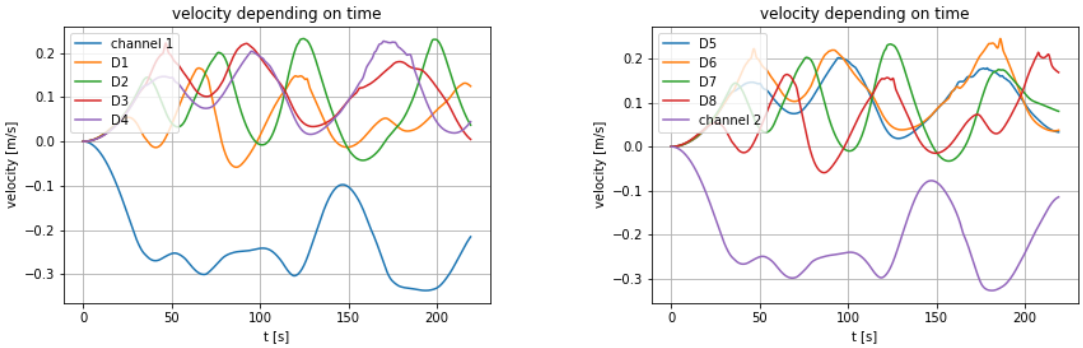

(a) (b)

Figure 4.33: graph of the vertical velocity on the left (a) and the right (b) in the channels for the sinusoidal heating case

The vertical speed in the middle of the channels are shown on figure 4.33. The curves follow a sinusoidal pattern and are coupled two by two. When the velocities in the D1 and D2 channels reach a local maximum, the velocity in the two others are close to a minimum and vice versa. This oscillation with a 180° offset was explained in 4.2.1 and is due to the flows basically blocking each others. The two graphs are almost identical as the symmetry is maintained during the first 170 seconds of the simulation. Compared to section 4.2.1, the velocities are not much higher, with a maximum of 0,2 $\frac{m}{s}$ during the first 110s compared to a maximum of 0,15 $\frac{m}{s}$ in figure 4.8. The frequency of the oscillations has increased a bit, but not by that much (the second local maximum in D2 is reached in $t = 75s$ instead of $t = 100s$ in figure 4.8), it is due to the slightly higher speed (the channels are emptying of their hot water faster).

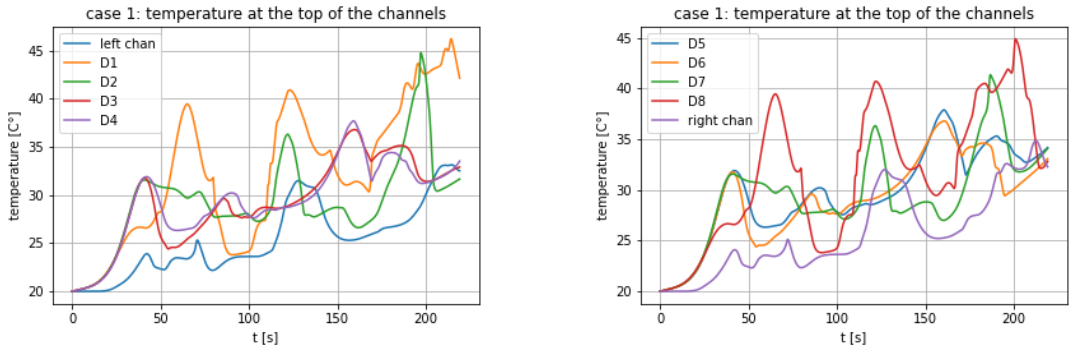

(a) (b)

Figure 4.34: graph of the temperature on the left (a) and the right (b) at the top of the channels for the sinusoidal heating case

As can be seen on figure 4.34, the local maximum of the temperature at the top of D1 quickly reaches a value of 39 C°, but the next maxima are only hotter by a few degree Celsius. This strong oscillation is due to the fact that D1 is the only channel experiencing a local reflux for short amounts of time for the first 100 seconds, so the hot region stays inside the assembly for a longer period and accumulate more heat. The sensor on top of D2 also experiment local peak of temperature, but they are less severe as the oscillations of the flow is less pronounced.

To summarize, the following can be said about the difference between this simulation and the one realized in 4.2.1:

- The speed of the flow is faster than in the lower power case (35kW-17kW), but not by that much (0,2 $[\frac{m}{s}]$ here, compared to 0,15 $[\frac{m}{s}]$).
- The general behavior is preserved, the flows oscillate in a similar manner to what was observed in the lower power configuration, even if the frequency of the flow oscillations is a bit higher.
- The temperatures reached are much higher, which is normal as the heat flux is doubled.
- The hot spots are at the top of the two outermost assemblies, the highest temperature reached is 45C°.

4.3.2 Configuration 2 : rack with older nuclear wastes in the center

Like in the previous analysis, only the sinusoidal heating profile case was simulated. Two snapshots were taken at $t = 110s$ and $t = 220s$, the temperature and velocity profiles are shown on figure 4.35.

The behavior of the flow in the 110 first seconds is similar to what was observed in section 4.2.2. The hot water seems to be blocked in most of the channels, except for D2 and D7, where the hot regions moved in the two free channels completely. The maximum temperature reached is also a lot higher than expected, with hot spot at the top of nearly all channels and a maximum temperature of 38 C°.

In $t = 220s$, there is also a rupture of the symmetry of the flow like in section 4.3.1. A very large plume is also visible on the top left in figure 4.35d, and the velocity profile visible in 4.35b just above the rack exhibit much complex features than the symmetric one in $t = 110s$ (4.35a).

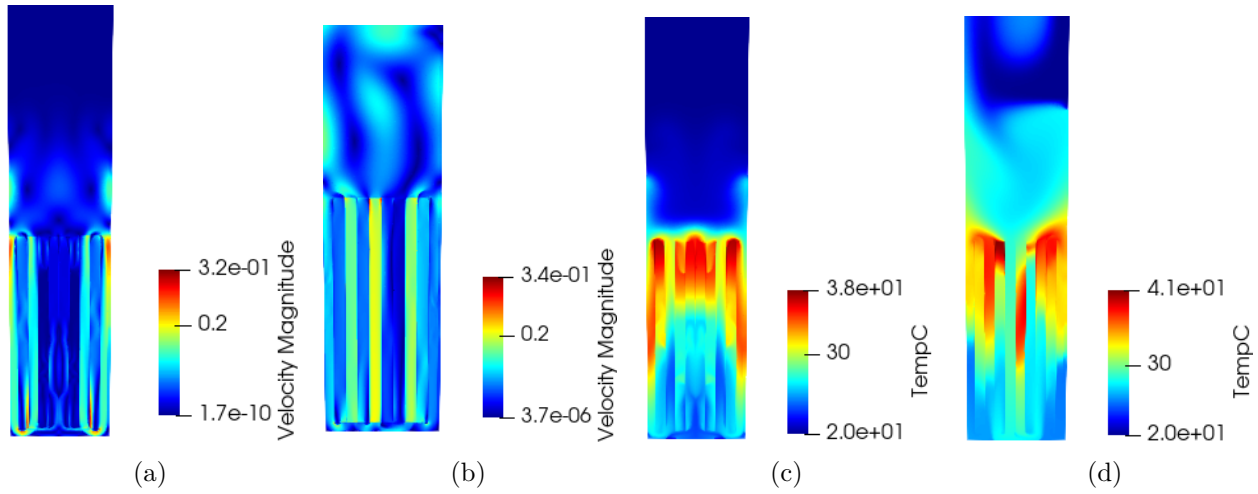

(a) (b) (c) (d)

Figure 4.35: temperature and velocity profiles of the sinusoidal heat release case at $t = 110s$ (a,c) and $t = 220s$ (b,d)

The rupture of the symmetry between the right and left part of the rack happens at around $t = 160s$ like in the section 4.3.1 as can be seen on figure 4.36a. The flow oscillates in all channels unlike the precedent case where the flow was more constant in the two free channels (see figure 4.33). A very strong reflux in D4 and D5 can be observed: it starts at $t = 120s$ and it reaches a maximum negative velocity at $t = 180s$. At first, the two symmetrical convection cells above the rack induced by the flow coming out of D2 and D7 greatly limited the vertical speed in the four innermost assemblies, which explains why the initial temperature profiles are still visible at their top in figure 4.35c. Despite this, the hot regions still managed to escape from the rack which means that at this point the innermost assemblies are full of relatively cold water (the drop of temperature is visible at $t = 130s$ on figure 4.37a in D3 and D4). Furthermore, a portion of the relatively hot region above the rack started to

move upward by buoyancy, which generated a massive convection cell that is displayed on figure 4.37b (with top speed up to $0.34[\frac{m}{s}]$). As the hot region climbs up to mix with the surrounding water near the surface of the pool, an equal amount must go down toward the bottom of the pool. The presence of this downward stream combined with the fact that the two central assemblies are full of cold water explain why there is a reflux in the center of the rack.

The velocity curves are similar to what was observed in section 4.2.2 for the first 110s. The maximum values of the velocity in D2 is higher by roughly 25% (0.19 $[\frac{m}{s}]$ instead of $0.15[\frac{m}{s}]$) in a similar fashion to what was observed in section 4.3.1 in the case with identical nuclear wastes. The frequency of the oscillation is also a little bit higher with a period of 65 seconds (measured from peak to peak on the green curve of the left graph in figure 4.36).

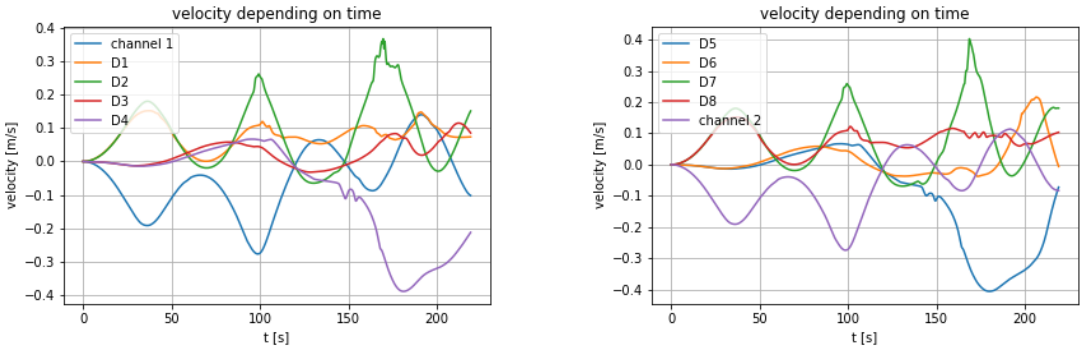

(a) (b)

Figure 4.36: graph of the vertical velocity on the left (a) and the right (b) in the channels for the sinusoidal heating case

On picture 4.37a, we see the temperature first increase and then decline in D3 and D4 as the hot water heats up and then climbs up the channels. It is interesting to see that the temperature in D1 seems to reach a plateau at $t = 100s$, which indicate that the flow speed is just high enough for the temperature profile to reach a quasi steady state. The water heats up progressively as it climbs in such a manner that locally, the temperature profile in this channel seems static for a short amount of time.

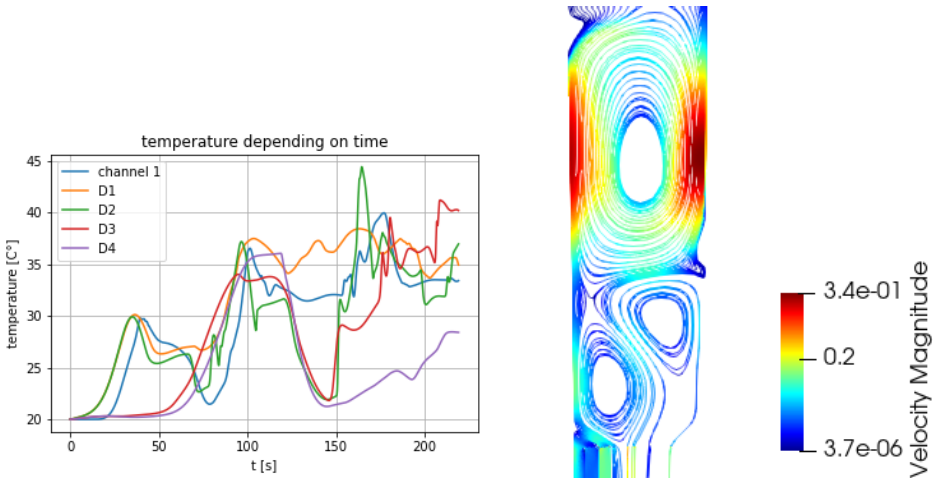

(a) (b)

Figure 4.37: graph of the temperature on the left channels (at the top) (a) and streamlines above the channels (b)

In summary, this section can be resumed as follows:

- The speed of the flow is faster by 25% than in the 35kW case, and the period of the vertical

speed oscillation is a bit shorter.

- The flow exhibit the same general behavior in the first 100s than in the lower power case, The water in the inner channel is partially trapped as the power output here is not high enough to counterbalance the mass flow coming from the convection cells.
- The temperatures reached are higher, which is normal as the heat flux is doubled.
- The flows going out of the assemblies tend to go directly in the two free channels instead of forming a huge plume like in the case analysed in 4.3.1.
- Because of that, the hot water that was accumulating above the rack will burst upward, forming a giant convection cell relatively close to the surface of the pool.

4.3.3 Configuration 3 : rack with an asymmetrical distribution

Here all the 70kW assemblies are put on the left of the rack, and the 35kW ones on the left. The heating profile is sinusoidal and the time step is equal to $dt = 1ms$. The simulation was integrated over a period of 220s.

The main feature of the flow above the rack is a big convection cell that grows over time. It starts with an irregular shape visible on top of picture (a) and (c) on figure 4.38, then it extends upward as the hot water released by the right assemblies goes up to the surface. It can be seen in picture (a) that the two streams of water going out of the assemblies in D3 and D4 go directly in the left free channel and in D1 in a similar fashion to what was observed near both free channels in the case analysed in section 4.3.2. Because of that, the water in D2 is immobilized, which explains why the local temperature is so high as it had time to accumulate heat. There was probably a small reflux there as the sinusoidal temperature profile visible in figure 4.38c is not perfectly centered. However, this local maxima is no longer present in $t = 220s$, which indicates that this hot region was evacuated either by the top or the bottom of the assembly. This hypothesis will be confirmed by the analysis of the vertical speed profiles.

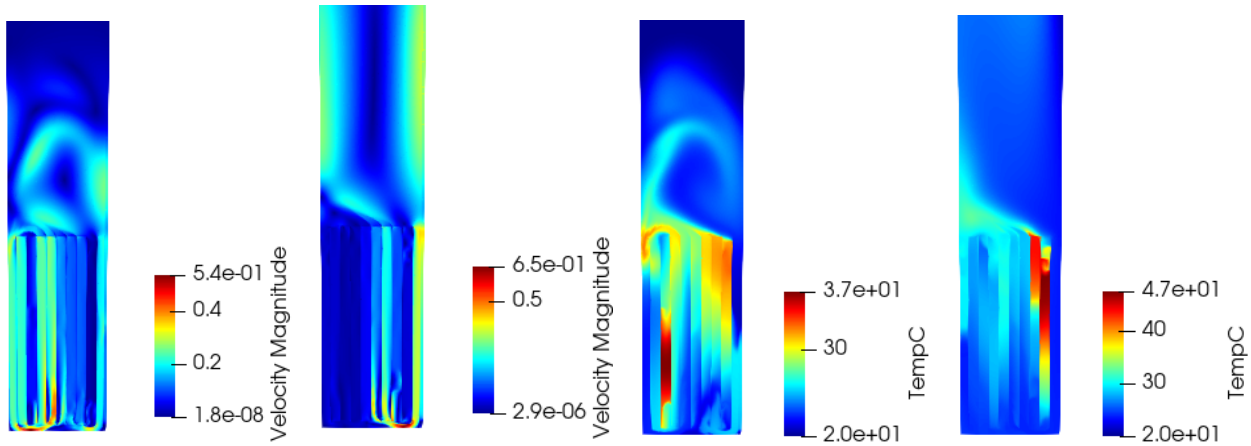

Figure 4.38: temperature and velocity profiles of the sinusoidal heat release case at $t = 110s$ (a,c) and $t = 220s$ (b,d)

The vertical velocity profiles in the channels are displayed in figure 4.39. The evolution of the speed in the channels on the left part of the rack is similar to what was observed in the section 4.2.3 in the first 50 seconds. These four assemblies experience a small reflux that reach a maximum speed in $t = 40s$, but after that the trend reverses and the water starts to rise again in D3 and D4. The reflux in D2 remains low, and then the water there also starts to rise after $t = 100s$ for the reasons explained in the previous paragraph.

Later in the simulation, the flow in the two channels D3 and D4 start to oscillate roughly in phase, with sometimes small periods of time where a reflux occurs (for instance between $t = 130s$ and $t = 170s$). Note that the velocity profiles in D1 and D2 also oscillate, but with a significant phase shift as the flow of water that goes out of D3 and D4 induces a reflux in D1.

The flow in the four assemblies on the right is much stronger than on the left at the beginning, which is normal as the water here is hotter and thus less dense. After that, the speed in the four channels containing a nuclear waste stays above $0,1[\frac{m}{s}]$ at least for the 70 first seconds. Later in the simulation, the velocity in D7 and D8 starts to decline as the water coming from the big convection cell just above them induces a local reflux, which in turn causes a local overheating of the water, that can be seen at the right of picture 4.38d.

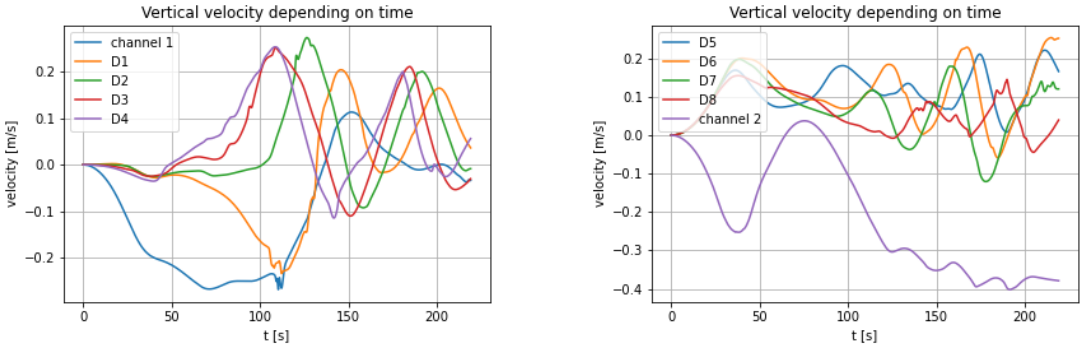

(a) (b)

Figure 4.39: graph of the vertical velocity on the left (a) and the right (b) in the channels for the sinusoidal heating case

The streamlines in $t = 220s$ and the temperature are shown respectively on figure 4.40b and figure 4.40a. The maximum temperature seems to be reached at the top of channel D8 with a maximum value of 45 C°. In reality, it is reached just below as can be seen on picture (d) of figure 4.38 with a value of 47 C°. The hot region is pushed downward by the reflux, which explains why the sensor saw a drop in the temperature as cooler water from above the rack was flowing in.

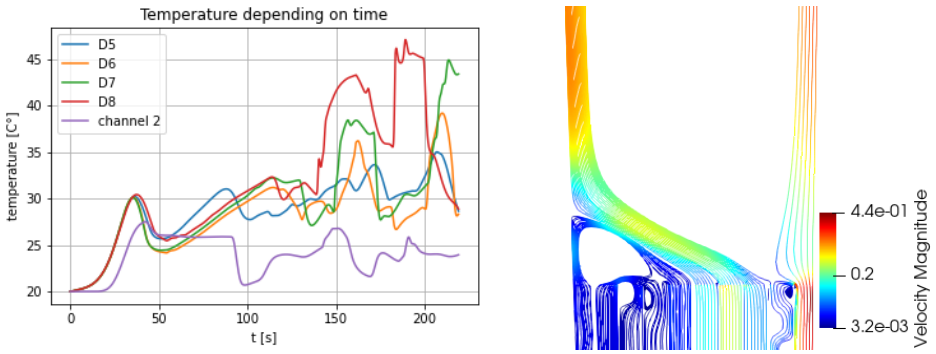

(a) (b)

Figure 4.40: graph of the temperature in the right channels (on top) (a) and streamlines above the channels at $t = 220s$ (b)

To summarize the content of this section :

- The inversion of the initial reflux in the channels on the left is faster in the simulation with a 70kW heat source.
- The velocity in the channels on the right tend to stay quite high at least in the 130 first second.

After that, there is a little bit of reflux in the D7 and D8 channels due to the large convection cell.

- The temperature field reaches a maximum of 47 degree Celsius in the D8 channel. There are also cooler hot spots in the channels on the left, but they only last a short period of time before the flow start to go up again, evacuating the hot water upwards.
- The hot water coming from the assemblies on the right form a large plume, which induces a large convection cell. The hot water coming out of the assemblies on the left tends to evacuate either directly in the left free channel, or in the directly adjacent channels.

The water in the channels on the right is blocked by the reflux coming from the large convection cell. This reflux lasts for a very long time, which explains why temperatures at the top of D8 are so high.

4.3.4 Configuration 4 : rack with an alternate distribution of assembly

The simulation described here was launched with sinusoidal heating profiles in the rack and with assemblies either containing nuclear wastes with a 70kW or 35kW thermal output. The time step was set to $dt = 1ms$.

The temperature and velocity profiles in $t = 110s$ and $t = 220s$ are displayed in figure 4.41. The flow follows a similar trend to what was observed in section 4.2.4 for the lower power case: First, the water going out of the assemblies flows directly in the free channels, and then a large plume forms above the rack and the hot water goes higher in the pool. The hot spots are not located at the same place for the two studied snapshot: in section 4.2.4, they were at the top of D2 in $t = 110s$ and at the top of D2 and D4 in $t = 220s$, whereas in the present case, they are located at the top of D4 and D6 in $t = 110s$, and on the top right in $t = 220s$. The temperature encountered are higher due to the higher total power of the assemblies.

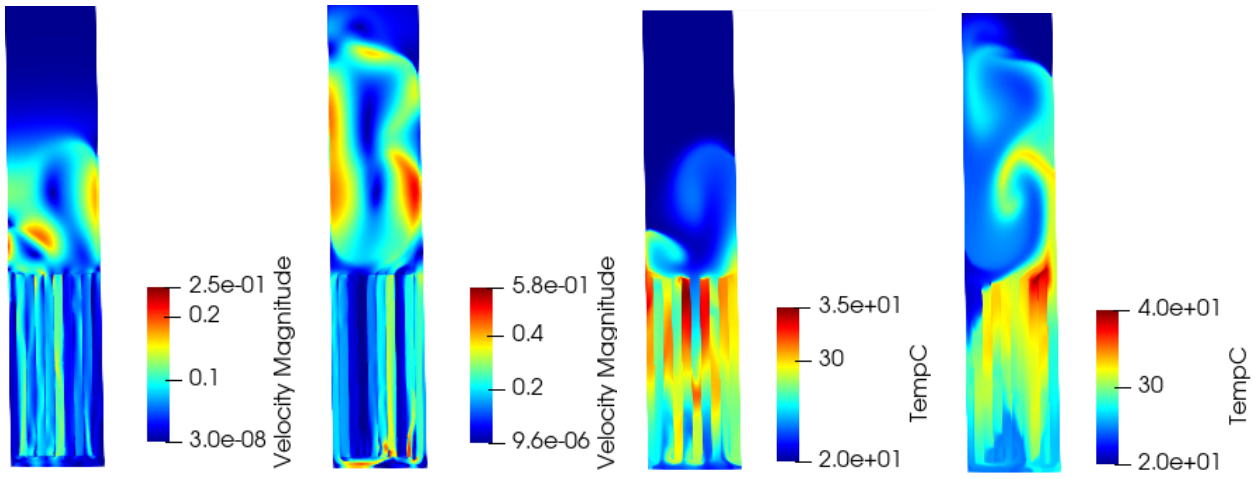

(a) (b) (c) (d)

Figure 4.41: temperature and velocity profiles of the sinusoidal heat release case at $t = 110s$ (a,c) and $t = 220s$ (b,d)

The oscillations of the vertical velocity in D2 reach a higher first maximum compared to 4.25a and the frequency of the oscillations of the speed is also higher by 33% (there are four local maxima on the green curve of figure 4.42a, and three on figure 4.25a). The global shape of all the velocity curves excepted D5 stay the same between the two power cases, and what we said for D2 is also true for the other channels (all the curves have a slightly higher speed and higher frequency). In D5, the reflux that happens after $t = 80s$ is much stronger in the high power simulation, with a maximum speed of $0.3[\frac{m}{s}]$ compared to $0.1[\frac{m}{s}]$ in figure 4.25b.

The maximum temperature is reached at the top of D6 in $t = 210s$ with a value of 45 C° (see figure 4.43b). When looking at the corresponding velocity curve on figure 4.42b, one can point out the fact that the local velocity (orange curve) was very low in the instant just prior the detection of this maximum, with even a small reflux in $t = 170s$. As the water was static in the assembly, its temperature rose significantly, which explains why the maximum was detected in this channel. It is also interesting to note that at any given time after $t = 70s$, the temperatures measured at the top of the channels on the left of the rack were within 7C° of each other (the maximum of the difference in temperature of any pair of sensor is lower than or equal to 7C°), all the curves are in a rather narrow band that grows before stabilizing around 32 C°. This is explained by the fact that the vertical speed in the assemblies containing a 70 kW nuclear waste are much higher than the one in the low power assemblies, so the heat is evacuated away more efficiently and the temperature in the four channels are close to one another despite the big difference in thermal output.

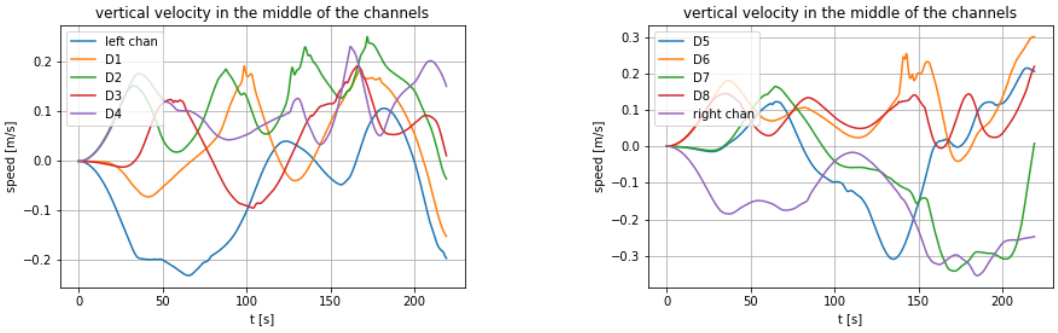

(a) (b)

Figure 4.42: graph of the vertical velocity on the left (a) and the right (b) in the channels for the sinusoidal heating case

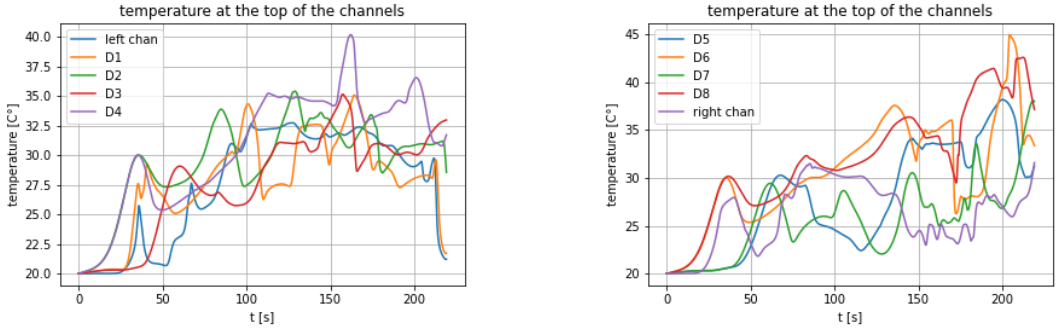

(a) (b)

Figure 4.43: graph of the temperature on the top of the left (a) and and the right channels (b)

4.3.5 Configuration 5 : inverted centered distribution

Similarly to the case analyzed in section 4.2.5, the 70kW assemblies are put in the middle, while the four outermost channels contain a 35kw nuclear waste. the time step is $dt = 1ms$ as usual, and only the sinusoidal heat release profile is studied.

There are two small convection cells just above the rack, but contrary to what was observed in section 4.2.5, the flow going out of the innermost assemblies split in two and heads directly toward the walls (two small jets are visible in the middle of figure 4.44c). It means that the direction of rotation of the two cells is reversed compared to the lower power case. A reflux is still observed in the two outermost regions (the offset of the temperature profile at the bottom of D1 and D8 is a strong indicator) and the maximum temperature reaches 32 C°.

Another major difference between this simulation and the one realized in 4.2.5 is that the symmetry is broken in $t = 220s$. Indeed, the system of cells above the rack merged in one big cell that rotates clockwise. Because of that, the picture (d) in figure 4.44 shares some similarities with picture (c) of figure 4.38. There seems to be a reflux at least in the three channels on the right, but it must be confirmed by the analysis of the velocity curves.

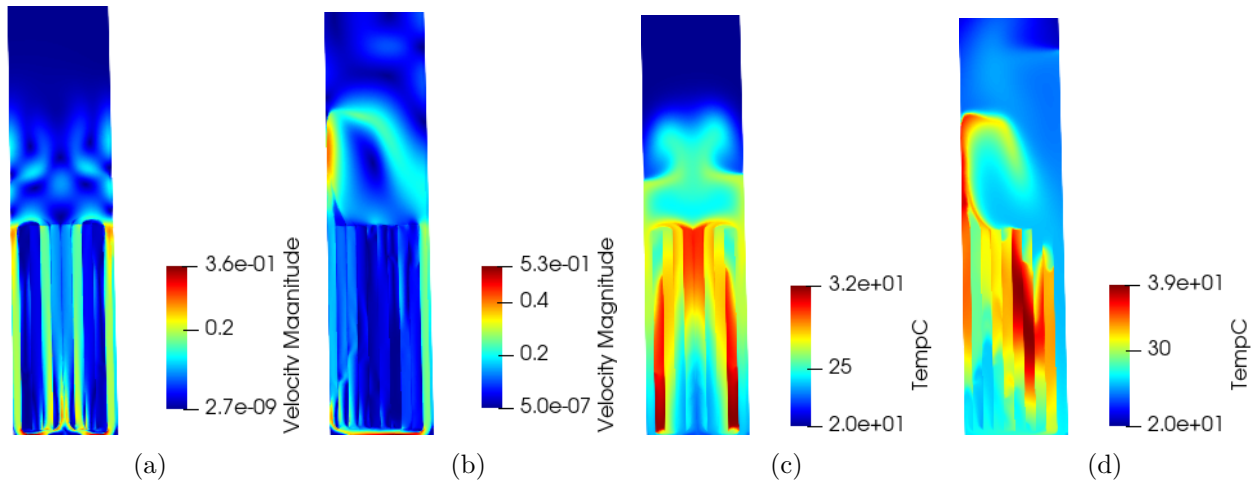

(a) (b) (c) (d)

Figure 4.44: temperature and velocity profiles of the sinusoidal heat release case at $t = 110s$ (a,c) and $t = 220s$ (b,d)

The flow symmetry is broken at $t = 140s$ (that's the moment when the speed in D1 and D8 start to diverge). The moment at which the large convection cell expands to the point where it takes all the width of the pool can be estimated by looking at the instant at which the flow in the left free channel start to go upward. On the graph 4.45a, we see that it happens at $t = 210s$.

At the beginning of the simulation, there is a small reflux in both D1 and D2 (and in their counterpart on the otherside), but the flow quickly reverse back to normal in D2, while maintaining a low velocity reflux of $0.02[\frac{m}{s}]$ in D1. After 100 seconds, the hot water accumulated in D1 (and D8) finally climbs up to be released in the area above the rack. Normally, the symmetry shouldn't be broken as the initial conditions and the domain are perfectly symmetric, so the reason why it happens is due to small errors accumulated when the equations were integrated over time. It is not a big issue though, because in a real life situation, the domain wouldn't be perfectly symmetric anyway, so the symmetry would also be broken pretty quickly.

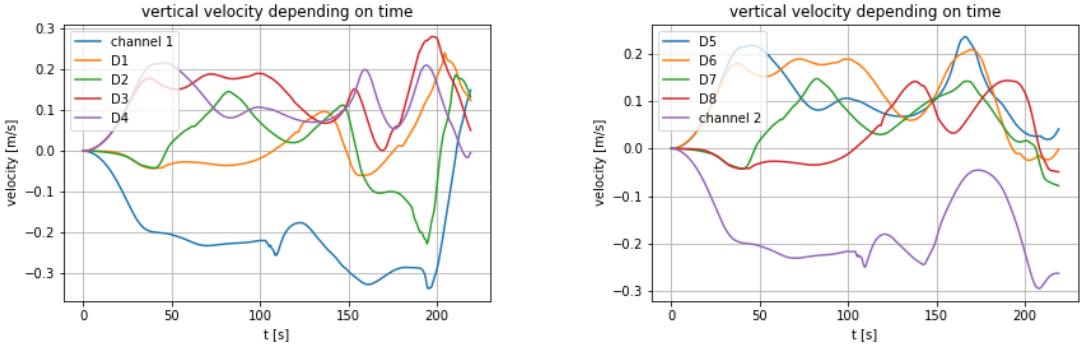

(a) (b)

Figure 4.45: graph of the vertical velocity on the left (a) and the right (b) in the channels for the sinusoidal heating case

The hot water accumulated in D8 exited the channel entirely from $t = 100s$ to $t = 210s$ as can be seen on the velocity curve on figure 4.45, while the water in D1 mostly stayed inside its assembly. As a consequence, this water heated up more, and when it exited the channel in $t = 170s$ (orange curve in the left graph of figure 4.45), its temperature was higher. Then, the flow entered the free channel on the left, and because of that higher buoyancy, the water stopped before starting to flow upward, which caused the big convection cell and the subsequent reflux in the channels on the right. A similar decrease of the speed in the right free channel can be observed starting at $t = 150s$ when the hot water flowing out of D8 starts to come in, but as its temperature is lower (31C° instead of 37 C°, see picture 4.46a), the buoyancy force is not strong enough to reverse the flow.

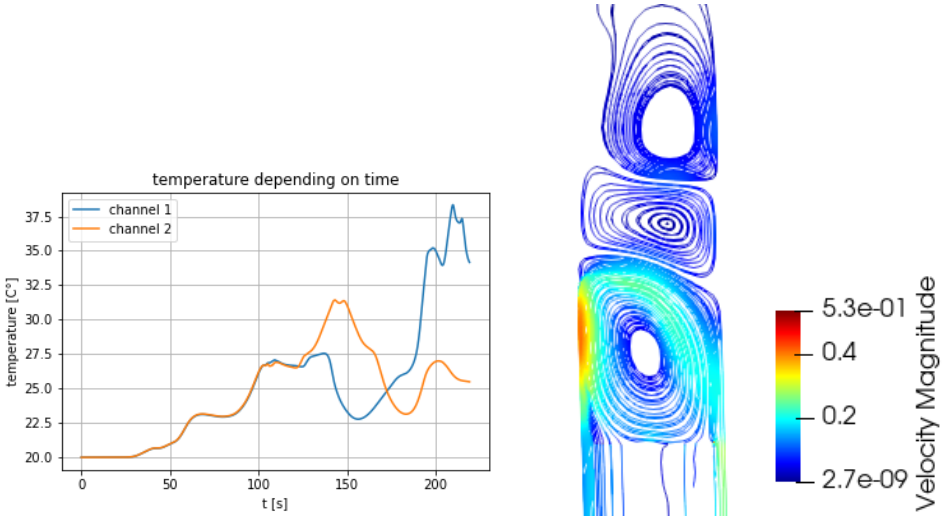

(a) (b)

Figure 4.46: graph of the temperature on the free channels (upper part) (a) and streamlines above the channels at $t = 220s$ (b)

Here is the summary of this section :

- A rupture of the symmetry of the flow begins at $t = 140s$. It didn't happen in the simulation at lower power in section 4.2.5, probably because the simulation was not long enough.
- A massive convection cell appears, which effectively blocks the water in the four assemblies on the right in the latest stage of the simulation
- The maximum temperature reached is 39-40C° C°, which is lower than in the previous configurations (it is 47 C° in section 4.3.3 for instance).
- There is no oscillation of the vertical speed at least in the first 150 seconds.
- The hot spots are located at the bottom of D1 and D8 in the first phase, and at the top of the channels on the right near the end of the simulation.

4.4 Third simulation round : 70kW and 35kW assemblies in a pool with a wider gap

Finally, in this last section, the flow in the five basic cases will be studied with an increased distance of 24cm between the walls and the rack. Only the sinusoidal heat release profile is considered here. The power level of the assemblies is the same as in the previous round, with the most powerful nuclear wastes releasing 70kW, and the least powerful releasing 35 kW. The different curves will be mainly compared with the curve of the second simulation round as to establish the impact of a wider gap without power change.

4.4.1 Configuration 1 : rack full of identical nuclear wastes

We will start by the first case with a uniform distribution in the rack. In figure 4.47, the graph of the vertical velocity at the top of the channels was displayed in parallel to the curves obtained in section 4.3.1. At the beginning of the simulations, the dashed and continuous curves are almost indistinguishable from one another. After a while, the curves for D1 and D2 start to diverge significantly in $t = 80s$. The velocity curves of the free channels diverge even more quickly (in blue at $t = 35s$), but they keep the same overall shape (same location of the local maxima and minima). Indeed, as the flows in the outermost assemblies stay the same during the first 70 seconds, the free channel on the left undergoes the same mass flux than in the 16cm gap case but with a larger cross section, it means that the overall shape of the blue curve stays the same but the overall speed is reduced. In theory, the velocity there should be reduced by 33% (a 50% increase of the width would imply a 33% decrease at constant mass flow), but in practice, the reduction is lower than that because the flow in the inner channel is more important in the 24cm case (see figure 4.47b). Thus, a wider gap will increase the flow in the four innermost channel, at least in the early time of the simulation.

As stated before, the velocity curves of the assemblies finally diverge from the ones of the 16cm gap case after $t = 80s$. Beyond that point, the speed of the flow is still oscillating, but there is no more reflux in D2. To summarize, a wider gap induces a faster flow in the innermost assemblies and the speed variations in the channels are less pronounced.

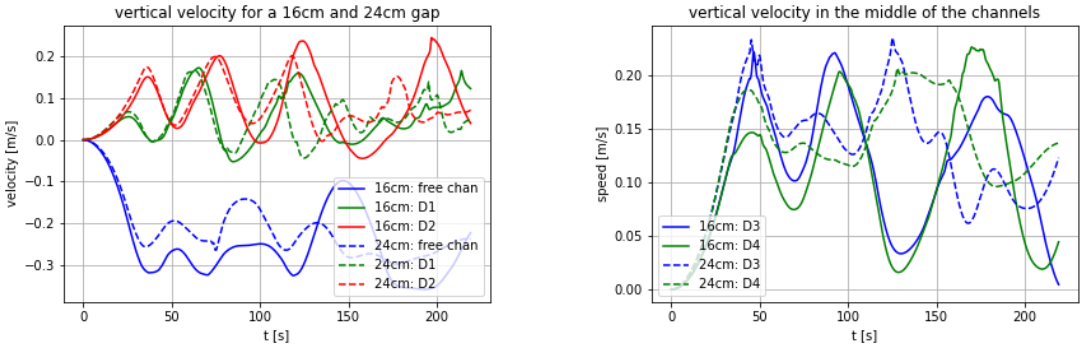

(a) (b)

Figure 4.47: graph of the velocity in the left part of the rack for the 16cm gap (continuous lines) and the 24 cm gap (dashed lines)

The temperature heat maps are displayed on figure 4.48. As could be observed in the two graphs of figure 4.47, the simulation results in $t = 110s$ in the 16cm and 24 cm cases are very similar, with the presence of two big convection cells on top of the rack in both cases. Note that the maximum temperature reached in $t = 110s$ is unchanged at 37C°, while it reaches a maximum of 48 C° in $t = 220s$. This maximum is reached in the same area of the domain (upper part of D1) as in the 16cm gap case.

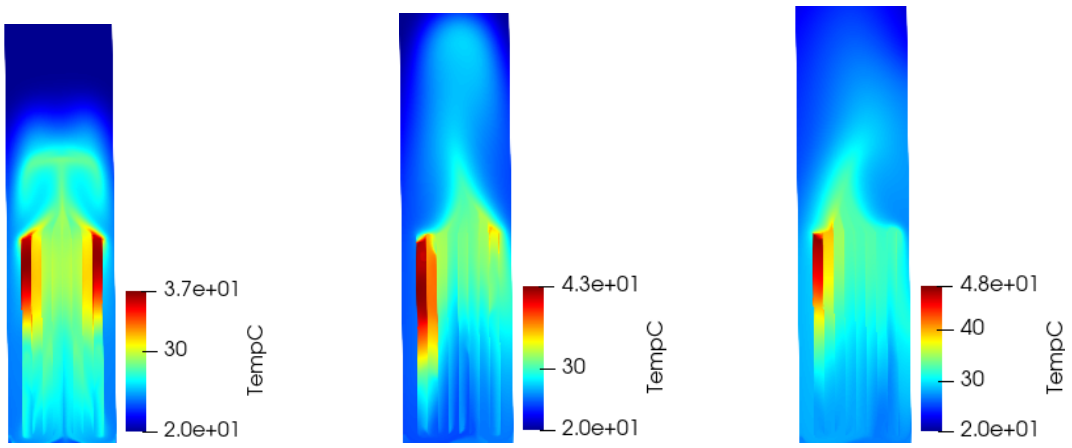

(a) (b) (c)

Figure 4.48: temperature profiles of the sinusoidal heat release case at $t = 110s$ (a), $t = 160s$ (b) and $t = 220s$ (c)

When looking at the temperature curves in figure 4.49a, we see that after $t = 150s$, the temperature in the D1 and D2 channels are almost always superior in the 24 cm gap case. The temperature in the left free channel stays close to the one observed in the 16cm case, but it is not a surprise as the water coming in is mainly water coming from the convection cells that had plenty of time to mix with colder water from the top of the pool, so the temperature in this location is not that impacted by what is happening in the assemblies. The temperature oscillations in D2 are less severe in the 24 cm gap case, the increase in T° is steady and doesn't undergoes short brutal variations like the one observed on the red curve on figure 4.49a at $t = 195s$. The temperature curves at the top of D3 and D4 shown in figure 4.49b also oscillates with a lower amplitude in the wider gap case and we also see that they are below the continuous curve most of the time, it is explained by the fact that the flow in the four assemblies in the middle is much regular than before.

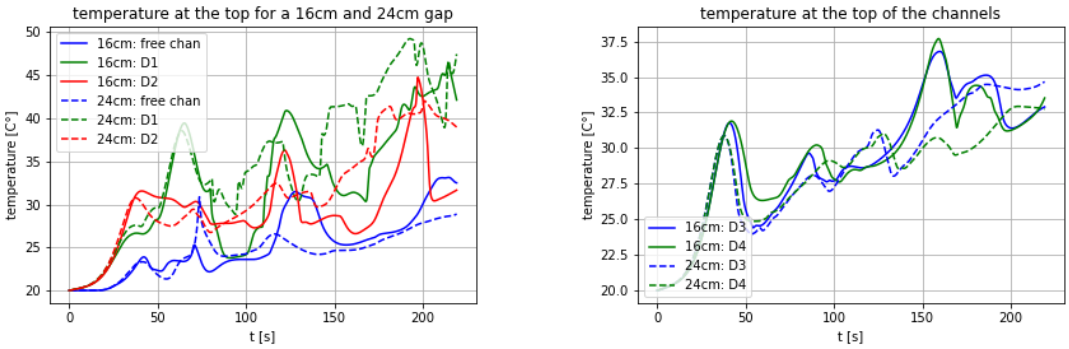

(a) (b)

Figure 4.49: graph of the temperature at the top of the assemblies in the left part of the rack for the 16cm gap (continuous lines) and the 24 cm gap (dashed lines)

The main differences between the 16cm and the 24cm case in this configuration of the assemblies can be summarized as follows :

- The speed of the flow in the outermost assemblies are almost identical during the first 80 seconds, then the flow in the assemblies undergoes less velocity variation.
- The temperature at the top of D2 increases more steadily than in the 16cm case, and the variations are less abrupt.
- The hot spots are still on the upper left.

4.4.2 Configuration 2 : rack with older nuclear wastes in the center

The temperature profiles at three different time steps are shown on picture 4.50. The pattern of the flow is similar to the one observed in the 16 cm gap studied in section 4.2.2 as expected, there are two convection cells on top of the rack that push the water in the four central assemblies toward the ground (so there is a reflux there). We can see that the reflux is so strong that it has pushed all the hot water out of the two assemblies in the center in $t = 160s$ (see picture 4.50b).

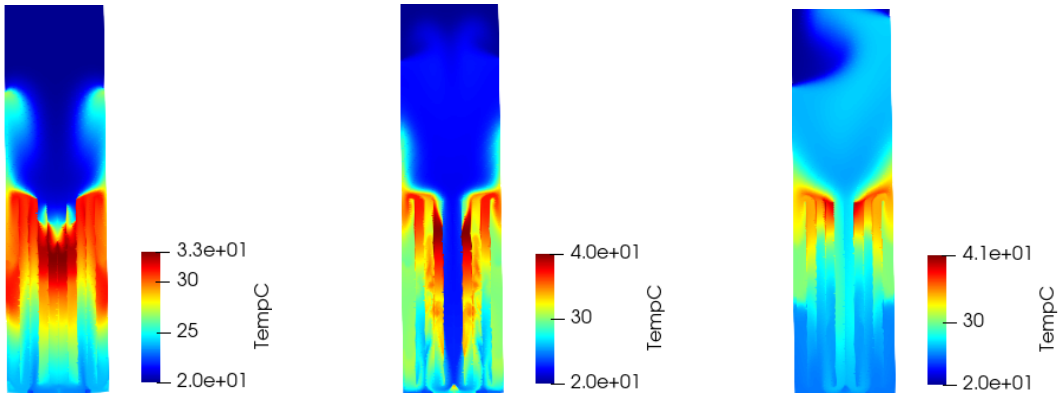

(a) (b) (c)

Figure 4.50: temperature profiles of the sinusoidal heat release case at $t = 110s$ (a), $t = 160s$ (b) and $t = 220s$ (c)

The velocity profiles are displayed just below in figure 4.51. Once again, the overall shapes of the curves are very similar. However, the velocity in the D1 channel is higher on graph 4.51a (dashed curve above the continuous one in $t > 60s$), which means that the heat is evacuated more efficiently than before. The amplitude of the speed oscillations in D2 are lower, so locally the flow is more regular and experiment lower maxima and higher minima. When looking at the graph on 4.51b, we see that initially, the flows in the inner channels are blocked during a shorter amount of time (there is no small reflux in $t = 30s$ and the values start increase in $t = 25s$ compared to $t = 50s$ for the continuous curve). As the free channels are larger, the water initially coming out the top of the inner and the outer channels can be evacuated downward more efficiently as the flow in the channels containing an assembly are not blocking each other as much as in the 16cm gap simulation. The bottleneck effect of the free channels is reduced. However, it should be noted that the free channels are not wide enough to prevent a reflux in the two central channels later in the simulation, it is just going to happen sooner.

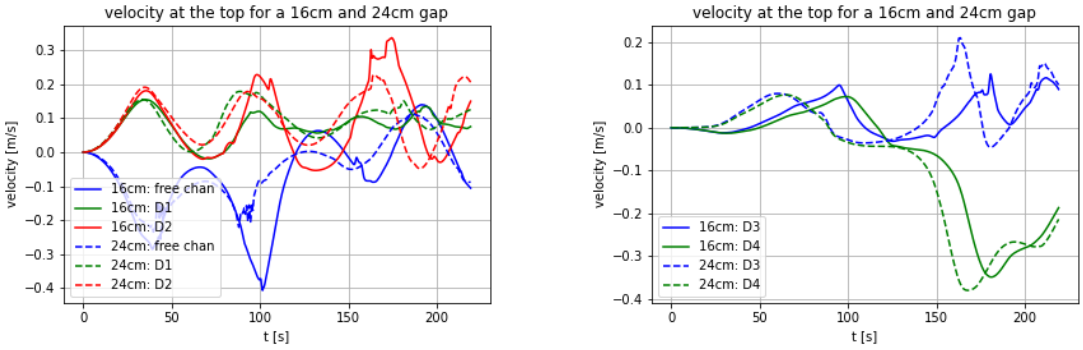

(a) (b)

Figure 4.51: graph of the velocity in the left part of the rack for the 16cm gap (continuous lines) and the 24 cm gap (dashed lines) for configuration 2

In opposition to this apparent dampening effect of a larger gap on the velocity in the outermost channels, it seems that the opposite happens in the innermost channels as higher maxima in the two

velocity curves for the D3 and D4 channels are observable at around $t = 160s$ in graph 4.51b. The flow in D4 is mainly driven by the water coming from the two convective cells above the racks, which are fed by the water flowing out of D3, so the two curves are directly related and the higher value of the speed in D3 explains the higher (negative) value observed in D4 in $t = 160s$.

We also see the correlation between the temperature and velocity profile by comparing 4.52b and 4.51b as the early flow in D3 and D4 is correlated with an early increase of the temperature and lower subsequent maxima as the water had less time to heat up. The temperature in D2 doesn't undergo a sudden drop at $t = 120s$, which shows that the temperature profile is less irregular, which is correlated with the fact that the velocity profile doesn't vary as much as in the 16 cm gap case.

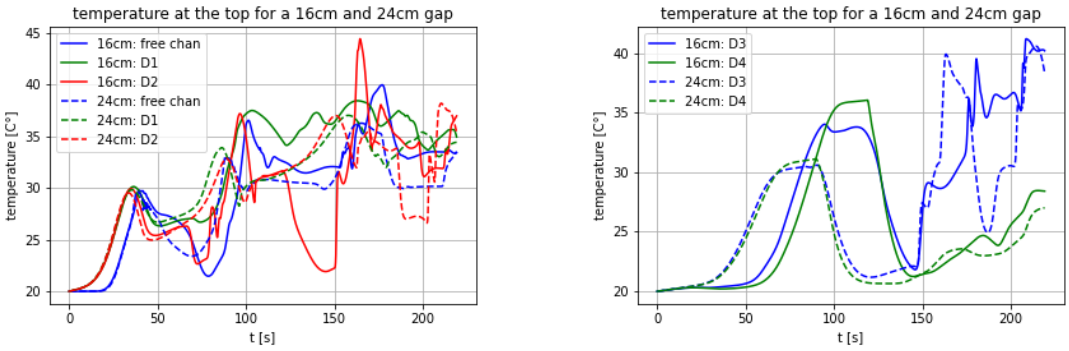

(a) (b)

Figure 4.52: graph of the temperature at the top of the assemblies in the left part of the rack for the 16cm gap (continuous lines) and the 24 cm gap (dashed lines) for case 2

4.4.3 Configuration 3 : rack with an asymmetrical distribution

In graph 4.53, the velocity curves for a simulation with a gap of 24 cm are displayed and compared with the velocity curves of the 16 cm case. The results presented here are compared with the simulations results presented in section 4.3.3.

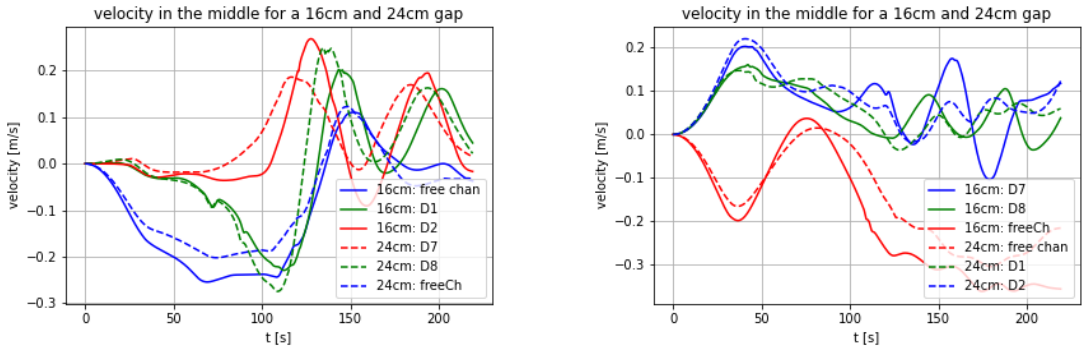

(a) (b)

Figure 4.53: graph of the velocity in the left part and the right part of the rack for the 16cm gap (continuous lines) and the 24 cm gap (dashed lines)

The attentive reader will have noticed that the high power assemblies are on the left part of the rack, while they were on the right in the simulations done in section 4.3.3 and 4.2.3. This is due to a careless mistake, but it doesn't impact the validity of the results as the velocity curves can simply be flipped with respect to the symmetry axis. This explain why we compare D1 with D8 and D2 with D7 in the following paragraphs for instance, as they are expected to have similar flow and temperature profiles.
The dashed and continuous curves keep the same overall shapes during the whole simulation for the

flow in the channels with a lower thermal output (see picture 4.53a). Because of the wider gap near the walls of the pool, one might expect the reflux to decrease in all the assemblies on the right part of the rack compared to what is seen in section 4.3.3. This is not what is observed, D8 will actually experience a greater reflux with equally severe velocity oscillations. Because of that, and as the free channels are wider, a lower fraction of the water going out of the high power assemblies is available to induce a reflux in D7. As a consequence, the oscillations there will start earlier than in the 16cm gap case and the reflux that is observed in $t = 150s$ for the 16cm gap case will be almost non-existent. Similarly to what was explained in section 4.4.1, the lower speed in the two free channels is due to their increased width.

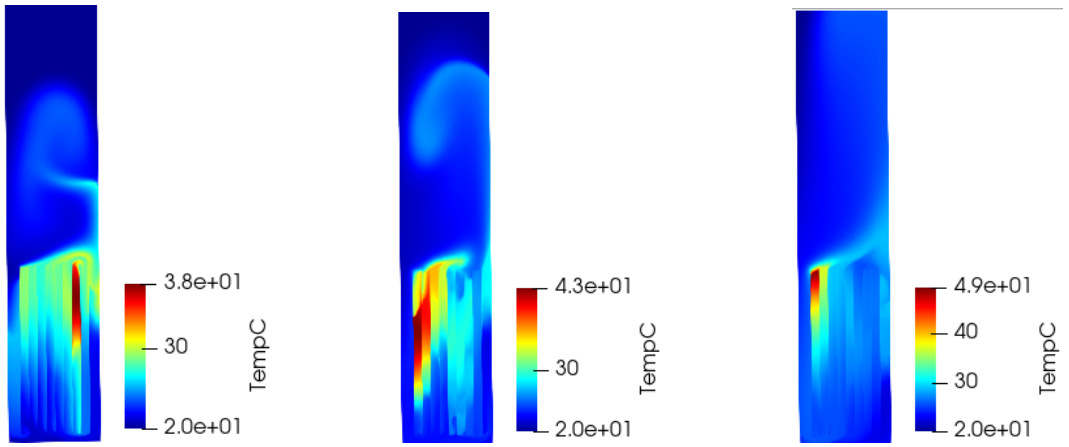

(a) (b) (c)

Figure 4.54: temperature profiles of the sinusoidal heat release case at $t = 110s$ (a), $t = 160s$ (b) and $t = 220s$ (c)

The convection cell on top of the rack has the same shape than the one observed in section 4.3.3. The observable high temperature regions in the D7 and D8 channels in $t = 110s$ are very similar to the one observed in D2 in the 16cm gap case.

The curves of the temperature at the top of the low power assemblies in figure 4.55a follow the same trend in the 16cm and 24cm gap case. The temperature in D1 and D2 undergoes the same brutal increase in $t = 100s$ with maxima reaching up to 37C°, followed by a moderate drop and a temporary plateau. However, the temperature value at which the D1 plateau stabilizes momentarily are a bit higher in the simulation with a 16cm gap (the green continuous curve oscillate a bit between 30C° and 33C° whereas the dashed one stays between 25C° and 29C°).

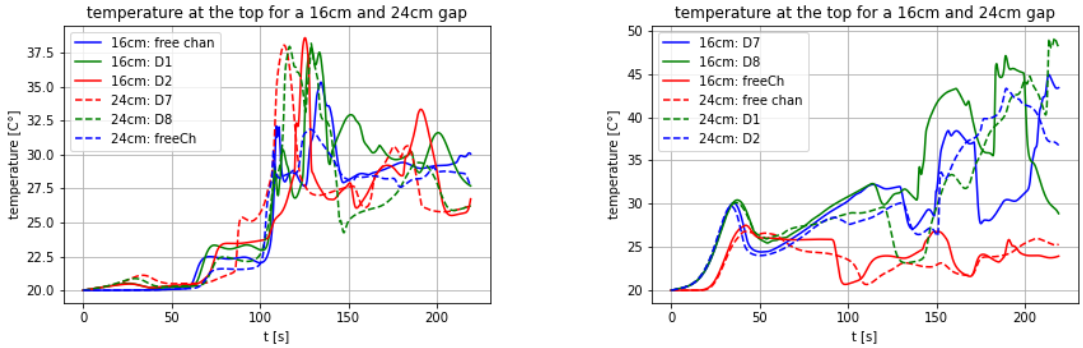

(a) (b)

Figure 4.55: graph of the temperature at the top of the assemblies in the left and right part of the rack for the 16cm gap (continuous lines) and the 24 cm gap (dashed lines)

To summarize, the widening of the gaps near the walls will not automatically reduces the reflux in

the assemblies with an older nuclear waste as it was seen in the D8 channel.

4.4.4 Configuration 4 : rack with an alternate distribution of assembly

The results of the simulation with a 24 cm gap and an alternate power distribution in the rack are presented in this section. All the curves on the graph of the speed and the temperature will be compared to the ones obtained in section 4.3.4. Similarly to the precedent section, the position of the assemblies were inverted compared to the simulation with a 16 cm gap but it is not a problem as one can still compare the two simulations by using the same orthogonal symmetry. The corresponding curves have the same color in order to make it easier to compare them.

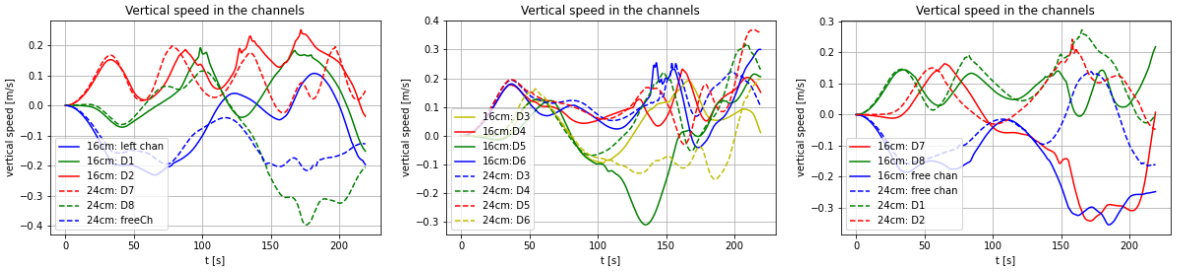

(a) (b) (c)

Figure 4.56: graph of the vertical velocity in the rack for the 16cm gap (continuous lines) and the 24 cm gap (dashed lines)

As in the other cases analyzed in this chapter, the flows in the channels during the first 50 seconds are almost identical, before gradually diverging. However, whereas the velocity profiles in the first three section show approximately the same general behavior with a 16cm or a 24cm gap, here the general behavior changes much more. Indeed, the flows in channels D6 and D8 undergo a pronounced reflux from halfway through the simulation to the end (see figure 4.57a). Similarly, the flow in the free channel on the right (blue dashed curve in graph 4.57a) is also directed downwards with a much higher velocity than the simulation with a 16cm gap. If we now look at the other side of the rack on the graph 4.57c, we can also see that this massive reflux is compensated for by an increase of the speed flow in D1 (compared to the continuous green curve), and a reversal of the direction of the flow in D2 and the left free channel.

To summarize shortly, in the 24cm gap case the right side of the rack experiments a massive reflux in the low power assemblies (D6 and D8) after 130 seconds, while the left part of the rack undergoes a positive flux most of the time (excepted for the free channel). The reflux is maximal in the low power channels because the water within is heated more slowly, so the buoyancy force that usually oppose the reflux is less strong. In the 16cm gap case, the situation is reversed, and it is the portion of the rack located below the hot plume that experiments a strong reflux (see the continuous blue and red curves on figure 4.57c).

The speed in D7 is also lower in the 24cm gap case (as can be seen on the two red curves of figure 4.57a), so the heat can no longer be evacuated as efficiently as before, which explain the sudden increase in temperature in the middle of this channel in $t = 180s$, visible on figure 4.57a. On the contrary, the temperatures in D8 and the right free channel are lower than in their counterparts because of the massive reflux these two channels undergo at the same time. The low temperature field in this region is clearly visible on the right of picture 4.58b and on the green and blue dashed curve on figure 4.57a. Note that the maximum temperature in the middle of the assemblies is 40 C° in both cases, but this value is not reached in the same channel.

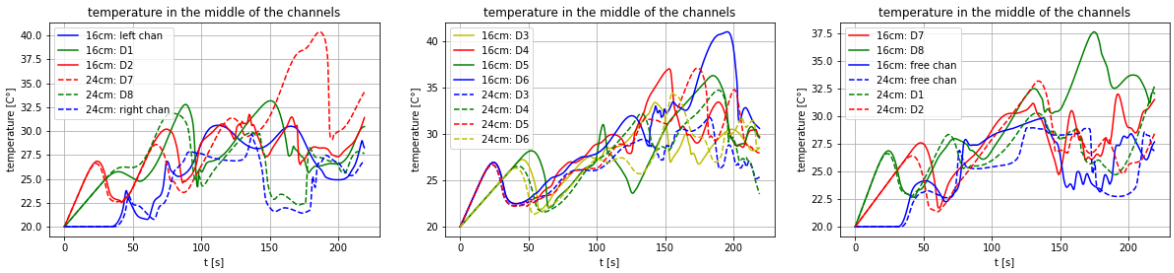

(a) (b) (c)

Figure 4.57: graph of the temperature in the middle of the rack for the 16cm gap (continuous lines) and the 24 cm gap (dashed lines)

To sum up, widening the space between the walls and the rack will have a huge impact on the flow after 130 seconds of simulations. Indeed, the channels experiencing a reflux will not be the same despite the fact that the convection cell above the rack does not change its direction of rotation. As a result, the region with the highest temperature will not be at the same place.

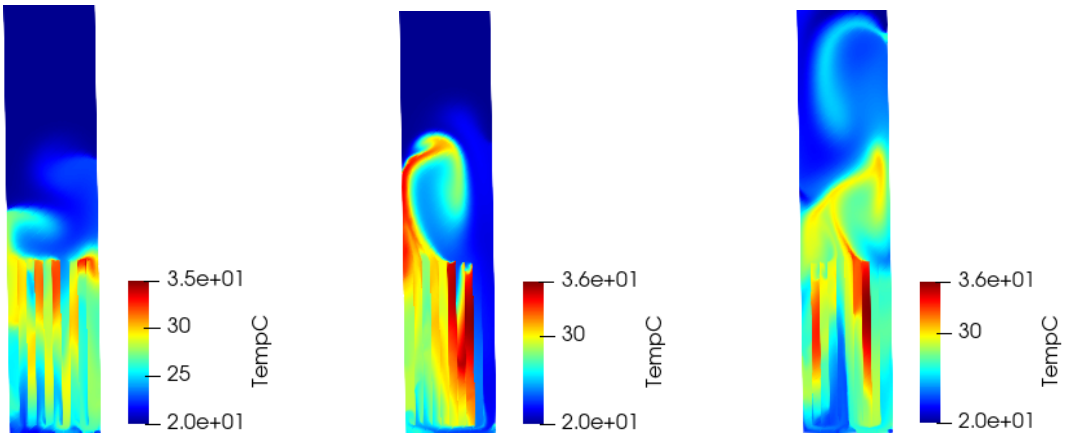

(a) (b) (c)

Figure 4.58: temperature heat map of the sinusoidal heating profile configuration at $t = 110s$ (a), $t = 160s$ (b) and $t = 220s$ (c)

4.4.5 Configuration 5 : inverted centered distribution

The temperature and velocity profiles presented here will be mainly compared with the results obtained and studied in section 4.3.5. The heat profile is sinusoidal and the total duration is 220s like the precedent ones.

The shape evolution of the convection cell above the rack follows the same sequence of event as in section 4.3.5 with first two convection cell bringing the hot water from the assemblies to the free channels, followed by the formation of a unique convection cell as large as the pool (visible on figure 4.60c). The graph of the vertical speed at the top of the channels are presented in figure 4.59. The first visible consequence of the larger gap in the early stages of the simulation is that most of the downward water flow can pass through here and as a consequence, the reflux in D1 is less severe than in 4.3.5. The flow in this channel changes direction to be directed upward in $t = 75s$, and the local maximum that follows reaches a higher value at $0,18[\frac{m}{s}]$ (compared to $0,1[\frac{m}{s}]$). Because of that, most of the hot water has been evacuated from D1 and D8 in 4.51a whereas a large hot region is clearly still visible at the bottom of D1 in figure 4.44c. However, as D1 is completely filled with cold water in $t = 110s$, the buoyancy in this region become lower than in the left free channels (which was filled with relatively hotter water coming from the assemblies in the 100 first seconds) and as a consequence, a massive reflux happens here between $t = 120s$ and $t = 210s$. This phenomenon is clearly different from what

happens in the 16 cm gap case during the same period, where a small reflux is observed only during 20 seconds.

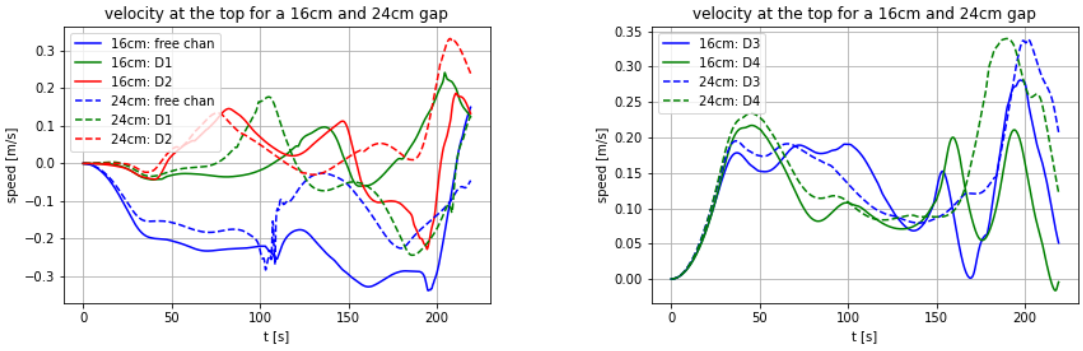

(a) (b)

Figure 4.59: graph of the velocity in the left part of the rack for the 16cm gap (continuous lines) and the 24 cm gap (dashed lines)

The evolution of the vertical speed in the D2, D3 and D4 channels is less impacted by the widening of the channels at the beginning of the simulation. The three corresponding dashed curves in the graph 4.59a and 4.59b stay quite close to the continuous ones at least until $t = 150s$, when the speed in the two channels suddenly increases in the 24cm gap case, with a maximum speed reaching values up to $0,35[\frac{m}{s}]$. The higher velocity in D2 is due to the presence of a hotter region at the top of this channel compared to the case in section 4.3.5 (the water is hotter there, because the local vertical velocity was a bit lower in the moment prior, which means that the convection was less effective) and it is also linked to the big reflux in D1 discussed in the previous paragraph.

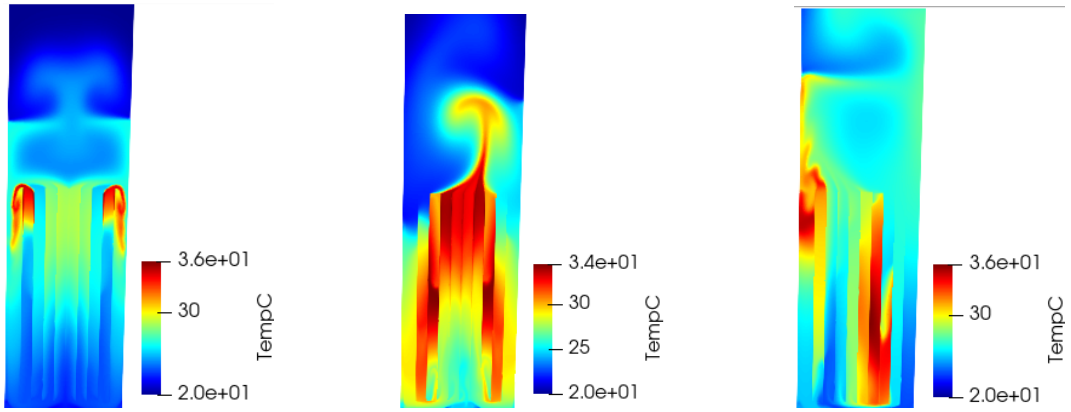

(a) (b) (c)

Figure 4.60: temperature profiles of the sinusoidal heat release case at $t = 110s$ (a), $t = 160s$ (b) and $t = 220s$ (c)

The higher temperature at the top of D2 is visible on graph 4.61a between $t = 160s$ and $t = 180s$ (red dashed line). Apart from that, the evolution of the temperature at the top of D3 and D4 doesn't diverge that much compared to the the 16cm gap case. The temperature profiles on 4.61b start to decrease a bit more at the end near $t = 180s$ because the higher vertical velocity in the two innermost channels imply that the hot regions were evacuated faster.

In conclusion, a wider gap on this configuration of the assemblies induces a better evacuation of the heat in the D1 and D8 channels at the beginning (almost no reflux there before $t = 120s$), and it also increases the efficiency of the convection in the innermost channels later on in the simulations.

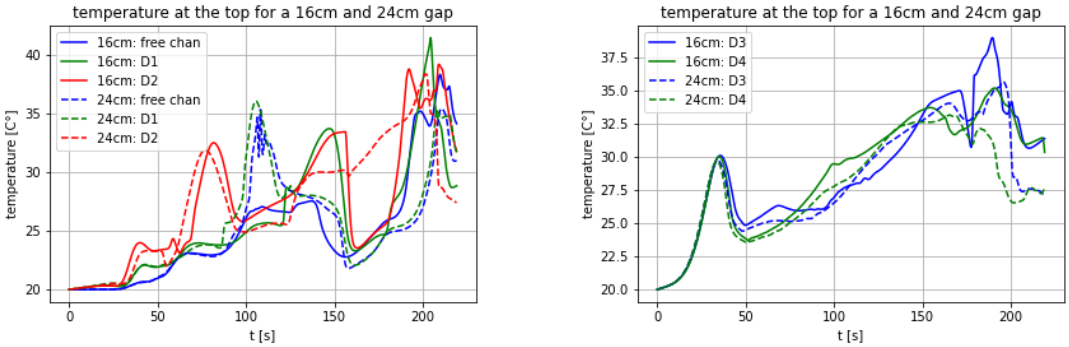

(a) (b)

Figure 4.61: graph of the temperature at the top of the assemblies in the left part of the rack for the 16cm gap (continuous lines) and the 24 cm gap (dashed lines)

4.4.6 Configuration 1 : long-range simulation

In this section, we will take a look at the long term behavior of the flow in the first configuration. Here, a rack full of identical nuclear assemblies each releasing a power of 70kW was set in a pool with a 24 cm gap between the walls and the outermost assemblies. The time step was equal to 1ms and the duration of the simulation was 660 seconds.

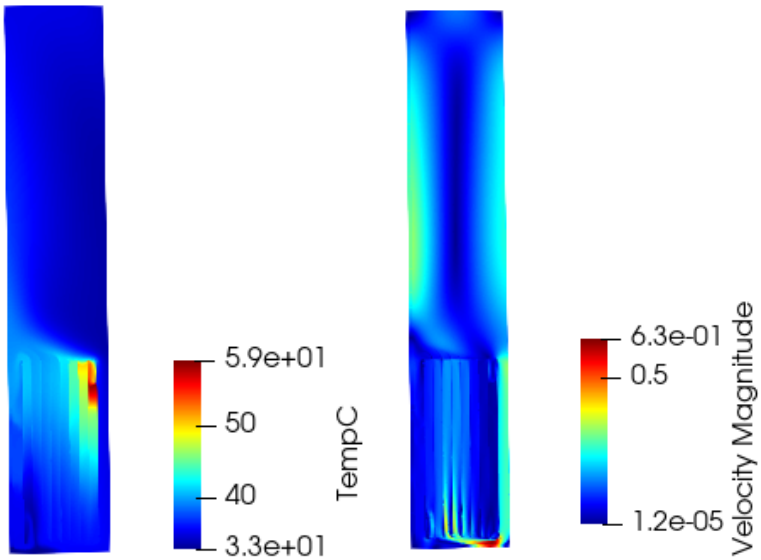

(a) (b)

Figure 4.62: temperature (a) and velocity (b) heat maps at $t = 660s$

By looking at figure 4.62a, we see that the temperature field at $t = 660$ seconds is very uniform across the domain, with an average value just above 33 degrees Celsius. A hot spot is visible at the top right of the assemblies, but it is limited to a single channel. The temperature of the other channels is barely above the average temperature of the pool, indicating that the hot water leaving the channels has undergone significant mixing with the pool water. When we look at the velocity field, we see that the entire area above the rack is occupied by a huge convection cell that rises to the surface of the pool. This cell is the reason why the temperature field is so uniform, as the hot water coming from the rack has been able to mix with the colder water at the top.

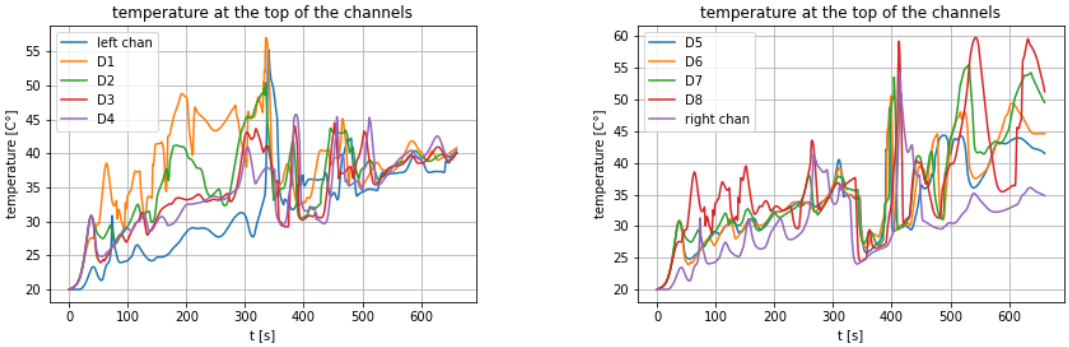

(a) (b)

Figure 4.63: graph of the temperature at the top of the assemblies in the left (a) and the right (b) part of the rack for the 24 cm gap

A radical change in the dynamics inside the rack can be seen from around $t = 350$ seconds on figure 4.63a. In the first part of the simulation, the left-hand side of the rack undergoes significant temperature variations at its top, with very high maxima, while the top of the right-hand side of the rack remains close to an average temperature of 35C°. After the transition, we observe a complete inversion of behavior: the temperature in the left-hand part stabilizes at around 40C°, while the right-hand part sees its oscillations increase considerably in amplitude, with some areas undergoing temperature variations of the order of 25C° at the top of channel D8.

On the velocity profile graphs on figure 4.64a, we can see that the first part of the flow corresponds to a period when the flow velocity in the free channel on the left is practically constant, and the flow moves downwards at a rather high speed. We can also see that once temperature variations become less abrupt, the velocity in the free channel decreases sharply and begins to oscillate around zero. Also, the amplitude of velocity oscillations in the channels with an assembly on the left of the rack increases while staying above zero. This transition, appearing at $t = 330$ seconds, is due to the formation of the huge convection cell taking up the entire depth of the pool from the surface to the top of the rack. The cell rotates in a clockwise direction, causing the downward flow to block the water in the right-hand channels, resulting in the sudden temperature variations visible after 330 seconds on the 4.63b graph as the water flow undergoes sporadic period of reflux and can thus accumulate heat. As this cell is fed by the flow coming from the left side of the rack, the velocity in these assemblies is higher on average, and as a result the water temperature in this part of the rack stabilizes at a value slightly above the average temperature of the pool.

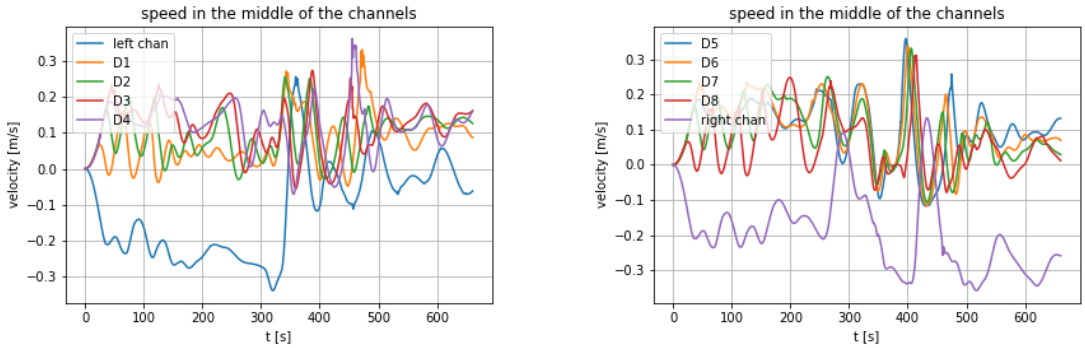

(a) (b)

Figure 4.64: graph of the vertical velocity in the assemblies in the left (a) and the right (b) part of the rack for the 24 cm gap

In conclusion, the flow in the pool undergoes a transition from a system of two symmetrical convection cells to a single huge cell. This has a huge impact on the cooling dynamics inside the rack, as one of the two sides will be blocked by the reflux. As a result, hot spots will systematically appear at the top right of the assemblies once this massive convection cell has formed.

Chapter 5

Discussion

In this chapter, we are going to discuss and summarize the main findings described in chapter four. The impact of each parameter on the flow in the pool will be evaluated independently.

5.1 Impact of the free channels width

One of the first things worth noticing when looking at the velocities in the channels containing an assembly is that in all simulations for all configurations, the speed of the flow in some channels will be equal to zero momentarily. This observation is due to the principle of conservation of mass as explained in the previous chapter: if water rises in a channel, it must go down somewhere. Normally, the places where this downward flow occurs are the two spaces between the rack and the walls, but these are not wide enough to prevent the flow in some channels from being temporarily stopped. Consequently, the velocity profiles of the first three configurations will adopt a sinusoidal shape with a more or less important phase shift with respect to each other. To summarize, the channels will either empty their hot water into the area above the rack one after the other, or some of them will undergo a reflux most of the time, which means that most of their hot water will be evacuated by the bottom (like the low power assemblies in section 4.4.3 and 4.3.3 for instance).

A widening of the free channels has for main consequences to damp the amplitude of the current oscillations in the outermost channels for configuration one, two and three, in addition to decreasing the speed in the free channels themselves. Because of the evident correlation between the temperature field and the velocity field, the location of the hot spots is also highly dependent on the speed of the flow. For a hot spot to appear, it is necessary that the water in an assembly remains stationary for a relatively long period of time. In this way, heat can accumulate locally, causing an increase of the temperature. As the amplitude of the vertical velocity oscillation decreases, the water will remain locally less still and the temperature field in the channels will also undergo oscillations of lower amplitude. Note that this reduction of the amplitude is not systematic, especially in the channels located at the center of the rack. In order to improve the evacuation of the hot water from the assemblies, it is also necessary to increase the space between the pool floor and the bottom of the rack (distance dy1 in section 3.6.3) as this zone is also a choke point were the speed of the flow increases dramatically. In case number four and five, the widening of the two free channels changes the behavior of the flow in the later stage of the simulation. Indeed, some channels will undergo an important reflux in the 24cm gap configuration but not in the 16cm one, which will impact the location of the hot spots.

5.2 Impact of the nuclear wastes configuration

Depending on the power distribution in the assemblies, the reflux will take place in different locations. In general, they will be located in the assemblies containing a waste with a low thermal output. This will be particularly true if they are grouped together, as in configuration number two, three and five ("Inverted centered distribution","rack with an asymmetrical distribution" and "rack with older nuclear wastes in the center"). This also means that hot spots will often occur at the bottom of assemblies if

they are of relatively low power. The reflux in an assembly will also be increased if this assembly has a low power output, is far from the high power channels and close to the free channels. For example, in the fifth configuration studied with a 16cm gap, the two low power channels with an assembly close to the walls experienced such an intense back flow that all the hot water accumulated during the first 100 seconds was evacuated from the bottom.

The most efficient configuration for removing heat from the assemblies when half of the nuclear wastes have a power divided by two is configuration five where the most powerful assemblies are placed in the middle. The maximum temperature reaches a value of 40C°, which is lower than in the other configurations, where the temperature can locally reach a value of nearly 50C°. This is due to the fact that the mixing with the colder water initially located above the rack is more effective.

5.3 Impact of the power released by the assemblies

Beside the obvious increase in temperature at any given time, the doubling of the power output of the assemblies also induce an increase of the speed in the channels. However, the velocity increase is not proportionally related to the temperature increase, and we only see a moderate increase of 20% in most channels. The main shape of the flow is also mainly preserved. For instance, the two convection cells at the top of the rack present in the "35-17.5kW" simulation round will also be present in the "70-35kW" one and will induce a reflux at the same location. The velocity curves are also very similar, for instance the alternate distribution case behaves in the same way with both power output despite the fact that the flow undergoes a radical change in its shape halfway through the simulation.

5.4 Impact of the shape of the heating profile

The shape of the heating profile, whether it is uniform or sinusoidal, doesn't impact much the shape of the velocity field in all the studied configurations excepted one. Indeed, the rotation direction of the massive convection cell that appears on top of the rack in the alternate distribution case (configuration 4) depends on the shape of the heating profile, and so the hot spots will not be located in the same assemblies. In all configurations however, the hot spots in the sinusoidal configurations tend to be hotter as the heat flux is unevenly distributed and the power source is higher in the middle of the assemblies than at the extremities.

5.5 The importance of convection cell geometry

The geometry of the convection cells above the rack will play a major role in cooling the nuclear waste. This geometry obviously depends on the parameters studied so far (assembly configuration, distance between walls and rack, etc.) and will have an impact on the duration and temperature of hot spots. Indeed, the size of the cells and the direction of flow within them will influence mixing efficiency. If we want to delay the onset of boiling points as much as possible, we absolutely must avoid the same water flowing through the rack over and over again, as this would mean that a small part of the water would accumulate all the energy, and for this to happen, the hot and cold regions must mix efficiently.

An example of poor mixing can be seen in configuration number two, where less powerful nuclear waste is placed in the middle. As explained in the corresponding section, initially the hot water leaving the rack will flow directly back into the two free channels, limiting mixing with the cold water-filled region above the rack. Eventually, a region of relatively warm water located just above the rack will begin to rise suddenly, which will both homogenize the temperature in the pool and cause a backflow to the center of the rack. On the contrary, configuration number three, where all the high-power assemblies are placed on one side of the rack, will undergo much more efficient mixing with the appearance of a huge convection cell that will bring the hot water to the surface very quickly.

If we compare all the configurations, we can see that the hottest spots are generally located at

the top of the high-power assemblies, with a single convection cell in the space between the rack and the surface. This is the case in configuration three, where the temperature reaches a maximum of 47 degrees to the right of the rack, and it's also the case in the long-term simulation of configuration one, where the hot spots can be thirty degrees hotter than the water right next to them.

The appearance of a single convection cell will have two consequences. On the one hand, it will homogenize the temperature throughout the pool, which is a good thing, but on the other hand, the reflux induced by this cell will greatly favor the emergence of hot spots on one side of the pool, especially as this reflux will generally last over time.

5.6 Overall areas for improvement

The assumptions and the simplifications made on the assemblies and on the flows imply that the results presented in this master thesis will not exactly match with what is observed in a real pool. Here are the main identified areas of improvement:

- **Area 1: 2D simulation**
  Because of the limitation in time and the limited amount of CPU available, it was not practical to make simulations in 3 dimensions with a very small spatial resolution. For instance, one of the 2D simulations already required 90 processors and a computing time of almost two days. It was decided that it was better initially to have good results in 2D with a very fine mesh, rather than poorer results in 3D due to a coarse mesh. However, the 2D simulations don't capture the impact on the flow of the assemblies lying behind and in front of the row studied here.

- **Area 2: improved heat transfer model**
  The way the heat transfer from the assemblies to the water has been modeled is not totally realistic. In reality, it would have been more correct to use a procedure where the local heat flow depends on the local water temperature, the flow velocity and the rod temperature. Such a model was partially presented in the section 3.3.3. The main difficulty lies in being able to find a good model for the heat transfer coefficient h.

- **Area 3: improved modelisation of the inner structure of an assembly and the head loss**
  In this work, the assemblies were modeled as a set of vertical rods placed in parallel. In reality, an assembly also contains metal reinforcements perpendicular to the rods which keep them attached to each other. These reinforcements will occasionally disrupt the flow along the assembly, which could induce local heating. In addition to this, the modeling of the pressure drop along the assembly used in this work does not take into account the complex geometry of the nuclear waste. In reality, the flows along the different rods will interact with each other, which means that the real head loss is not equal to the sum of the head losses of a flow along a rod in an infinite medium.

- **Area 4: improved free surface**
  Surface evaporation and change in shape of the free surface of the pool were not taken into account. A slip condition has been implemented, but it is not sufficient to realistically take into account the interactions between the pool water and the atmosphere. It could be interesting to model the free surface more accurately, especially for long lasting simulations.

- **Area 5: two phase flow**
  When the water temperature exceeds 100 degrees, bubbles will begin to form near the hot spots, which will greatly reduce the heat transfer efficiency from the fuel to the pool water. It will be necessary in future studies to model the boiling onset correctly and the resulting two phase flow using an appropriate software.

Conclusion

In this master's thesis, we sought to model the natural convection happening in a spent fuel pool using a two dimensional CFD simulation. This was done using Code Saturne, an open source software available on the Internet. By doing so, we tried to characterize the flow in the pool with various dispositions of the assemblies in the rack in order to see if some of them were better than the others. The natural convection was modeled by using the Boussinesq approximation, where the density only depends on the temperature. As the individual cells of the mesh could not be made small enough to model the smallest eddies of the turbulent flow, a RANS approach was used using the famous $k-\epsilon$ model.

More concretely, we set ourselves the objective of evaluating the impact of 5 different assembly configurations on the reflux and the location of hot spots. To do this, it was important to study the formation, shape and influence of the convection cells above the rack. These five configurations have been studied for two types of profile (uniform and sinusoidal) and two different power levels (70-35kW and 35-17kW). As the efficiency of convection depended on the capacity of the flow to descend via the two free channels, we decided to choose two different spacing values (16 and 24 cm).

The flows were analyzed thanks to the graphs of the velocity and temperature profiles. Photos of the streamlines were also taken at different intervals in order to determine the general shape of the flow at specific times. There were thirty sensors in total, which implies that not all the graphs were shown in the previous section. There would have been far too many of them and they were not all relevant for the analysis.

It was determined that a rack with a higher thermal output would increase the speed of the flow induced by the natural convection, but not in the same proportion as the increase in power, which means that the temperature at the local hot spots is much higher. Interestingly, even after 220 seconds, there are some configurations where the water close to the surface has a temperature very close to the initial temperature of the simulation (20 C°). This is particularly true for the case with older nuclear waste in the center of the rack. It shows that a good mixing just above the rack doesn't imply a good mixing in the whole pool. In the case where the rack contains four 70 kW and four 35 kW assemblies, it has been shown that the fifth configuration allows to minimize the temperature of the hot spots, with a maximum at 40 C°. It has also been shown that when a convection cell grows to take up the entire depth of the pool as in the first and the third configurations, it will enhance the mixing of the water throughout the pool and will lead to the appearance of long-lasting, high-intensity hot spots at the top of the assemblies below the downflow. The onset of boiling will also likely appear well before the mean temperature of the pool reaches 100 C° as the hot spots are sometimes 25C° hotter than the surrounding water for very short amounts of time, so the assemblies will likely be damaged more quickly than expected from a simpler analysis.

As indicated in the Discussion, it could be interesting to use an extension of Saturn Code called Neptune CFD which would allow to evaluate the impact of boiling on the heat transfer close to the assemblies for longer simulations. This would allow to continue the research work started here.

Bibliography

[1] "The nuclear power stations in Belgium | ENGIE Electrabel." [Online]. Available: https://nuclear.engie-electrabel.be/en/nuclear-power-stations-belgium

[2] J. Chadwick, "The existence of a neutron," *Proceedings of the Royal Society of London. Series A, Containing Papers of a Mathematical and Physical Character*, vol. 136, no. 830, pp. 692–708, Jun. 1932. [Online]. Available: https://royalsocietypublishing.org/doi/10.1098/rspa.1932.0112

[3] N. Bohr and J. A. Wheeler, "The Mechanism of Nuclear Fission," *Physical Review*, vol. 56, no. 5, pp. 426–450, Sep. 1939. [Online]. Available: https://link.aps.org/doi/10.1103/PhysRev.56.426

[4] M. Aoki and G. Rothwell, "A comparative institutional analysis of the Fukushima nuclear disaster: Lessons and policy implications," *Energy Policy*, vol. 53, pp. 240–247, Feb. 2013. [Online]. Available: https://linkinghub.elsevier.com/retrieve/pii/S0301421512009433

[5] "Pressurized water reactor," Mar. 2023, page Version ID: 202221549. [Online]. Available: https://en.wikipedia.org/wiki/Pressurized_water_reactor

[6] L. Sjoberg*, "Local Acceptance of a High-Level Nuclear Waste Repository," *Risk Analysis*, vol. 24, no. 3, pp. 737–749, Jun. 2004. [Online]. Available: https://onlinelibrary.wiley.com/doi/10.1111/j.0272-4332.2004.00472.x

[7] [U+FFFD] aliatka, V. gnerubov, and V. Vileiniskis, "Analysis of the processes in spent fuel pools of Ignalina NPP in case of loss of heat removal," *Nuclear Engineering and Design*, vol. 240, no. 5, pp. 1073–1082, May 2010. [Online]. Available: https://linkinghub.elsevier.com/retrieve/pii/S0029549310000129

[8] "Reacteur de grande puissance a tubes de force," Apr. 2023, page Version ID: 203782260. [Online]. Available: https://fr.wikipedia.org/wiki/Réacteur_de_grande_puissance_à_tubes_de_force

[9] C. Ye, M. Zheng, M. Wang, R. Zhang, and Z. Xiong, "The design and simulation of a new spent fuel pool passive cooling system," *Annals of Nuclear Energy*, vol. 58, pp. 124–131, Aug. 2013. [Online]. Available: https://linkinghub.elsevier.com/retrieve/pii/S0306454913001308

[10] H. Mutelle, I. Tamburini, C. Duriez, S. Tillard, N. Trégourès, A. Toutant, M. Mermoux, V. Peres, and H. Buscail, "A new research program on accidents in spent fuel pools: the DENOPI project," Sep. 2014, p. Paper No. 100071. [Online]. Available: https://hal.science/hal-01098163

[11] R. Oertel, T. Hanisch, E. Krepper, D. Lucas, F. Rüdiger, and J. Fröhlich, "Two-scale CFD analysis of a spent fuel pool involving partially uncovered fuel storage racks," *Nuclear Engineering and Design*, vol. 341, pp. 432–450, Jan. 2019. [Online]. Available: https://linkinghub.elsevier.com/retrieve/pii/S0029549318305624

[12] S. P. Neuman, "Theoretical derivation of Darcy's law," *Acta Mechanica*, vol. 25, no. 3-4, pp. 153–170, Sep. 1977. [Online]. Available: http://link.springer.com/10.1007/BF01376989

[13] S. Bories, "Natural Convection in Porous Media," in *Advances in Transport Phenomena in Porous Media*, J. Bear and M. Y. Corapcioglu, Eds. Dordrecht: Springer Netherlands, 1987, pp. 77–141. [Online]. Available: http://link.springer.com/10.1007/978-94-009-3625-6$_4$

[14] A. Bejan and K. R. Khair, "Heat and mass transfer by natural convection in a porous medium," *International Journal of Heat and Mass Transfer*, vol. 28, no. 5, pp. 909–918, May 1985. [Online]. Available: https://linkinghub.elsevier.com/retrieve/pii/0017931085902728

[15] T.-C. Hung, V. K. Dhir, B.-S. Pei, Y.-S. Chen, and F. P. Tsai, "The development of a three-dimensional transient CFD model for predicting cooling ability of spent fuel pools," *Applied Thermal Engineering*, vol. 50, no. 1, pp. 496–504, Jan. 2013. [Online]. Available: https://linkinghub.elsevier.com/retrieve/pii/S1359431112004632

[16] J. Amat Foraster, "Study for the validation of Code Saturne for turbulent flow simulations," Bachelor thesis, Universitat Politècnica de Catalunya, Jun. 2017, accepted: 2017-07-07T08:53:58Z. [Online]. Available: https://upcommons.upc.edu/handle/2117/106220

[17] J. R. Wang, H. T. Lin, Y. S. Tseng, and C. K. Shih, "Application of TRACE and CFD in the Spent Fuel Pool of Chinshan Nuclear Power Plant," *Applied Mechanics and Materials*, vol. 145, pp. 78–82, Dec. 2011. [Online]. Available: https://www.scientific.net/AMM.145.78

[18] "Code Saturne: A Finite Volume Code for the computation of turbulent incompressible flows - Industrial Applications - Archive ouverte HAL." [Online]. Available: https://hal.science/hal-01115371/

[19] N. N. Mansour, J. Kim, and P. Moin, "Near-wall k-epsilon turbulence modeling," *AIAA Journal*, vol. 27, no. 8, pp. 1068–1073, Aug. 1989. [Online]. Available: https://arc.aiaa.org/doi/10.2514/3.10222

[20] V. Guimet and D. Laurence, "A LINEARISED TURBULENT PRODUCTION IN THE k-ϵ MODEL FOR ENGINEERING APPLICATIONS," in *Engineering Turbulence Modelling and Experiments 5*. Elsevier, 2002, pp. 157–166. [Online]. Available: https://linkinghub.elsevier.com/retrieve/pii/B9780080441146500144

[21] R. K. Zeytounian, "Joseph Boussinesq and his approximation: a contemporary view," *Comptes Rendus Mécanique*, vol. 331, no. 8, pp. 575–586, Aug. 2003. [Online]. Available: https://linkinghub.elsevier.com/retrieve/pii/S1631072103001207

[22] S. Acharya, B. R. Baliga, K. Karki, J. Y. Murthy, C. Prakash, and S. P. Vanka, "Pressure-Based Finite-Volume Methods in Computational Fluid Dynamics," *Journal of Heat Transfer*, vol. 129, no. 4, pp. 407–424, Apr. 2007. [Online]. Available: https://asmedigitalcollection.asme.org/heattransfer/article/129/4/407/467619/PressureBased-FiniteVolume-Methods-in

[23] F. P. Incropera, D. P. Dewitt, T. L. Bergman, and A. S. Lavine, *Fundamentals of heat and mass transfer, Chapter 7.2 : The flat plate in parallel flow*, 7th ed. Cambridge MA: Don Fowlay, 2011.

[24] J. R. Lamarsh and A. J. Baratta, *Introduction to nuclear engineering*. Prentice-Hall, Inc, 2001, ch. 6, pp. 279–280.

[25] J.-F. Balfroid and A. Debouny, "Mémoire de fin de master : Etude numérique de la convection naturelle lors du refroidissement des combustibles nucléaires usés en piscine de désactivation," Master's thesis, Ecole polytechnique de Louvain, UCL, 2014.

[26] S. Dennis and M. Shimshoni, "The steady flow of a viscous fluid past a circular cylinder," 1964.

[27] P. P. Puttkammer, "Boundary Layer over a Flat Plate," 2013.

Appendix A

Location of the sensors

A.1 16cm gap configuration

x [m]	z [m]	x [m]	z [m]	x [m]	z [m]
0.08	4	0.08	0.32	0.08	2.16
0.268	4	0.268	0.32	0.268	2.16
0.476	4	0.476	0.32	0.476	2.16
0.684	4	0.684	0.32	0.684	2.16
0.892	4	0.892	0.32	0.892	2.16
1.1	4	1.1	0.32	1.1	2.16
1.308	4	1.308	0.32	1.308	2.16
1.516	4	1.516	0.32	1.516	2.16
1.792	4	1.792	0.32	1.792	2.16
1.912	4	1.912	0.32	1.912	2.16

A.2 24cm gap configuration

x [m]	z [m]	x [m]	z [m]	x [m]	z [m]
0.12	4	0.12	0.32	0.12	2.16
0.348	4	0.348	0.32	0.348	2.16
0.556	4	0.556	0.32	0.556	2.16
0.764	4	0.764	0.32	0.764	2.16
0.972	4	0.972	0.32	0.972	2.16
1.18	4	1.18	0.32	1.18	2.16
1.388	4	1.388	0.32	1.388	2.16
1.596	4	1.596	0.32	1.596	2.16
1.804	4	1.804	0.32	1.804	2.16
2.032	4	2.032	0.32	2.032	2.16

Appendix B

Temperature curves: 70kW-35kW rack, 16cm gap

Note : Due to a careless mistake during the setting of the sensors location, the sensor located in x = 1.912m and y = 0.32m (bottom right, in the right free channel) was unable to record the temperature field. Because of that, the corresponding curves displayed in appendix B and C are either non existent or false.

B.1 Configuration 1

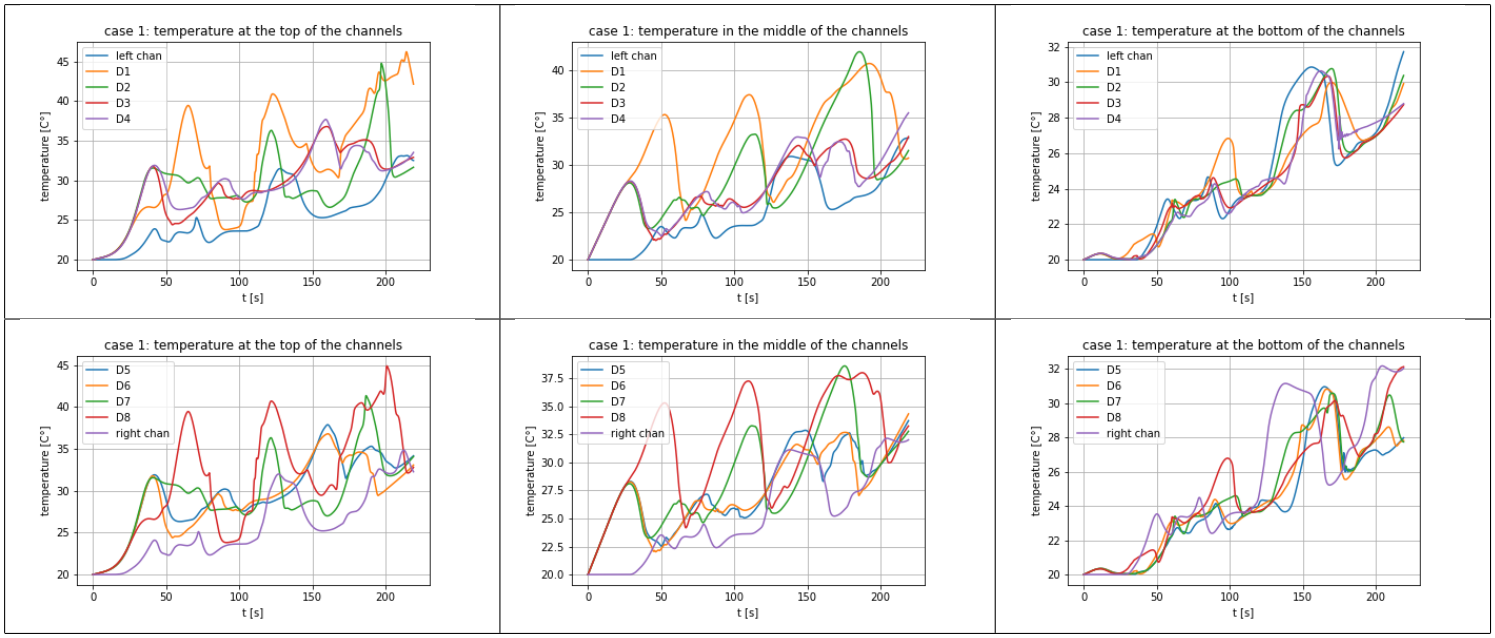

B.2 Configuration 2

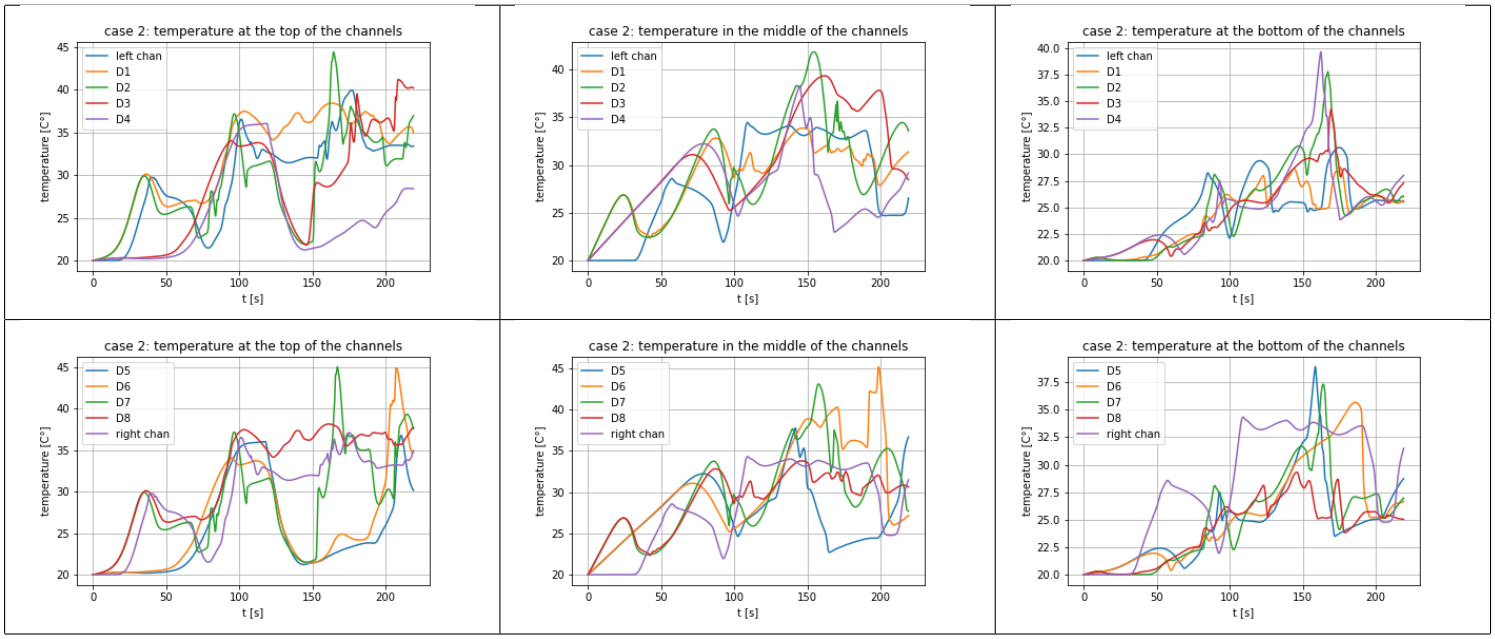

B.3 Configuration 3

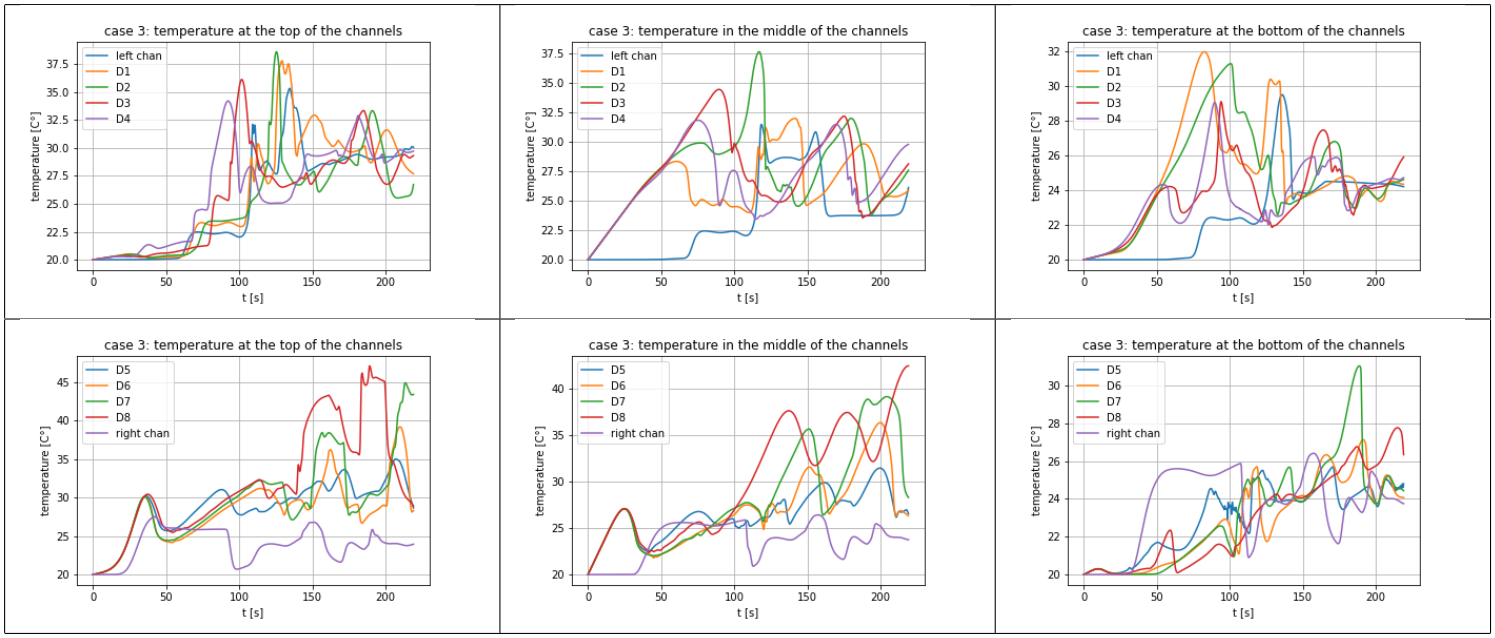

B.4 Configuration 4

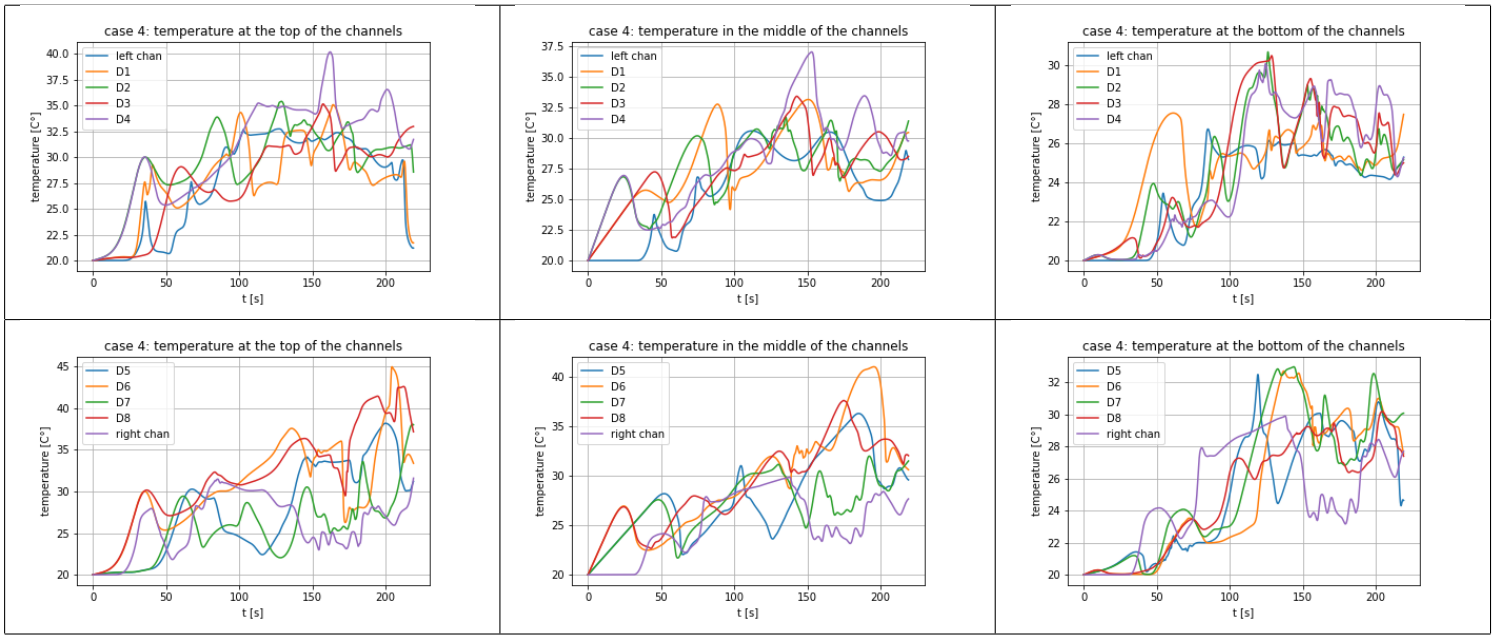

B.5 Configuration 5

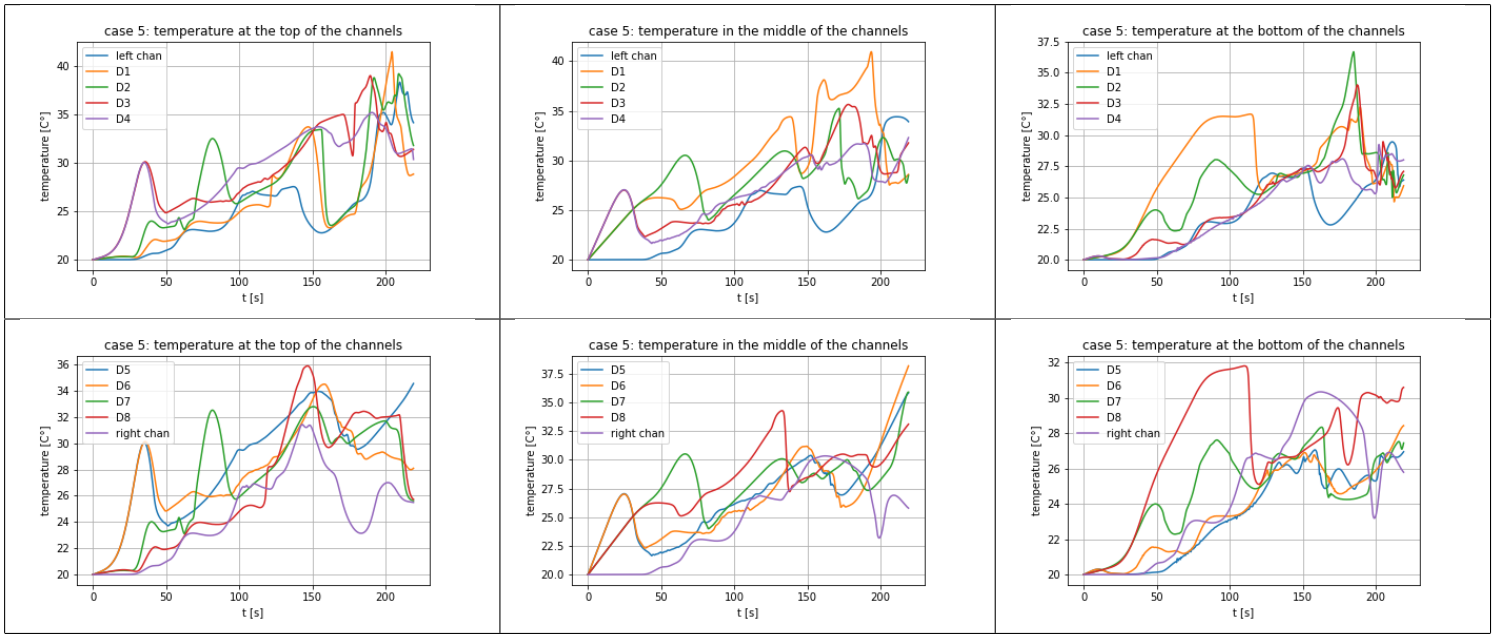

Appendix C

Temperature curves: 70kW-35kW rack, 24cm gap

C.1 Configuration 1

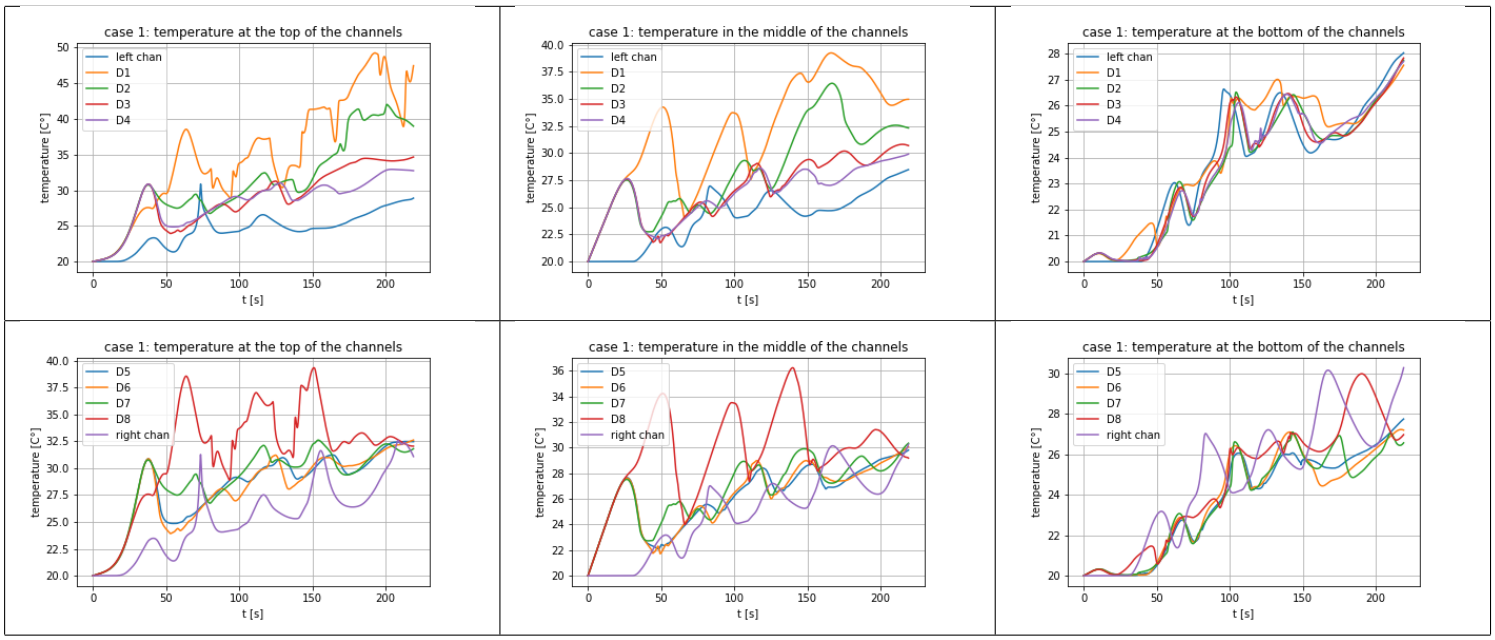

C.2 Configuration 2

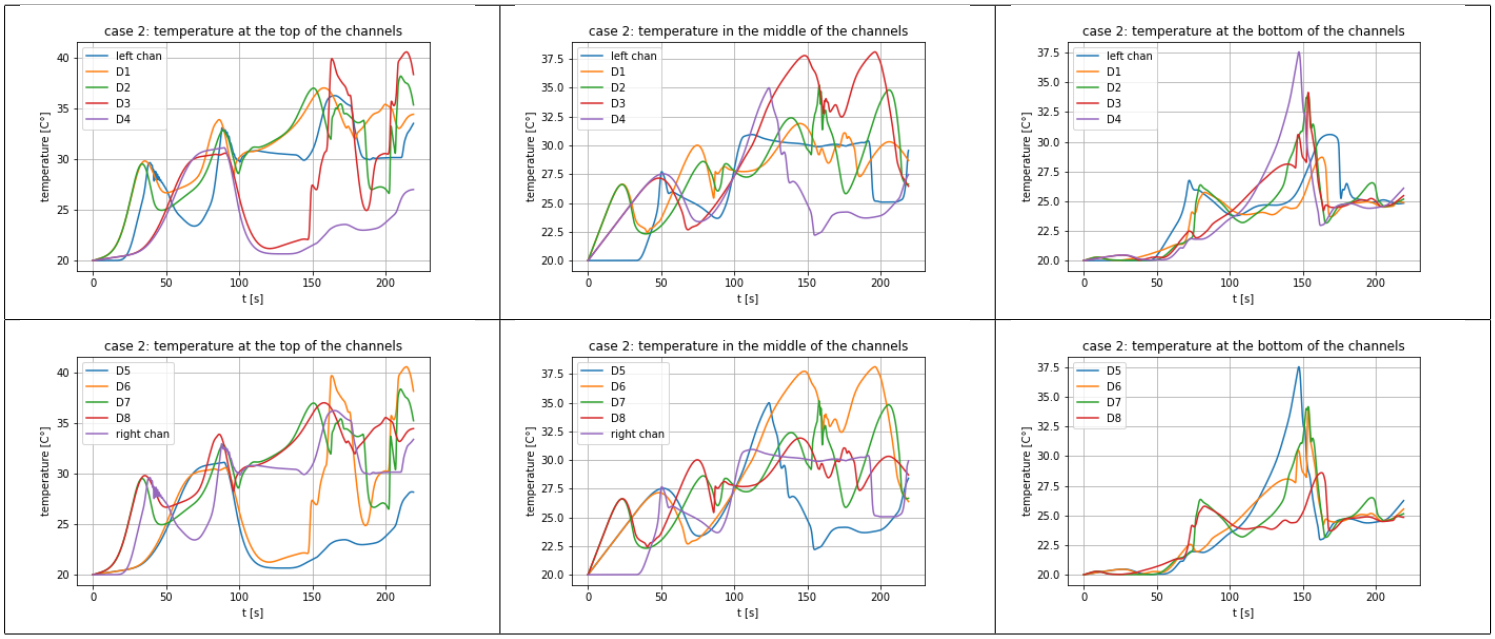

C.3 Configuration 3

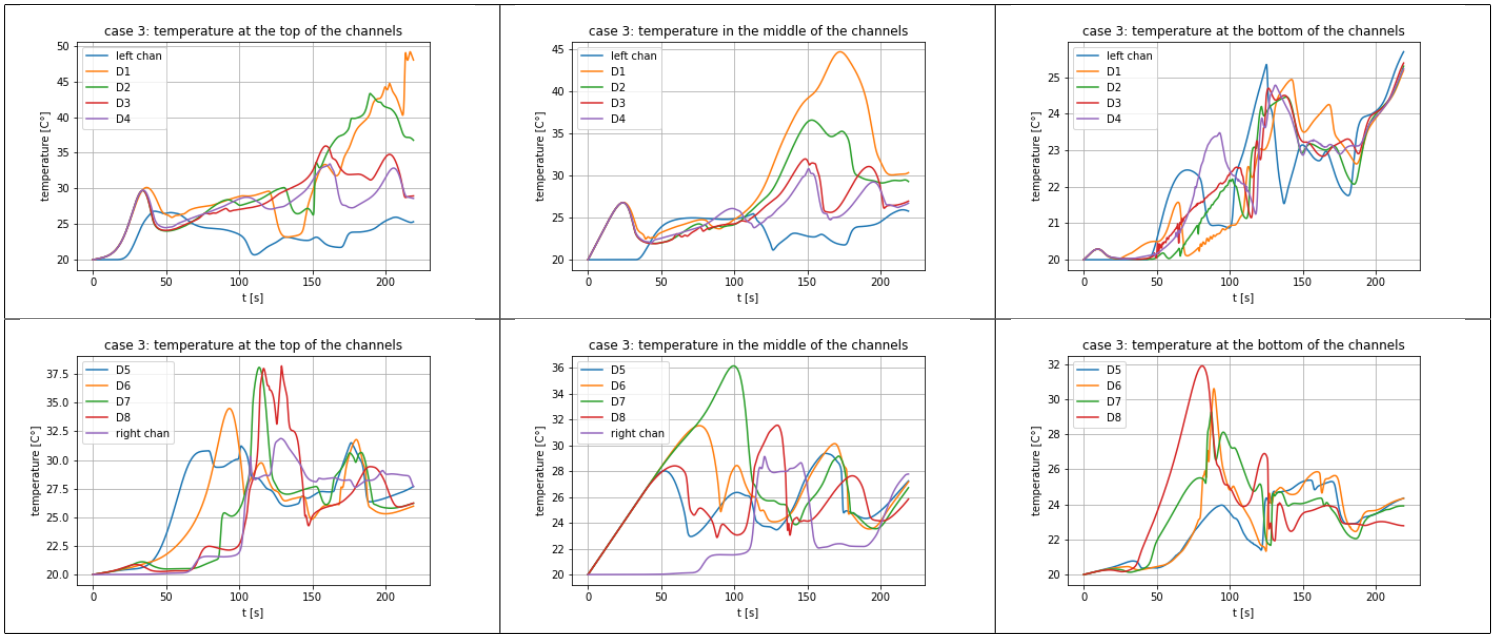

C.4 Configuration 4

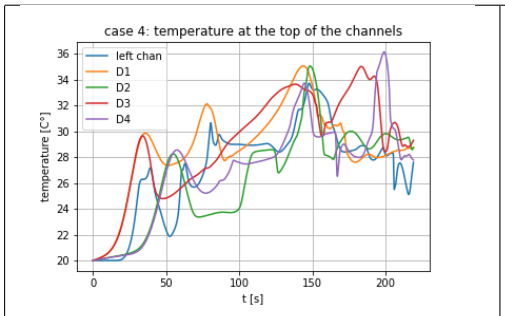

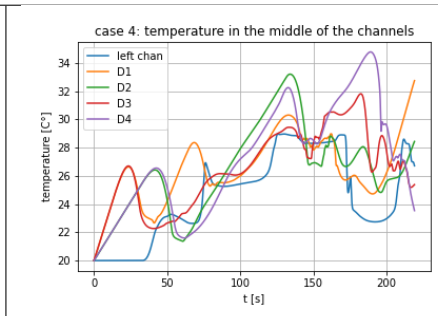

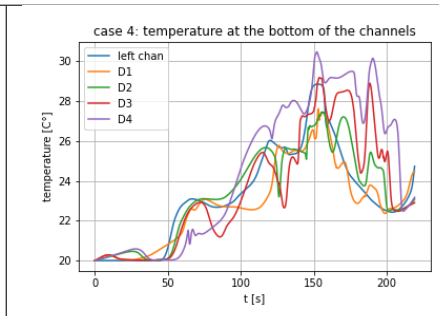

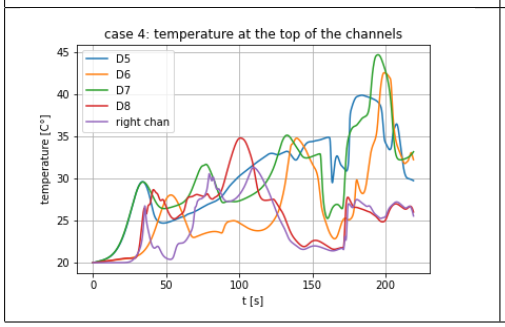

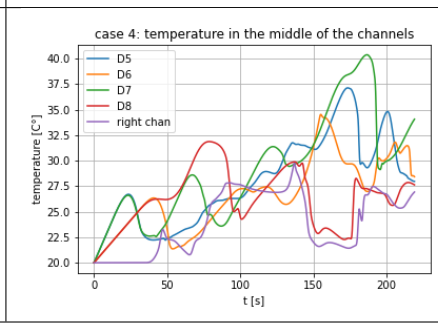

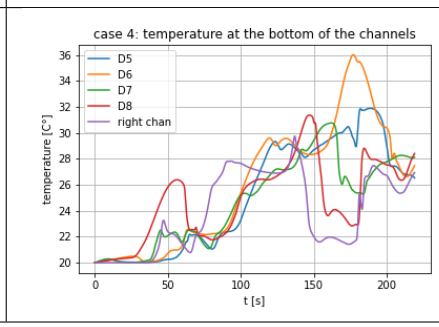

C.5 Configuration 5

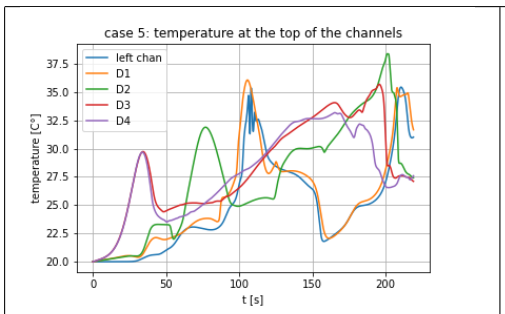

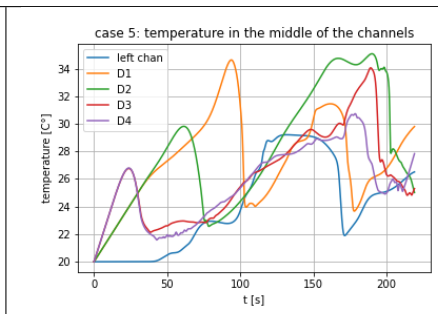

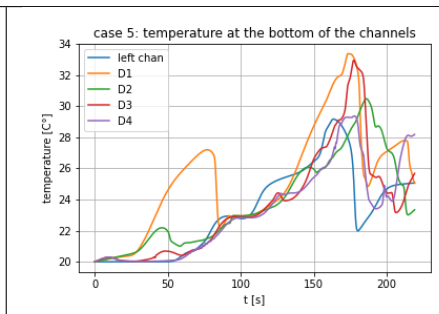

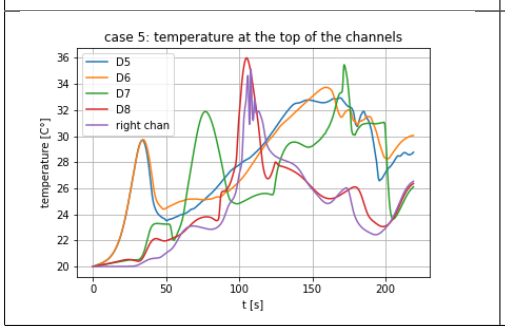

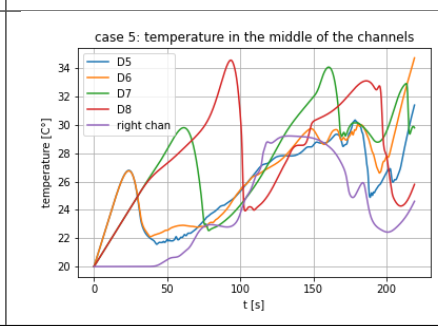

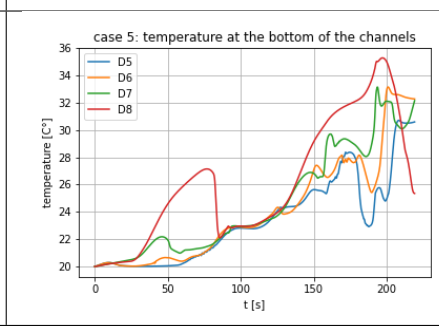

C.6 Configuration 1 long simulation

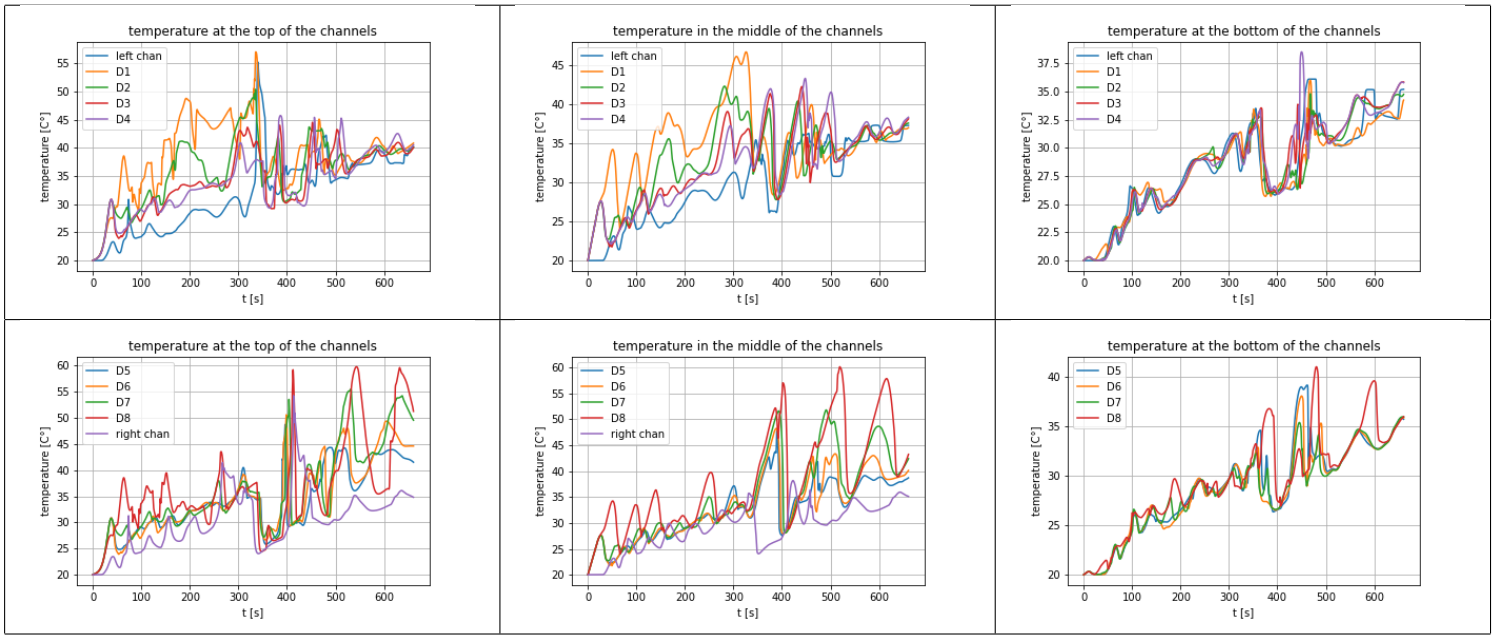

UNIVERSITÉ CATHOLIQUE DE LOUVAIN
École polytechnique de Louvain
Rue Archimède, 1 bte L6.11.01, 1348 Louvain-la-Neuve, Belgique | **www.uclouvain.be/epl**